Predicting phenotypic variation through human brain decoding and connectivity: Applications for capturing individual differences in face recognition ability, aging, and brain-computer interfaces

Andrew Joseph Graves
Knoxville, TN

B.S., B.A./ M.A., Appalachian State University, 2015/ 2017
M.A./ M.S (Data Science), University of Virginia, 2019/ 2021

A Dissertation Presented to the Faculty of the University of Virginia in Candidacy for the Degree of Doctor of Philosophy

Department of Psychology
University of Virginia
August, 2023

James P. Morris, Ph.D.
Jessica J. Connelly, Ph.D.
Chad S. Dodson, Ph.D.
Kevin A. Pelphrey, Ph.D.

Abstract

The following three chapters are a collection of studies aimed to better understand individual differences in various cognitive and biological processes. The first chapter focuses on face recognition ability and the cortical structures/ representations that give rise to neurotypical heterogeneity in this behavior. The second chapter focuses on the aging process at the epigenetic and cognitive level, linking these two levels and explaining these relationships through functional connectivity of the human brain. Finally, the third chapter focuses on algorithmic modifications that incorporate individual difference information when training machine learning systems suitable for brain-computer interface systems. The substantive domains across the three chapters differ drastically, but the general analytical framework for approaching these diverse problems is shared across the three chapters. The common thread linking these interdisciplinary efforts is 1) the committed focus to understanding why people's minds and brains operate differently from one another, and 2) the successful application of modern machine learning tools to function as a mechanism for uncovering new insights about the brain and behavior. In summary, this collection of work leverages the application of modern measurement and analytic tools to design models of behavior that incorporate critical idiosyncrasies between people. These papers add novel research contributions to three different domains relevant to modern psychology and neuroscience: 1) face recognition ability, 2) aging, and 3) brain-computer interfaces.

This dissertation is dedicated to my mother Virginia Pharaoh, who passed away December 10th, 2016 to a long and hard-fought battle with cancer one year before starting my Ph.D. During one of my last conversations with her, she told me to follow my dreams, passions, and instincts. This body of work is just one demonstration of how I am living my life with this in mind, and every day it makes me happy to know how proud she is of me.

Acknowledgements

This dissertation would not have been possible without my amazing colleagues from the last six years. I cannot express enough gratitude to Jamie Morris and Jess Connelly for welcoming me into their labs, providing me their excellent mentorship, and teaching me how to be a scientist. Thank you to the remaining members of my committee for insightful discussions of my results: Chad Dodson and Kevin Pelphrey. A huge thanks to Jesse Grabman, Josh Danoff, and Gabe Yohe for all of your help generating the research ideas for Chapters 1, 2, and 3, respectively. Chapter 3 would not have been possible without the incredible guidance of Per Sederberg. I have received so much support and I am incredibly grateful for all members of the Morris and Connelly labs. Specifically, a lot of my early development as a scientist was helped by my peers Meghan Puglia, Amalia Skyberg, and Kathleen Krol. Last and certainly not least, I want to acknowledge the support of my entire family, who have helped shape me into the person I am today.

Table of Contents

INTRODUCTION 1

CHAPTER 1: ACCURACY OF FMRI DECODING MAPS FOR FACES IN DOMAIN-SPECIFIC BRAIN REGIONS RELATE TO INDIVIDUAL DIFFERENCES IN FACE RECOGNITION ABILITY 4

- **INTRODUCTION** 4
- **RESULTS** 9
- **DISCUSSION** 12
- **MATERIALS AND METHODS** 13
- **REFERENCES** 17
- **FIGURES AND TABLES** 25
- **SUPPORTING INFORMATION** 32

CHAPTER 2: ACCELERATED EPIGENETIC AGING ASSOCIATES WITH WHOLE-BRAIN FUNCTIONAL CONNECTIVITY AND IMPAIRED COGNITIVE PERFORMANCE IN OLDER ADULTS 46

- **INTRODUCTION** 46
- **RESULTS** 49
- **DISCUSSION** 52
- **MATERIALS AND METHODS** 54
- **REFERENCES** 63
- **FIGURES AND TABLES** 74
- **SUPPORTING INFORMATION** 84

CHAPTER 3: EXTENSIONS AND APPLICATION OF THE ROBUST SHARED RESPONSE MODEL TO ELECTROENCEPHALOGRAPHY DATA FOR ENHANCING BRAIN-COMPUTER INTERFACE SYSTEMS 89

- **INTRODUCTION** 90
- **METHODS** 91
- **RESULTS** 93
- **DISCUSSION** 93
- **REFERENCES** 95

*NOTE THAT FIGURES AND TABLES ARE EMBEDDED RATHER THAN APPENDED IN THIS CHAPTER

CONCLUSIONS 96

Introduction

The following sections summarize the three chapters in abstract format to briefly motivate the problem and describe the approach for the targeted research questions:

Chapter 1: Accuracy of fMRI decoding maps for faces in domain-specific brain regions relate to individual differences in face recognition ability

Submitted for peer review at Proceedings of the National Academy of Sciences (PNAS) as of July 7th, 2023.

Face recognition ability lies on a wide spectrum. Neuroimaging has richly characterized neural systems involved in face perception, but there are mixed findings in the literature associating brain activity with this heterogeneity. The notion that there exists modularity in precisely localized cortical structures that preferentially respond to faces has been criticized due to overlapping representations, expertise, and the need for whole-brain approaches to investigate complex cognitive processes. Here, we leverage populations of voxels using multivariate pattern analysis (MVPA) as a brain decoding approach for understanding individual differences in face recognition ability. We developed an old/new recognition paradigm comparing faces to flowers that satisfies domain-specific criteria and incorporates optimized stimulus-sequences for fMRI. Outside the scanner, participants completed the Cambridge Face Memory Test (CFMT) to quantify individual differences in face recognition ability. Applying MVPA on our targeted region of interest (Neurosynth mask, keyword: "ffa"), we found that face recognition ability was positively associated with decoding accuracy for stimulus differentiation between faces and flowers controlling for in-scanner performance. Follow-up analysis indicated that the information driving decoding for face recognition included regions of the core face processing system, including typical coordinates for face-sensitive Fusiform Gyrus and Posterior Superior Temporal Sulcus. Visualizations of brain representations for stronger versus weaker face recognizers suggest a structure that is less overlapping, more modular, and better respects the preference for faces in the lateral Fusiform Gyrus. We also find that taking a whole brain approach using connectome-based models cannot successfully predict face recognition ability. This work contributes to a better understanding of how domain-specific neural systems support behavioral heterogeneity in face recognition, and suggests that higher-order visual cortices that process face information may be more important than whole-brain connectivity for understanding this specific behavior.

Chapter 2: Accelerated epigenetic aging associates with whole-brain functional connectivity and impaired cognitive performance in older adults

Submitted for peer review at Science Advances as of July 7th, 2023.

While chronological age is a strong predictor for health-related risk factors, it is an incomplete metric that fails to fully characterize the unique aging process of

individuals with different genetic makeup, neurodevelopment, and environmental experiences. Recent advances in epigenomic array technologies have made it possible to generate DNA methylation-based biomarkers of biological aging, which may be useful in predicting a myriad of cognitive abilities and functional brain network organization across older individuals. As hypothesized, individuals with faster epigenetic age acceleration performed worse on tasks that spanned a wide variety of cognitive faculties including both fluid and crystallized intelligence. Additionally, fMRI connectome-based predictive models suggested a mediating mechanism of memory on epigenetic age acceleration/ functional connectivity associations primarily in medial temporal lobe and limbic structures. This research highlights the important role of epigenetic aging processes on the development and maintenance of healthy cognitive capacities and function of the aging brain. Specifically, individuals with more epigenetic age acceleration tended to perform worse on tasks that spanned a wide variety of cognitive faculties, and brain regions crucial for successful memory formation were most important for predicting AgeAccelGrim in the aging brain. These differences cannot be explained by chronological age alone, in that AgeAccelGrim and chronological age are orthogonal variables, and both were included/ controlled for in each statistical model. This suggests that epigenetic age explains a unique portion of variance of cognitive ability that chronological age does not capture, and this relationship may be explained by connectivity of memory brain structures primarily within the limbic system.

Chapter 3: Extensions and application of the robust shared response model to electroencephalography data for enhancing brain-computer interface systems

Published in IEEE Systems and Information Engineering Design Symposium (SIEDS).

**Because this paper was written in LaTeX and involves a substantial number of mathematical equations, the final published .pdf was appended to this dissertation rather than converting to the same Microsoft Word format applied to Chapters 1 and 2*

Brain Computer Interfaces (BCI) decode electroencephalography (EEG) data collected from the human brain to predict subsequent behavior. While this technology has promising applications, successfully implementing a model is challenging. The typical BCI control application requires many hours of training data from each individual to make predictions of intended activity specific to that individual. Moreover, there are individual differences in the organization of brain activity and low signal-to-noise ratios in noninvasive measurement techniques such as EEG. There is a fundamental bias-variance trade-off between developing a single model for all human brains vs. an individual model for each specific human brain. The Robust Shared Response Model (RSRM) attempts to resolve this tradeoff by leveraging both the homogeneity and heterogeneity of brain signals across people. RSRM extracts components that are common and shared across individual brains, while simultaneously learning unique representations between individual brains. By learning a latent shared space in conjunction with subject-specific representations, RSRM tends to result in better predictive performance on fMRI data relative to other common dimension reduction

techniques. To our knowledge, we are the first research team attempting to expand the domain of RSRM by applying this technique to controlled experimental EEG data in a BCI setting. Using the openly available Motor Movement/ Imagery dataset, the decoding accuracy of RSRM exceeded models whose input was reduced by Principal Component Analysis (PCA), Independent Component Analysis (ICA), and subject-specific PCA. The results of our experiments suggest that RSRM can recover distributed latent brain signals and improve decoding accuracy of BCI tasks when dimension reduction is implemented as a feature engineering step. Future directions of this work include augmenting state-of-the art BCI with efficient reduced representations extracted by RSRM. This could enhance the utility of BCI technology in the real world. Furthermore, RSRM could have wide-ranging applications across other machine-learning applications that require classification of naturalistic data using reduced representations.

Chapter 1: Accuracy of fMRI decoding maps for faces in domain-specific brain regions relate to individual differences in face recognition ability

Full author list: Andrew J. Graves, Jesse H. Grabman, Chad S. Dodson, and James P. Morris

Submitted for peer review at Proceedings of the National Academy of Sciences (PNAS) as of July 7th, 2023.

Introduction

There is a long history of mapping specific neural processes with face detection and recognition. Early studies focused on the specialization of portions of ventral occipital temporal cortex, specifically the fusiform gyrus, for the detection and perception of faces. Both subdural electrophysiological studies (1, 2) and neuroimaging work (3–6), established that a region of lateral fusiform cortex preferentially responds to faces relative to other categories of stimuli. While this region is somewhat anatomically variable between subjects, it may be reliably identified on an individual subject basis (6), and is functionally defined as the fusiform face area (FFA). In parallel to localizationist accounts, a distributed network response to the perception of faces suggests that face perception is not processed in a single brain region, but rather is distributed across the temporal lobes (7, 8). Though most of the field would generally agree that faces represent a unique class of visual information with dedicated neural systems, we know much less about how these systems contribute to the spectrum of behavioral differences in face recognition. To date, the evidence that these specialized neural systems explain phenotypic neurotypical heterogeneity in face recognition ability has been mixed (9–11).

Individual differences in face recognition ability

The notion that faces represent a specialized class of visual stimulus predates the technology to measure neural systems associated with these skills. Classic neuropsychological studies documented special cases of acquired prosopagnosia – in which damage along the temporal lobes caused deficits in recognizing familiar faces, but was distinct from general forms of agnosia (12). Though long considered to be acquired through damage, modern studies of prosopagnosia have demonstrated that face recognition lies on a spectrum, with a small percentage of people showing developmental prosopagnosia with no apparent brain damage. Conversely, there are individuals characterized as super-recognizers due to their extraordinary face recognition ability (13). Despite the common assumption that all neurotypical people are ‘”face experts”, a growing body of research suggests that there is considerable heterogeneity in the ability to accurately remember novel faces (14, 15).

Starting at one extreme of ability, developmental (or congenital) prosopagnosia (DP) refers to lifelong difficulty with learning to recognize faces (16). Diagnosis requires relatively intact visual and memory capabilities, exclusion of other diagnoses known to impact face recognition (e.g., Autism), and no evidence of brain damage (17). Numerous

neurobiological studies of prosopagnosia over the past two decades show results that are both inconsistent and incongruous with models of face recognition. For example, multiple imaging studies find that people with DP show normal face-selective activation in regions of the core face processing network, including fusiform gyrus and inferior occipital gyrus (18–20). However, broad structural differences are noted between DP and matched controls, including volumetric reductions in gray matter in the middle and anterior temporal lobe (21, 22). Additionally, DP shows altered patterns of structural connectivity, with studies finding reduced volume, density, and coherence of long-range tracts from the fusiform gyrus to the anterior temporal lobes (ATL) (23, 24), though more recent research suggests that these white matter abnormalities are locally restricted to areas abutting face-selective regions (25, 26). Moreover, inter-subject functional connectivity analysis finds that individuals with DP have weaker core-face network connections to ATL/frontal regions, but hyper-connectivity in more generalized visual areas, with these amplified connections predictive of face recognition performance (27).

Generalizing results from studies of DP to the wider population is complicated by multiple factors. First, it is not clear whether DP represents only the lower-tail of a normative distribution of ability, or should be considered a pathological disorder rooted in underdevelopment of the face system (17). Second (and relatedly), the criteria used by studies to define the DP sample can vary substantially in terms of screening measures (e.g., self-report; face recognition measures) and statistical cutoffs (28). Finally, it is likely that DP is comprised of various sub-populations. For example, one proposed distinction is between an apperceptive variant that causes difficulties with creating face percepts, and an associative variant which is not accompanied by perceptual deficits (29–31). On the other extreme of ability are super-recognizers (SRs), or individuals who are exceptionally skilled at face recognition (32). Relatively few studies have examined the neural correlates of super recognition. In the only fMRI study (to our knowledge), SRs exhibited increased fusiform gyrus size, face selectivity, and response, as compared to DPs (33). While research in this sub-population more clearly conforms to normative standards than the case of DP (i.e., most studies define the group as the upper-tail of the population), there are similar difficulties in generalizing results. SRs may display above-average ability on only some tests of face perception/recognition, but not others (34–38). Moreover, there are questions about face specificity, given that SRs are often more skilled than average in multiple visual and non-visual domains (39).

Between the extremes of DP and SR, exists a wide range of facial recognition capabilities (40). Wilmer and colleagues have established that these differences are heritable, showing remarkable similarity in Monozygotic twin pairs, and specific to facial recognition relative to recognition processes in general (41, 42). These differences in face recognition appear to be stable and are not influenced either positively through training (43) or negatively through adverse life experiences (44), and only weakly correlate with general intelligence (41, 45–49). Face recognition fMRI studies in healthy populations generally focus on group activation maps, while varying particular experimental parameters such as facial familiarity, emotion, or race. Studies explicitly addressing individual differences in recognition as a function of brain activation have typically used ROI based approaches (9, 50). Some studies find that the magnitude of the face-selective

response in the FFA is related to recognition ability (51–53) whereas others do not (54). Huang and colleagues related face recognition capabilities with greater activity in the individually defined FFA (9). Elbich and Scherf incorporated more ROIs into their analyses, and found significant relationships between behavioral performance and the magnitude of response and the spatial extent of response (50). However, these effects were significantly reduced when controlling for overall recognition capabilities. Beyond the FFA, the volume of grey matter in the ATL in one study corresponded to scores on the Cambridge Face Memory Test (CFMT, the most used measure of face recognition ability) (55) -- a finding that is closely related to increased size of the ATL face-selective response in another study (56).

Finally, there have been recent suggestions that the assumptions of functional localization is an inadequate approach for understanding brain-behavior relationships (57). The theoretical claim that challenges localization of function emphasizes neuronal populations distributed across the entire brain rather than local neuronal populations, and that these weak interacting signals across the entire brain (as well as other contextual factors) are what give rise to mental events (57). Some recent studies hint to broader patterns of activation outside of the canonical face network, including connectivity to hubs implicated in memory (e.g., medial temporal lobe, hippocampus) (53), social processing (e.g., amygdala, somatosensory cortex) (53, 56), and audition (53). Given that face recognition is a more complex and involved cognitive process than simple face detection, face recognition ability may rely on whole-brain connectivity above and beyond the core and extended face network. This is in contrast to a more modular account, which would suggest that the individual differences observed would be constrained to the core and extended face network.

In summary, there is growing literature on individual differences in face recognition. However, knowledge in this area has significant room for further inquiry. First, the vast majority of the results are derived from studies of DP, which debatably represents a different sub-population of wider face recognition ability. Second, sample sizes are generally small and results can be misinterpreted due to the statistical constraint of collapsing across heterogeneous populations. Third, many studies derive conclusions from use of functional localizers, which may instantiate different processes than are typical of face recognition, or use control stimuli that differ substantially from face tests. Finally, using traditional univariate methods to find reliable associations between specialized brain activity and behavioral variance in face recognition ability has been historically inconsistent.

Using fMRI decoding and connectivity for investigating face recognition ability

One potential methodological improvement for determining face-specific processing is to leverage populations of voxels within the face network using multivariate pattern analysis (MVPA). Univariate analysis typically focuses on individual voxels and examines their activity independently (58). In contrast, MVPA considers patterns of activity across multiple voxels simultaneously which provides information into the spatial distribution of neural activity patterns as well as unique information not captured by

univariate methods (59). MVPA may be particularly useful for studying individual differences in brain activity patterns when fitting participant-level decoding models. This personalized approach can highlight idiosyncrasies and individual variations in brain activity not captured by general population-level models (60). By examining the unique spatial patterns of brain activity within and across individuals, this provides information into how neural representations vary between people, potentially uncovering important insights into individual variation in face recognition ability. In fact, research on DPs in relation to controls suggest that MVPA using fMRI can detect functional brain differences in the absence of univariate differences (61). There has also been work using electroencephalography (EEG) to successfully decode face recognition ability directly at a group-level by classifying SRs from neurotypicals while viewing face-stimuli (but also non-face stimuli) (62, 63). Thus, there is evidence that MVPA is a useful tool in addition to traditional univariate analysis for better understanding face recognition individual differences.

Additionally, methods now exist that move beyond the localization assumption, one of the primary alternatives being functional connectivity analysis (14). Functional connectivity is quantified through spatially distributed collections of voxels with blood oxygen level dependent (BOLD) signal correlates over time (64). A high degree of shared variance between two regions across time implies coordination between those brain regions and may reflect large-scale brain network structure (65). While there inarguably exists some degree of specialization and modularity in human cortex, functionality of a specific cognitive process is often distributed across brain networks (66). This makes distilling an experimental result down to a small handful of cortical regions challenging, and potentially misleading (67). In order to model distributed representations across cortex, one particularly influential functional connectivity analysis approach is the connectome-based predictive model (CPM) (68). The simple application of ridge regression to connectivity vectors is known as ridge regression connectome-based predictive modeling (rCPM), and is considered the state-of-the-art CPM tool for detecting phenotypic differences in behavior (69). CPM is particularly suited for individual differences research, as it is highly predictive of an individual's identity irrespective of nuisance artifacts such as head motion or anatomical differences (70). An individual's functional connectome is one of the most powerful tools in fMRI for explaining individual differences in age, attention, general intelligence, and other complex cognitive skills (71–74).

Engaging domain-specific processes with task-based fMRI

For the current research, we will examine a pre-specified ROI known to be sensitive to face and object perception, and directly compare results to a whole-brain connectivity analysis to determine which approach better characterizes individual differences in face recognition ability. When investigating face recognition, it is important to consider factors of the experimental paradigm that will maximize the capacity to make claims about face recognition memory, rather than general recognition or visual memory. However, these concerns are balanced with the need to optimize stimulus sequences for event-related designs in fMRI. Dennett et al. outlined five criteria

for developing control stimuli in experiments investigating face recognition (75). The criteria specify that the control task matches the face task (1) in structure and performance, (2) on as many low-level visual features as possible, (3) in split-half reliability and that both have high reliability, and (4) in duration of the task such that both are relatively short and easy to administer. Finally, the fifth criterion requires the control task to measure a process dissociable from the face recognition task of interest. Thus, we set out to design an old/new recognition task with these five criteria in mind to allow for experimental control over stimulus features to make specific inferences regarding recognition of faces relative to other visual objects.

We developed a behavioral task in order to engage domain-specific cognitive processes and brain regions using an old/ new recognition memory paradigm made with Psychtoolbox (see Figure 1) (76). The task consisted of three encoding-recognition blocks divided across three functional runs. For each run, participants studied 10 faces and 10 flowers followed by a 96 second task-irrelevant delay (60 encoding trials total). We chose flowers as an appropriate control task, as recent evidence points to this stimulus class falling under a more general recognition component shared across numerous real-world objects (see (77) for details). During the task-irrelevant delay, participants viewed alternating videos of biological and scrambled dot motion (78). At test, different photos of the encoded stimuli were mixed with an equal number of new faces and flowers, resulting in 40 recognition trials for each block (120 recognition trials total). Participants were asked to distinguish the old items from the new items by making an old/ new judgment during stimulus presentation by pressing a button. Between each stimulus presentation, a white cross hair was presented as a jittered inter-stimulus interval (ISI) ranging from 0-12 s to allow for optimized separation of hemodynamic response function (HRF) modeling, as well as keep participants attentionally engaged by making the stimulus presentation time uncertain. The stimulus sequence in terms of timing and presentation order were optimized for event-related neuroimaging analysis for face – flower contrasts using the shell tool optseq2 (https://surfer.nmr.mgh.harvard.edu/optseq/).

We set out to test two hypotheses for capturing individual differences in face recognition ability, as measured by the CFMT which participants completed outside of the scanner. The first focuses on canonical regions sensitive to face perception, and the second focuses on whole-brain connectivity to capture distributed representations. We hypothesize that more discriminative multivariate cortical representations (fit via MVPA) within regions important for face perception will positively correlate with face recognition ability. We also hypothesize that whole-brain connectivity, in addition to taking an ROI approach, will explain unique individual difference variance in face recognition ability.

Answers to both of the questions will be fruitful additions to the literature which has been historically mixed with respect to the first and understudied in the second – and speaks to the ongoing debate regarding the local vs. global nature of brain organization as it pertains to the neural mechanisms supporting face recognition ability. To our knowledge, there is no work in the literature using state-of-the-art individual difference fMRI techniques such as rCPM (or other related CPM approaches) to directly predict

CFMT, nor is there work analyzing the relationship between decoding rates and CFMT performance within the neurotypical population. It is entirely possible that using the functional architecture of individual-specific connectomes across disparate brain regions will predict more variance in face recognition ability than previously defined regions sensitive to face perception.

Results

Event-related fMRI face recognition memory task sufficiently meets domain-specific criteria

The experimental structure of our task was equivalent across face trials and flower trials, with the same stimulus duration (3 s during encoding; 4 s during recognition), number of targets (30 for each class), and number of lures (30 for each class). Furthermore, we selected and pre-processed task stimuli to minimize featural differences across the two stimulus classes. The stimuli for this task were real-world three-dimensional objects hand-picked from the noncommercial Meissner face database and Nilsback flower database (79, 80), and were matched on luminance using the Shine MATLAB toolbox (81). The use of different images of the same object at encoding and test mitigated the potential confound of a simple picture matching strategy for both stimulus categories. Both stimulus classes have similar and high internal consistency (82): Cronbach's α for face trials was .76 and for flower trials was .81. The task is relatively short, requiring 24 minutes to complete, and group-average accuracy did not appreciably vary across the three blocks (block 1 = .70; block 2 = .70; block 3 = .69).

To demonstrate similar performance across the face and flower stimulus classes, we separately hierarchically modelled response time (RT), accuracy, hit rate, false alarm rate, d', and C with stimulus class (face vs. flower) as the predictor of interest, controlling for age and sex. We define task accuracy as (# hits + # correct rejections) / (# of trials) and we define hit rate as (# "old" responses / # old items) and false alarm rate as (# "old" responses / # new items). Figure 1 shows that the RT, task accuracy, hit rate, and false alarm rate across face and flower trials are similar. Table S1 shows that the hit rates were well-matched across the face and flower trials, while the false alarm rates were slightly higher for face trials relative to flower trials (i.e., the 95% posterior distribution for that fixed-effects parameter does not overlap with 0). However, the difference in the widely applicable information criterion (WAIC) between the false alarm rates including stimulus class as a predictor vs. a null model suggests that the null model fits better (WAIC difference of 3.4 in favor of null model). This suggests that the difference detected between the false alarm rates of the two stimulus classes is not substantial.

Additionally, we investigated whether the control stimulus (i.e., flowers) measures a process dissociable from the face memory stimulus of interest. To demonstrate this aim, we modelled signal detection metrics (grouped by stimulus class) to calculate sensitivity (d') and bias (C) (see (83) for calculation of each metric), using the *dprime* function from the *psycho* package in R (84) . In terms of d', nearly all participants performed better than chance (2 participants had negative d', Min. = -0.07,

Mean = 1.09, Max = 2.56) on both the face and flower trials, and d' was similar across the two tasks (face d' = 1.03, flower d' = 1.15). The only metric significantly and positively associated with CFMT scores, both in a joint model and in simple bivariate correlations, was face d' (see Fig. S1 and Table S2). This provides evidence that our face recognition task is sufficiently dissociable from our flower recognition task, despite overlapping perceptual and cognitive components and positive correlation between the face and flower d' scores.

To sum up, our task satisfies the five criteria for successfully modelling domain-specific face recognition capabilities, which include: a) matching the face task to a control task in structure and performance, b) matching the face task to the control task on as many low-level features as possible, c) computing similar and high metrics of internal consistency for the face task and control task, d) making the test relatively short and easy to administer, and e) measuring a control process dissociable from the face memory task of interest. These results increase confidence that experimental contrasts and MVPA decoding tasks using imaging data capture true differences between the encoding and recognition of faces and flowers, rather than differences in task demands attributed to other cognitive systems.

Univariate contrasts activate the canonical regions involved in face perception and positively correlate with multivariate pattern representations

Consistent with previous literature, the face – flower contrasts in this experiment produce canonical activation maps of fusiform gyrus, superior temporal sulcus, lateral occipital cortex, amygdala, para-hippocampal cortices, and other nearby higher order visual cortical structures contained within the "ffa" mask (see Fig. S2, Table S3 and Table S4). Fig. S3 demonstrates that both stimulus classes highly activate the majority of voxels within this region when computing face – fixation and flower – fixation contrasts, which suggests that this mask casts a wide-net along these brain areas that are not strictly face-specific but also includes voxels that show preference for other object classes. Lateral regions of the fusiform gyrus were much more active during face trials relative to flower trials, while medial regions were much less active, which is the typical result for these paradigms. Importantly, these univariate activation maps are strongly positively correlated with the MVPA decoding coefficients (see Figure 2), which suggests that this method largely captures interpretable cortical representations in terms of localized and unique activations relative to other voxels within the mask.

Multivariate pattern analysis can reliably decode stimulus states with high accuracy and individual differences in decoding accuracy positively correlates with CFMT

We successfully decoded stimulus states from one another within higher-order visual cortex well above theoretical levels of chance performance which is 50% for balanced stimulus class labels (median decoding accuracy: encode phase = 86%, recognition phase = 89%). Consistent with our hypothesis, we found that individual differences in decoding accuracy was positively associated with CFMT scores during both the encoding and recognition phase of the experiment (see Table 1). In other words,

decoding face stimuli from flower stimuli on average was easier for the classifier when participants were stronger recognizers (i.e., higher CFMT score), and more difficult for weaker face recognizers. Importantly, neither face d' nor flower d' could uniquely predict variance in individual level decoding accuracies for either the decoding phase or recognition phase. However, the bivariate correlations between face/ flower d' and decoding accuracies for both the encoding and recognition phase were positive and significant: face d'-encode (r = .224, p = .031), face d'-recognition (r = .355, p < .001), flower d'-encode (r = .217, p = .037), flower d'-recognition (r = .216, p = .038), with df = 90 for each. This pattern of results suggests that it is an individuals' face recognition ability specifically that is important for decoding these two stimulus-states during a task that engages domain-specific brain regions, rather than their general recognition capacities.

The relationship between decoding accuracy and CFMT is driven both by unique information in the hubs of the face network and typical cortical topological structure for face perception during encoding

To further probe and interpret the association between CFMT performance and stimulus-state decoding accuracy, we fit second-level GLMs directly to the decoding coefficient maps to ascertain which clusters covary with CFMT. The hypothesis is that stronger face recognizers will have larger coefficients in face-specific regions and smaller coefficients in regions that are not face-specific. Figure 3 shows that the decoding coefficients were larger (classifier gives high-probability that participant is a viewing a face) in the right posterior superior temporal sulcus (r pSTS) for stronger face recognizers during encoding, and in typical coordinates for the right fusiform face area (r FFA) during recognition. The remaining clusters are included in Table 2 and all follow the predicted directionality with respect to their functional role. For face d', clusters within left lateral occipital cortex, often dubbed the left occipital face area (l OFA), were identified and are also reported in Table 2. No clusters that covary with the decoding maps were identified with flower d'. In order to further unpack the relationship between CFMT and decoding accuracy, we plotted MVPA representations of the top 4 performers in our sample (who scored a perfect 72) and the bottom 4 performers (range from 40-47). Figure 4 shows that stronger face recognizers tend to have a structure that is less overlapping, more modular, and better respects the preference for faces in the lateral Fusiform Gyrus. Conversely, weaker face recognizers seem to have less-defined decision boundaries that tend to be overlapping and diffuse across these cortical regions

Connectome-based predictive models both at rest and during task cannot predict CFMT

Independently fitting rCPM on resting-state scans, concatenated task-based scans, and face-specific beta-series correlations from least-squares-all (LSA) maps prepped for decoding, we were unable to successfully predict CFMT from functional connectivity data across the entire brain (see Figure 5). As a validation control, we demonstrated that we can replicate previous research by successfully predicting age (an example continuous phenotype) using the same analysis pipeline and input data. The inability to predict CFMT from connectivity data is striking, given that rCPM is an excellent tool for

capturing individual differences for a myriad of demographics, personality, and cognitive abilities. This finding was inconsistent with our hypothesis, and suggests that a whole-brain perspective may be too coarse for capturing behavioral differences in face recognition ability.

Discussion

Neuroimaging has given us rich descriptions and characterizations of neural systems involved in the perception and recognition of faces, but empirical efforts to associate activity in these systems with face recognition capabilities has been inconsistent. There are at least two critical reasons for this gap in the literature. First, creating a task that allows for accurate differentiation of face-specific recognition/ memory processes from domain-general memory mechanisms is challenging and often not a core focus of fMRI studies. Second, while traditional univariate fMRI analysis has given us invaluable maps of neural activation associated with complex cognitive processes, these same analyses have been criticized as being limited with regards to assessing individual differences (85). Here, we analyze a task specifically constructed to dissociate face recognition from a more general recognition component using two contemporary multivariate approaches for characterizing face recognition ability.

This study is the first to demonstrate using fMRI showing that decoding rates of stimulus states for faces is significantly related to face recognition ability in neurotypicals, suggesting that the spatial patterns underlying stimulus encoding and processing are more discriminative as face recognition ability increases. While this relationship is not strictly due to regions within the *core* face network, we do find that the right p STS and FFA are important mechanisms for supporting successful face recognition. Well-defined cortical representations that respect the medial-to-lateral functional subdivision of fusiform cortex are characteristic of stronger face recognizers, while poorly-defined and highly distributed representations are more characteristic of weaker face recognizers. Additionally, for the first time, we find that state-of-the-art CPM-based techniques fail to capture these individual differences in face recognition ability. These patterns of results point toward face recognition ability being a unique cognitive process that may be less globally distributed with respect to neural mechanisms in contrast to other complex cognitive processes such as attention or decision-making.

Some work has raised concern about the use of task-based fMRI for biomarker discovery or individual differences research (59). Specifically, test-retest reliability of these task-based activations were generally poor, thus lowering confidence in the adoption of such tasks and analysis procedures for examining individual differences. There are at least two compelling reasons for this. First, many fMRI-based tasks were designed to elicit group-based activations, while minimizing within-subject variance. And second, many of these tasks show poor internal reliability, which would significantly contribute to the failure to find reliable activations in the brain. Thus, establishing high internal reliability in task performance is important for making inference in the imaging contrasts. We have provided evidence that our old/ new recognition paradigm does just this, mitigating the above concerns.

However, there are several limitations to this study. First, we employed a simple design to maximize power to differentiate the two stimulus classes, because using more classes would require longer scans and more cognitive resources due to the increase in trial count. However, it is important to replicate these results using more classes to be more confident that these findings are in fact truly domain-specific. Second, our measured range of face recognition performance in our sample does not include all levels of ability in this domain. Specifically, the lowest CFMT score in this sample is 40, and four participants performed at ceiling with a score of 72. That being said, because a score of 42 is often used as a threshold for mild DP (more than two standard deviations below the mean), and is thought to be present in approximately 2% of the population, this suggests that the current sample is reflective of the typical lower tail of this distribution (86, 87). A potential improvement for future studies could incorporate the CFMT+, which has been shown to provide more fine-grained information differentiating individuals with strong face recognition ability, and additionally recruiting more participants to acquire a wider range of individual differences (32). Last, it has been argued that the interpretation of MVPA coefficients must be done with caution, because decoding models might select one but not the other of two informative voxels when the two have high covariance (88, 89). While this is certainly the case, we show in Figure 2 that the MVPA coefficients are highly correlated with univariate activations, and are filtered by redundant activity generated by other voxels within the mask.

Since the advent of fMRI, face perception and recognition have been a central theme and heated topic for debate in cognitive neuroscience. Faces have also been central to the debate concerning the local vs. distributed theoretical accounts for what gives rise to complex cognitive processes. While acknowledging its limitations, this study's results suggest that individual differences in face recognition ability may be largely constrained to canonical cortical regions sensitive to faces, in line with a local rather than distributed account. This work contributes to a better understanding of how domain-specific neural systems support behavioral heterogeneity in face recognition, and suggests that specialized preferential higher-order visual cortices may be more important than whole-brain connectivity for understanding this specific behavior.

Materials and Methods

Participants

92 healthy adults with normal or corrected-to-normal vision were recruited for the current study. This data collection was a subset of a larger project examining (epi)-genetic differences in adults, thus self-identified Caucasians of European descent were included to avoid population stratification artifacts. All individuals gave written informed consent for a protocol approved by the University of Virginia (UVA) Institutional Review Board (Protocol 15051) and were paid $50 for participation. All participants, consisting of 62 females and 30 males aged 18–30 y (M = 22.50 years, SD = 3.32), were included in the analysis.

Cambridge Face Memory Test

We used the CFMT to assess individual differences in face recognition outside of the scanner as our primary index for face recognition ability (90) The CFMT is the most widely used test of face recognition ability (91). In this task, participants attempt to memorize six faces in three separate orientations. For each trial, previously viewed faces must be selected from an array of the target face and two foils. The test phase proceeds across 72 trials in three increasingly difficult blocks. In the first block, faces are presented individually in all three orientations for 3-seconds, followed by an immediate recognition trial of the same images. In the second block, participants study all six faces simultaneously for 20 seconds, and are then tested on novel images. Finally, in the third block, participants must recognize novel images distorted by Gaussian noise. Past research shows that a simple sum of correct responses is a reliable indicator of poor to above average recognition ability, with performance ranging from 0-72 correct responses (92).

Behavioral statistical models

Please see supporting information for specific modeling details, inference procedures, and motivations for using Bayesian estimation.

fMRI preprocessing for decoding and connectivity

Please see supporting information for details on fMRI acquisition and preprocessing.

fMRI first and second-level model GLMs for decoding

Fitting fMRI-specific general linear models was conducted using the *glm* module contained within nilearn, version 0.9.2 (93). For the first-level models, voxel-wise autoregression [AR(1)] models were fit in standardized space, with no smoothing at the first level. Condition onsets were convolved with the canonical Glover hemodynamic response function (HRF) (94). All three task-runs for each subject were fit, and subject-specific first-level parameters were aggregated across the three runs as implemented in nilearn.

Single-trial beta-series were also fit for the purposes of trial-level brain decoding using multivariate pattern analysis (MVPA) and task-based functional connectivity. The same steps were performed at fitting as described above for the traditional first-level models, with the one exception that single trials were separately convolved with an HRF and received their own column in the voxel-wise AR(1) design matrix, as is typical in MVPA analysis using LSA single-trial beta-series. The individual trial maps were concatenated together to form a 4-D structure, with each trial containing a 3-D brain volume of main-effect parameter estimates. The decoding MVPA input (single-trial beta-series first-level model images) were masked using a targeted functional region-of-interest (ROI) analysis as defined by a meta-analytic approach using Neurosynth.org

(keyword: “ffa”), which was derived from 99 studies and contains 6238 voxels at our measured resolution (95). Importantly, this mask contains regions that are canonically activated both by face and other visual non-face stimuli (see Fig. S4). Before model fitting, beta-series images were smoothed using a Gaussian kernel of 4 mm full-width at half-maximum. For brain decoding using MVPA, participant-specific penalized L2-norm logistic regression classifiers were fit using leave-one-run-out cross-validation with the following label classification tasks (encode face vs. encode flower, recognize face vs. recognize flower). Each participant received the same regularization parameter ($\lambda = 1$ as implemented in *sklearn* (96)). Participant-specific decoding was fit and accuracy was computed separately for each of these label classification tasks with a decision threshold of .5. Accuracy is a reasonable performance metric, since the classification labels are fully balanced and theoretical chance performance is 50%.

All second-level modelling approaches included age, sex, handedness, CMFT, d’ and C for both stimuli, as potential covariates of interest as well as nuisance variables. For exploratory covariate-based analysis on the participant-specific decoding images, we used a statistical threshold of two-tailed $p < .005$ and cluster extent of 10 voxels, as this threshold has been championed as being both sensitive and conservative for new discoveries (97). Anatomical labels for all results were identified from clear agreement across the default anatomical atlases implemented in the *AtlasReader* package in python (98), and this software was also used for cluster analysis. For modelling decoding accuracies, we used multivariate Bayesian beta regressions fit to the outcome variables of encoding and recognition decoding accuracies, from participants’ CFMT, face/ flower d’ and C, age, and sex.

Parcellation and image preparation for connectivity

We applied rCPM to three different inputs, a single resting-state scan (660 volumes), the three concatenated functional runs (1845 volumes), and the single-trial task-based beta-series for face trials (90 volumes). For all input scans, parcellation was performed by taking the framewise average of the voxel-wise signals in each of the 268 nodes from the Shen atlas (99). The Shen atlas is a functionally defined parcellation that covers the whole brain, including cortex, subcortex, and cerebellum. The three task-based scans were concatenated along the time dimension before calculating connectivity, as this can improve reliability of estimates (100). We calculated Fisher Z transformed Pearson correlation coefficients between the activity time courses of all possible pairs of nodes to construct 268 x 268 symmetric functional connectivity matrices. Only the lower triangle of each functional connectivity matrix was vectorized, discarding the constant diagonal, resulting in 35778 unique connections/ edges, which served as input features (i.e., columns in the design matrix) to rCPM.

Ridge regression connectome-based predictive modeling

It has been empirically demonstrated that applying an L2-norm ridge regression penalty to this connectivity vector is a simple and effective way to generate generalizable predictions from neuroimaging data, and tends to outperform other popular connectome-

based modeling approaches (69). Ridge regression is a linear supervised learning technique that regularizes model coefficients toward 0 with the canonical L2 norm. The regularization degree is governed by a single parameter, λ, where large values perform more shrinkage and small values perform less shrinkage. The lower triangle of the connectivity matrix can be cast as a vector to function as the feature space during model fitting.

We performed rCPM using a repeated (N = 100) outer K-fold (K = 10) cross-validation procedure where individuals were split into 10 folds, models were trained using 9 of the folds, and then evaluated on the held-out fold (73). Within each cross-validation split, we tuned λ with an inner 2-fold cross-validation loop to conservatively estimate optimal regularization strength and overall prediction fit. The phenotypic outcomes were residualized with respect to confound/ nuisance variables, which included CFMT, d' and C for both stimuli, age, and sex. Prediction performance for the rCPM models were evaluated using Spearman's correlation between observed and predicted behavior, since successful rank prediction across participants was considered most important. To assess the statistical significance of prediction performance, we generated null distributions of expected performance metrics due to chance by permuting behavioral scores with respect to individuals and ran the rCPM pipeline for 1000 iterations. Then, we calculated a non-parametric p-value, which tallies the number of times the performance metric for each of the 1000 iterations of the null distribution exceeds the median performance metric of the 100 true iterations.

References

1. T. Allison, *et al.*, Face recognition in human extrastriate cortex. *J. Neurophysiol.* **71**, 821–825 (1994).

2. T. Allison, G. McCarthy, A. Nobre, A. Puce, A. Belger, Human Extrastriate Visual Cortex and the Perception of Faces, Words, Numbers, and Colors. *Cereb. Cortex* **4**, 544–554 (1994).

3. J. Sergent, S. Ohta, B. Macdonald, Functinoal Neuroanatomy of Face and Object Processing: A Positron Emission Tomography Study. *Brain* **115**, 15–36 (1992).

4. G. McCarthy, A. Puce, J. C. Gore, T. Allison, Face-Specific Processing in the Human Fusiform Gyrus. *J. Cogn. Neurosci.* **9**, 605–610 (1997).

5. A. Puce, T. Allison, J. C. Gore, G. McCarthy, Face-sensitive regions in human extrastriate cortex studied by functional MRI. *J. Neurophysiol.* **74**, 1192–1199 (1995).

6. N. Kanwisher, J. McDermott, M. M. Chun, The Fusiform Face Area: A Module in Human Extrastriate Cortex Specialized for Face Perception. *J. Neurosci.* **17**, 4302 (1997).

7. J. V. Haxby, *et al.*, Distributed and Overlapping Representations of Faces and Objects in Ventral Temporal Cortex. *Science* **293**, 2425–2430 (2001).

8. J. A. Collins, I. R. Olson, Beyond the FFA: The role of the ventral anterior temporal lobes in face processing. *Neuropsychologia* **61**, 65–79 (2014).

9. L. Huang, *et al.*, Individual differences in cortical face selectivity predict behavioral performance in face recognition. *Front. Hum. Neurosci.* **8** (2014).

10. R. W. McGugin, A. E. Van Gulick, B. J. Tamber-Rosenau, D. A. Ross, I. Gauthier, Expertise Effects in Face-Selective Areas are Robust to Clutter and Diverted Attention, but not to Competition. *Cereb. Cortex* **25**, 2610–2622 (2015).

11. R. W. McGugin, K. F. Ryan, B. J. Tamber-Rosenau, I. Gauthier, The Role of Experience in the Face-Selective Response in Right FFA. *Cereb. Cortex* **28**, 2071–2084 (2018).

12. H. D. Ellis, M. Florence, Bodamer's (1947) paper on prosopagnosia. *Cogn. Neuropsychol.* **7**, 81–105 (1990).

13. E. Noyes, P. J. Phillips, A. O'Toole, "What is a Super-Recogniser?" in *Face Processing: Systems, Disorders and Cultural Differences*, (2017), pp. 173–201.

14. B. C. Duchaine, K. Nakayama, The Cambridge Face Memory Test: Results for neurologically intact individuals and an investigation of its validity using inverted face stimuli and prosopagnosic participants. *Neuropsychologia* **44**, 576–585 (2006).

15. L. T. Germine, B. C. Duchaine, K. Nakayama, Where cognitive development and aging meet: Face learning ability peaks after age 30. *Cognition* **118**, 201–210 (2011).

16. J. J. Barton, S. L. Corrow, Recognizing and identifying people: A neuropsychological review. *Cortex* **75**, 132–150 (2016).

17. J. J. S. Barton, S. L. Corrow, The problem of being bad at faces. *Neuropsychologia* **89**, 119–124 (2016).

18. U. Hasson, G. Avidan, L. Y. Deouell, S. Bentin, R. Malach, Face-selective Activation in a Congenital Prosopagnosic Subject. *J. Cogn. Neurosci.* **15**, 419–431 (2003).

19. G. Avidan, U. Hasson, R. Malach, M. Behrmann, Detailed Exploration of Face-related Processing in Congenital Prosopagnosia: 2. Functional Neuroimaging Findings. *J. Cogn. Neurosci.* **17**, 1150–1167 (2005).

20. G. Avidan, M. Behrmann, Functional MRI Reveals Compromised Neural Integrity of the Face Processing Network in Congenital Prosopagnosia. *Curr. Biol.* **19**, 1146–1150 (2009).

21. M. Behrmann, G. Avidan, F. Gao, S. Black, Structural Imaging Reveals Anatomical Alterations in Inferotemporal Cortex in Congenital Prosopagnosia. *Cereb. Cortex* **17**, 2354–2363 (2007).

22. L. Garrido, *et al.*, Voxel-based morphometry reveals reduced grey matter volume in the temporal cortex of developmental prosopagnosics. *Brain* **132**, 3443–3455 (2009).

23. C. Thomas, *et al.*, Reduced structural connectivity in ventral visual cortex in congenital prosopagnosia. *Nat. Neurosci.* **12**, 29–31 (2009).

24. I. Tavor, *et al.*, Separate parts of occipito-temporal white matter fibers are associated with recognition of faces and places. *NeuroImage* **86**, 123–130 (2014).

25. J. Gomez, *et al.*, Functionally Defined White Matter Reveals Segregated Pathways in Human Ventral Temporal Cortex Associated with Category-Specific Processing. *Neuron* **85**, 216–227 (2015).

26. S. Song, *et al.*, Local but not long-range microstructural differences of the ventral temporal cortex in developmental prosopagnosia. *Neuropsychologia* **78**, 195–206 (2015).

27. G. Rosenthal, *et al.*, Altered topology of neural circuits in congenital prosopagnosia. *eLife* **6**, e25069 (2017).

28. J. Geskin, M. Behrmann, Congenital prosopagnosia without object agnosia? A literature review. *Cogn. Neuropsychol.* **35**, 4–54 (2018).

29. P. I. N. Ulrich, *et al.*, Perceptual and memorial contributions to developmental prosopagnosia. *Q. J. Exp. Psychol.* **70**, 298–315 (2017).

30. F. Biotti, K. L. H. Gray, R. Cook, Is developmental prosopagnosia best characterised as an apperceptive or mnemonic condition? *Neuropsychologia* **124**, 285–298 (2019).

31. A. Albonico, J. J. S. Barton, Progress in perceptual research: the case of prosopagnosia. *F1000Research* **8**, F1000 Faculty Rev-765 (2019).

32. R. Russell, B. C. Duchaine, K. Nakayama, Super-recognizers: People with extraordinary face recognition ability. *Psychon. Bull. Rev.* **16**, 252–257 (2009).

33. R. Russell, X. Yue, K. Nakayama, R. B. Tootell, Neural differences between developmental prosopagnosics and super-recognizers. *J. Vis.* **10**, 582–582 (2010).

34. A. K. Bobak, A. J. Dowsett, S. Bate, Solving the Border Control Problem: Evidence of Enhanced Face Matching in Individuals with Extraordinary Face Recognition Skills. *PLOS ONE* **11**, e0148148 (2016).

35. J. P. Davis, K. Lander, R. Evans, A. Jansari, Investigating Predictors of Superior Face Recognition Ability in Police Super-recognisers. *Appl. Cogn. Psychol.* **30**, 827–840 (2016).

36. A. K. Bobak, R. J. Bennetts, B. A. Parris, A. Jansari, S. Bate, An in-depth cognitive examination of individuals with superior face recognition skills. *Cortex* **82**, 48–62 (2016).

37. S. Bate, E. Portch, N. Mestry, R. J. Bennetts, Redefining super recognition in the real world: Skilled face or person identity recognizers? *Br. J. Psychol.*, 2017–2019 (2019).

38. M. Ramon, A. K. Bobak, D. White, Super-recognizers: From the lab to the world and back again. *Br. J. Psychol.* **0** (2019).

39. S. Cohan, K. Nakayama, B. C. Duchaine, Broadly Superior: Many, but not all, visual and non-visual abilities are strong in face super-recognizers. *J. Vis.* **16**, 74 (2016).

40. J. B. Wilmer, Individual Differences in Face Recognition: A Decade of Discovery. *Curr. Dir. Psychol. Sci.* **26**, 225–230 (2017).

41. N. G. Shakeshaft, R. Plomin, Genetic specificity of face recognition. *Proc. Natl. Acad. Sci.* **112**, 12887–12892 (2015).

42. J. B. Wilmer, *et al.*, Human face recognition ability is specific and highly heritable. *Proc. Natl. Acad. Sci.* **107**, 5238–5241 (2010).

43. J. M. DeGutis, C. Chiu, M. E. Grosso, S. Cohan, Face processing improvements in prosopagnosia: successes and failures over the last 50 years. *Front. Hum. Neurosci.* **8** (2014).

44. L. Germine, E. C. Dunn, K. A. McLaughlin, J. W. Smoller, Childhood Adversity Is Associated with Adult Theory of Mind and Social Affiliation, but Not Face Processing. *PLOS ONE* **10**, e0129612 (2015).

45. O. Wilhelm, *et al.*, Individual differences in perceiving and recognizing faces-One element of social cognition. *J. Pers. Soc. Psychol.* **99**, 530–548 (2010).

46. A. Hildebrandt, O. Wilhelm, F. Schmiedek, G. Herzmann, W. Sommer, On the Specificity of Face Cognition Compared With General Cognitive Functioning Across Adult Age. *Psychol. Aging* **26**, 701–715 (2011).

47. J. B. Wilmer, Individual Differences in Face Recognition: A Decade of Discovery. *Curr. Dir. Psychol. Sci.* **26**, 225–230 (2017).

48. G. E. Gignac, M. Shankaralingam, K. Walker, P. Kilpatrick, Short-term memory for faces relates to general intelligence moderately. *Intelligence* **57**, 96–104 (2016).

49. Q. Zhu, *et al.*, Heritability of the Specific Cognitive Ability of Face Perception. *Curr. Biol.* **20**, 137–142 (2010).

50. D. B. Elbich, S. Scherf, Beyond the FFA: Brain-behavior correspondences in face recognition abilities. *NeuroImage* **147**, 409–422 (2017).

51. N. Furl, L. Garrido, R. J. Dolan, J. Driver, B. C. Duchaine, Fusiform Gyrus Face Selectivity Relates to Individual Differences in Facial Recognition Ability. *J. Cogn. Neurosci.* **23**, 1723–1740 (2011).

52. L. Huang, *et al.*, Individual differences in cortical face selectivity predict behavioral performance in face recognition. *Front. Hum. Neurosci.* **8**, 1–10 (2014).

53. M. Ramot, C. Walsh, A. Martin, Multifaceted Integration: Memory for Faces Is Subserved by Widespread Connections between Visual, Memory, Auditory, and Social Networks. *J. Neurosci.* **39**, 4976 LP – 4985 (2019).

54. R. W. McGugin, I. Gauthier, The reliability of individual differences in face-selective responses in the fusiform gyrus and their relation to face recognition ability. *Brain Imaging Behav.* **10**, 707–718 (2016).

55. J. Li, *et al.*, Structural attributes of the temporal lobe predict face recognition ability in youth. *Neuropsychologia* **84**, 1–6 (2016).

56. D. B. Elbich, K. S. Scherf, Beyond the FFA: Brain-behavior correspondences in face recognition abilities. *NeuroImage* **147**, 409–422 (2017).

57. C. Westlin, *et al.*, Improving the study of brain-behavior relationships by revisiting basic assumptions. *Trends Cogn. Sci.* **27**, 246–257 (2023).

58. A. Mahmoudi, S. Takerkart, F. Regragui, D. Boussaoud, A. Brovelli, Multivoxel pattern analysis for fMRI data: A review. *Comput. Math. Methods Med.* **2012** (2012).

59. K. Jimura, R. A. Poldrack, Analyses of regional-average activation and multivoxel pattern information tell complementary stories. *Neuropsychologia* **50**, 544–552 (2012).

60. M. E. Weaverdyck, M. D. Lieberman, C. Parkinson, Tools of the Trade Multivoxel pattern analysis in fMRI: a practical introduction for social and affective neuroscientists. *Soc. Cogn. Affect. Neurosci.* **15**, 487–509 (2020).

61. D. Rivolta, *et al.*, Multi-voxel pattern analysis (MVPA) reveals abnormal fMRI activity in both the "core" and "extended" face network in congenital prosopagnosia. *Front. Hum. Neurosci.* **8** (2014).

62. S. Faghel-Soubeyrand, *et al.*, Multivariate pattern analysis reveals domain-general enhancement of visual representations in individuals with "super-recognition" of faces. *J. Vis.* **20**, 502–502 (2020).

63. S. Faghel-Soubeyrand, *et al.*, Decoding real-world visual recognition abilities in the human brain. *J. Vis.* **21**, 2604–2604 (2021).

64. M. D. Fox, M. E. Raichle, Spontaneous fluctuations in brain activity observed with functional magnetic resonance imaging. *Nat. Rev. Neurosci.* **8**, 700–711 (2007).

65. B. P. Rogers, V. L. Morgan, A. T. Newton, J. C. Gore, Assessing functional connectivity in the human brain by fMRI. *Magn. Reson. Imaging* **25**, 1347–1357 (2007).

66. M. P. van den Heuvel, H. E. Hulshoff Pol, Exploring the brain network: A review on resting-state fMRI functional connectivity. *Eur. Neuropsychopharmacol.* **20**, 519–534 (2010).

67. K. J. Friston, Functional and Effective Connectivity: A Review. *Brain Connect.* **1**, 13–36 (2011).

68. E. S. Finn, *et al.*, Functional connectome fingerprinting: Identifying individuals using patterns of brain connectivity. *Nat. Neurosci.* **18**, 1664–1671 (2015).

69. S. Gao, A. S. Greene, R. T. Constable, D. Scheinost, Combining multiple connectomes improves predictive modeling of phenotypic measures. *NeuroImage* **201**, 116038 (2019).

70. C. Horien, X. Shen, D. Scheinost, R. T. Constable, The individual functional connectome is unique and stable over months to years. *NeuroImage* **189**, 676–687 (2019).

71. E. S. Finn, *et al.*, Functional connectome fingerprinting: identifying individuals using patterns of brain connectivity. *Nat. Neurosci.* **18**, 1664–1671 (2015).

72. K. Yoo, *et al.*, Connectome-based predictive modeling of attention: Comparing different functional connectivity features and prediction methods across datasets. *NeuroImage* **167**, 11–22 (2018).

73. X. Shen, *et al.*, Using connectome-based predictive modeling to predict individual behavior from brain connectivity. *Nat. Protoc.* **12**, 506–518 (2017).

74. N. U. F. Dosenbach, *et al.*, Prediction of Individual Brain Maturity Using fMRI. *Science* **329**, 1358 LP – 1361 (2010).

75. H. W. Dennett, *et al.*, The Cambridge Car Memory Test: A task matched in format to the Cambridge Face Memory Test, with norms, reliability, sex differences, dissociations from face memory, and expertise effects. *Behav. Res. Methods* **44**, 587–605 (2012).

76. D. H. Brainard, The psychophysics toolbox. *Spat. Vis.* **10**, 433–436 (1997).

77. D.-B. Ćepulić, O. Wilhelm, W. Sommer, A. Hildebrandt, All categories are equal, but some categories are more equal than others: The psychometric structure of object and face cognition. *J. Exp. Psychol. Learn. Mem. Cogn.* **44**, 1254–1268 (2018).

78. A. Klin, D. J. Lin, P. Gorrindo, G. Ramsay, W. Jones, Two-year-olds with autism orient to non-social contingencies rather than biological motion. *Nature* **459**, 257–261 (2009).

79. C. A. Meissner, C. G. Tredoux, J. F. Parker, O. H. MacLin, Eyewitness decisions in simultaneous and sequential lineups: A dual-process signal detection theory analysis. *Mem. Cognit.* **33**, 783–792 (2005).

80. M. E. Nilsback, A. Zisserman, Automated flower classification over a large number of classes in *Proceedings - 6th Indian Conference on Computer Vision, Graphics and Image Processing, ICVGIP 2008*, (2008), pp. 722–729.

81. V. Willenbockel, *et al.*, Controlling low-level image properties: The SHINE toolbox. *Behav. Res. Methods* **42**, 671–684 (2010).

82. W. Revelle, psych: Procedures for Psychological, Psychometric, and Personality Research (2018).

83. C. Pallier, "Computing discriminability and bias with the R software" (2002).

84. D. Makowski, The Psycho Package: An Efficient and Publishing-Oriented Workflow for Psychological Science. *J. Open Source Softw.* **3**, 470 (2018).

85. M. L. Elliott, *et al.*, What Is the Test-Retest Reliability of Common Task-Functional MRI Measures? New Empirical Evidence and a Meta-Analysis. *Psychol. Sci.* **31**, 792–806 (2020).

86. E. J. Burns, E. Gaunt, B. Kidane, L. Hunter, J. Pulford, A new approach to diagnosing and researching developmental prosopagnosia: Excluded cases are impaired too. *Behav. Res. Methods*, 1–24 (2022).

87. E. Murray, S. Bate, Diagnosing developmental prosopagnosia: repeat assessment using the Cambridge Face Memory Test. *R. Soc. Open Sci.* **7**, 200884 (2020).

88. S. Haufe, *et al.*, On the interpretation of weight vectors of linear models in multivariate neuroimaging. *NeuroImage* **87**, 96–110 (2014).

89. N. Kriegeskorte, P. K. Douglas, Interpreting encoding and decoding models. *Mach. Learn. Big Data Neurosci.* **55**, 167–179 (2019).

90. B. Duchaine, K. Nakayama, The Cambridge Face Memory Test: Results for neurologically intact individuals and an investigation of its validity using inverted face stimuli and prosopagnosic participants. *Neuropsychologia* **44**, 576–585 (2006).

91. R. J. Robotham, R. Starrfelt, Tests of whole upright face processing in prosopagnosia: A literature review. *Neuropsychologia* **121**, 106–121 (2018).

92. S.-J. Cho, *et al.*, Item response theory analyses of the Cambridge Face Memory Test (CFMT). *Psychol. Assess.* **27**, 552–566 (2015).

93. A. Abraham, *et al.*, Machine learning for neuroimaging with scikit-learn. *Front. Neuroinformatics* **8** (2014).

94. G. H. Glover, Deconvolution of Impulse Response in Event-Related BOLD fMRI1. *NeuroImage* **9**, 416–429 (1999).

95. T. Yarkoni, R. A. Poldrack, T. E. Nichols, D. C. Van Essen, T. D. Wager, Large-scale automated synthesis of human functional neuroimaging data. *Nat. Methods* **8**, 665–670 (2011).

96. F. Pedregosa, *et al.*, Scikit-learn: Machine Learning in Python. *J. Mach. Learn. Res.* **12**, 2825–2830 (2011).

97. D. J. Benjamin, *et al.*, Redefine statistical significance. *Nat. Hum. Behav.* **2**, 6–10 (2018).

98. M. P. Notter, *et al.*, AtlasReader: A Python package to generate coordinate tables, region labels, and informative figures from statistical MRI images. *J. Open Source Softw.* **4**, 1257 (2019).

99. X. Shen, F. Tokoglu, X. Papademetris, R. T. Constable, Groupwise whole-brain parcellation from resting-state fMRI data for network node identification. *NeuroImage* **82**, 403–415 (2013).

100. J. W. Cho, A. Korchmaros, J. T. Vogelstein, M. P. Milham, T. Xu, Impact of concatenating fMRI data on reliability for functional connectomics. *NeuroImage* **226**, 117549 (2021).

Figures and Tables

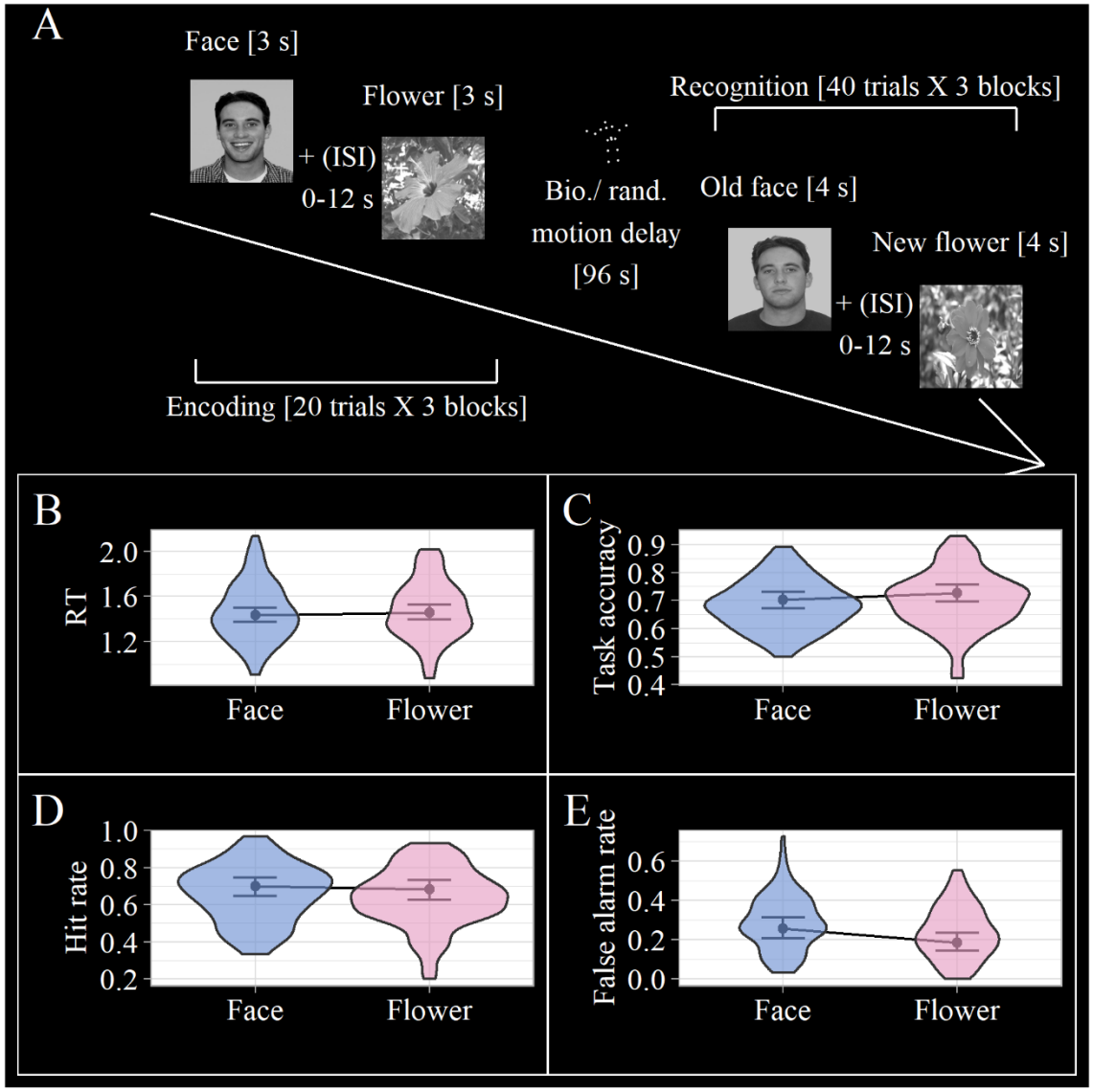

Figure 1. Experimental design and task performance is well-balanced across the two stimulus classes (faces and flowers). Panel A shows stimulus presentation times and overall paradigm structure for both the encoding (60 trials) and recognition phase (120 trials). The violin plots display the density of marginal participant averages for each respective outcome variable overlaid with the posterior parameter estimates. Panel B shows that RTs are well matched across the two stimulus classes. Panels C, D, and E show that recognition rates are similar across the two classes, with a slightly higher level of false alarms for faces. However, the WAIC difference of 3.4 in favor of the null model indicates that there is no substantial difference in false alarms across faces and flowers. This suggests that the structure and performance is well-matched across both stimulus classes, affording the possibility of making domain-specific claims on imaging contrasts between faces and flowers.

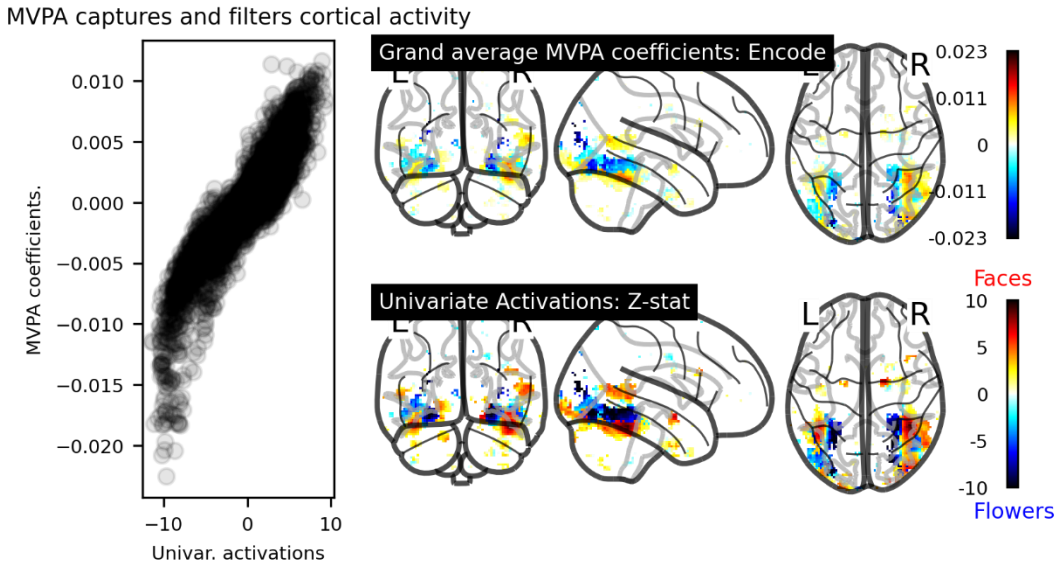

Figure 2. Visualization and replication of previous work showing canonical activation patterns for faces relative to non-face stimuli. Here, we are showing the MVPA decoding coefficients of the classification model (standardized penalized logistic regression) during the encoding phase (recognition phase shows similar pattern structure), as well as the univariate activations of the face – flower contrast. There is significantly more lateral and less medial fusiform gyrus activation for faces and flowers, as well as significant differences in other cortical (e.g., lateral occipital cortex) and subcortical (e.g., amygdala) structures reported in Table S3 and Table S4. There is a high correlation between MVPA decoding coefficients, suggesting that MVPA both represents and filters cortical activation for this specific model. This penalization filter is important, because it downweighs redundant information from voxels within this ROI, highlighting the voxels that are uniquely important. While it is important to be careful when interpreting decoding coefficients, this demonstrates that for this specific application decoding coefficients may be more informative than traditional univariate activations because of its filtered representation of information.

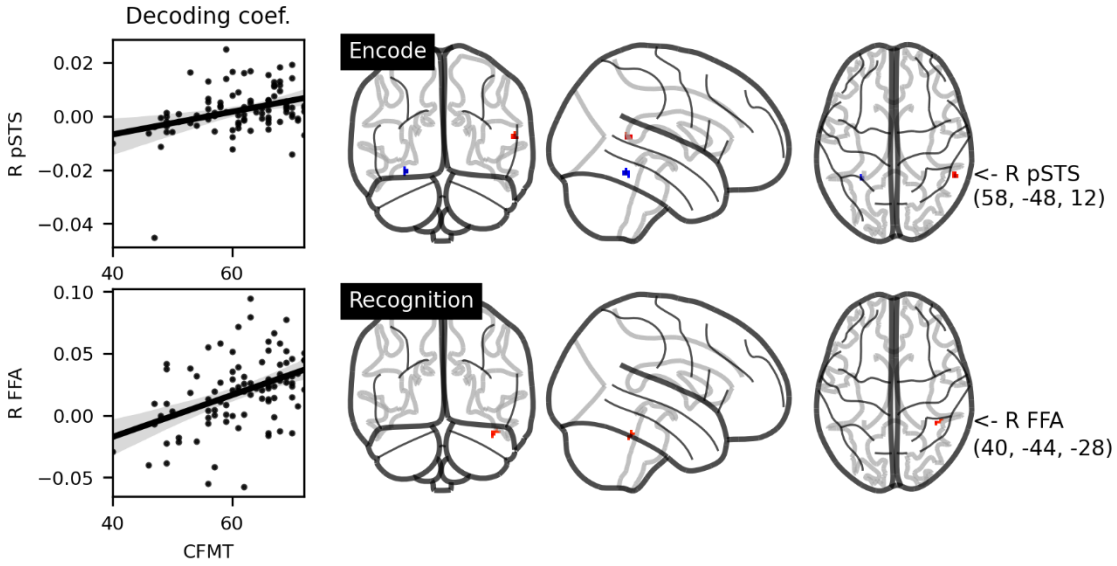

Figure 3. Cluster analysis suggests that the regions driving the relationship between decoding performance and CFMT are voxels within the core face network. Specifically, right pSTS was important for distinguishing the two stimulus classes for stronger face recognizers at encoding, and r FFA at recognition. All clusters are reported in Table 2, including the correlates with Face d' (no correlates detected with Flower d').

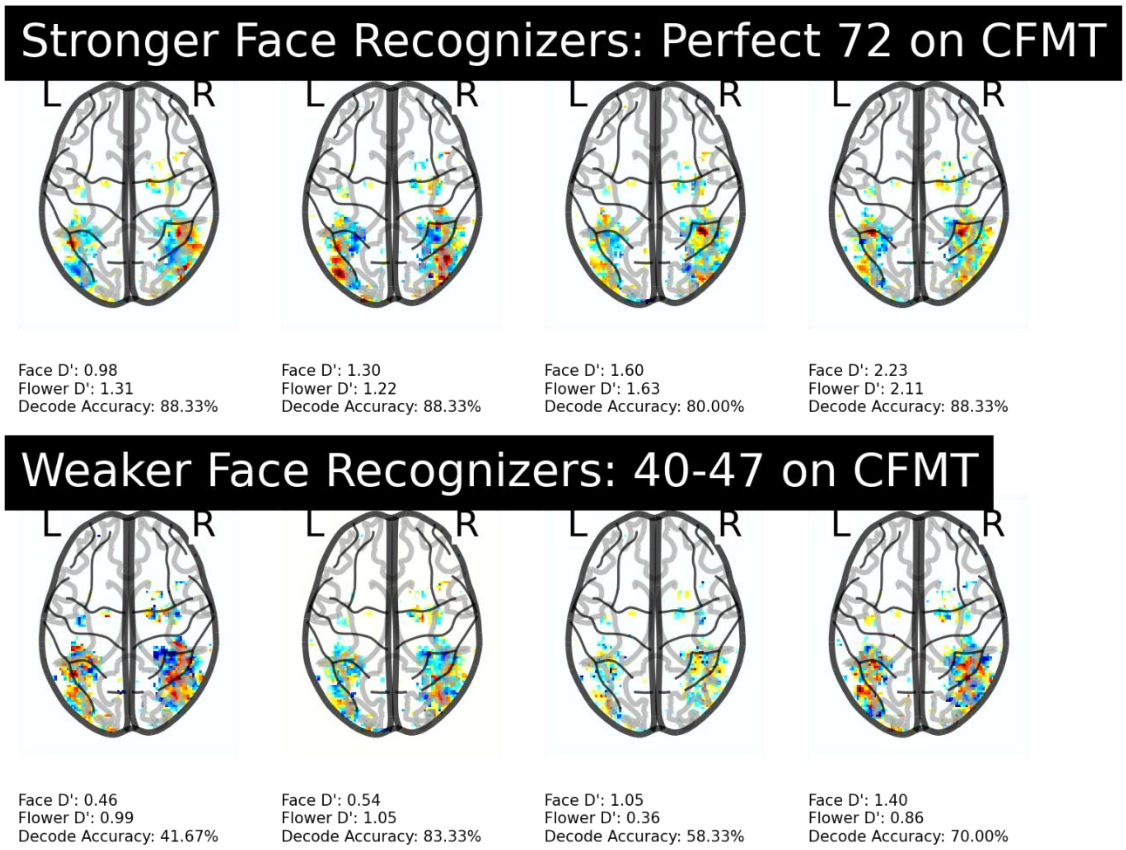

Figure 4. Exploratory visualization of stronger and weaker face recognizers suggests different cortical representations in our tested ROI. Each brain panel is a different individual with their decoding coefficients during the encoding phase overlaid. Stronger face recognizers seem to have more well-defined and modular FFAs, as well as better respect for the medial-to-lateral functional subdivision of fusiform cortex with respect to objects vs. face processing. Weaker face recognizers seem to have less-defined decision boundaries that tend to be overlapping and diffuse across these cortical regions. Signal detection summary statistics of performance indicate that all participants were paying attention in the scanner, such that lack of attention cannot explain the fuzzy and coarse MVPA representations of weaker face recognizers.

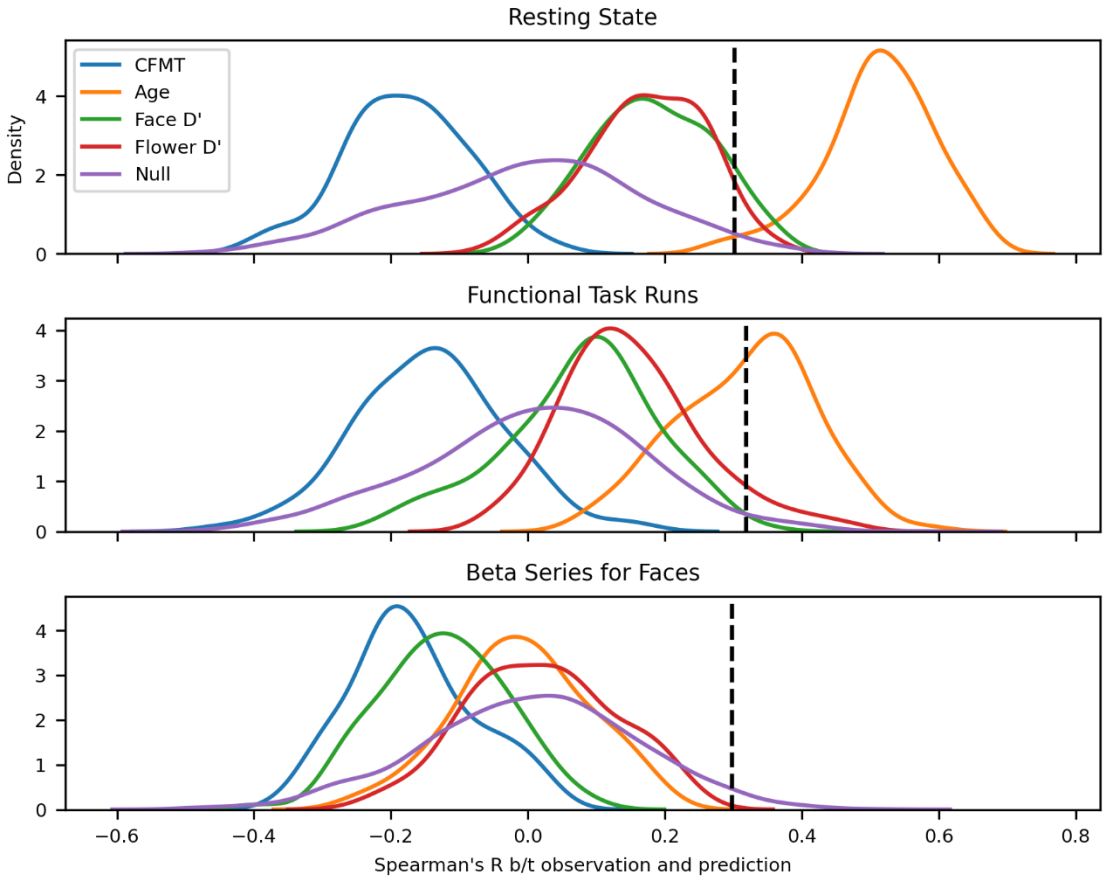

Figure 5. rCPM cannot predict face recognition behavior at rest, during task, or with face-specific activations. As a validation control, we demonstrate that age can be predicted from the resting-state run and the functional task runs separately. The vertical dashed lines indicate the point estimate of the 97.5% quantile for the null distribution. If the median of an outcome variable distribution exceeds this value, the model is considered "significant" and able to predict the phenotype of interest. For visual simplicity, the null distribution is generated from only a permuted CFMT score, rather than plotting an individual null distribution for each outcome variable. CFMT, Face d', and Flower d' are not predicted by any of the three functional imaging inputs.

Table 1. Decoding rates within ROI for faces relative to flowers is uniquely associated with face recognition ability (CFMT), controlling for signal detection metrics and demographics.

	Decode: Encoding		**Decode: Recognition**	
Predictors	*Estimates*	*CI (95%)*	*Estimates*	*CI (95%)*
Intercept	1.51	1.37 – 1.66	1.84	1.70 – 1.97
CFMT	**0.21**	**0.08 – 0.34**	**0.14**	**0.02 – 0.26**
Face d'	0.05	-0.11 – 0.21	0.12	-0.02 – 0.27
Flower d'	0.09	-0.06 – 0.24	0.07	-0.06 – 0.21
Face C	0.07	-0.06 – 0.20	**0.18**	**0.06 – 0.30**
Flower C	-0.00	-0.14 – 0.14	-0.05	-0.18 – 0.08
Age	0.03	-0.10 – 0.16	**0.16**	**0.03 – 0.28**
Sex (Female)	-0.04	-0.18 – 0.09	-0.06	-0.19 – 0.06
Hand	-0.05	-0.40 – 0.33	0.11	-0.23 – 0.48

Table 2. Identified clusters with face recognition metrics reveal positive relationships within core face network regions (R pSTS, R FFA, L OFA; bolded in table) and negative relationships with object-sensitive medial fusiform cortex.

X	*Y*	*Z*	*Mean (Z)*	*Volume (mm)*	*Anatomical Label*	*Top Neurosynth Terms*
CMFT:	*Encode*					
58	**-48**	**12**	**3.17**	**112**	**R Superior Temporal Sulcus**	**temporal sulcus, posterior superior, psts**
-30	-48	-16	-3.30	96	L Fusiform Gyrus	fusiform, fusiform gyrus, objects
CFMT:	*Recog.*					
40	**-44**	**-28**	**2.91**	**80**	**R Fusiform Gyrus**	**face, ffa, fusiform**
Face d':	*Encode*					
-40	**-88**	**-8**	**3.38**	**272**	**L Lateral Occipital Cortex**	**fusiform face, face ffa, ffa**
26	-80	-12	-3.01	88	R Fusiform Gyrus	visual, occipital, occipito
Face d':	*Recog.*					
-38	**-92**	**-10**	**2.99**	**80**	**L Lateral Occipital Cortex**	**faces, face, inferior occipital**

Supporting Information for Chapter 1: Accuracy of fMRI decoding maps for faces in domain-specific brain regions relate to individual differences in face recognition ability

Methods

Bayesian generalized linear models for statistical inference on behavior

We used the *brms* software package in R and the state-of-the-art Hamiltonian Monte-Carlo No-U-Turn sampler (NUTS) for Bayesian computation and inference on behavior (1, 2). Default priors on all the likelihood family-specific parameters were used, and soft regularization priors were used, generated by $\beta \sim N(\mu = 0, \sigma = 10)$ on the population-level regression coefficients. We ran 5 independent Markov chains each with 10,000 total iterations, including 5,000 warm-up iterations, resulting in 25,000 posterior samples total for each model. We fixed the target average proposal acceptance probability to 99% to improve the quality of sampling and thus the resulting posterior distributions. Convergence of the posteriors were confirmed with all $\hat{R} \approx 1.0$, which assesses agreement across the Markov chains. Posterior predictive checks were used to assess model adequacy (see Fig. S4) (3).

There were several motivating factors for using Bayesian techniques for the current research. First, we applied regularization priors to the regression coefficients as a way to employ shrinkage and mitigate potential for over-fitting. Second, we modelled hierarchy through probability distributions which allows for accurate estimation of subject-specific and item-specific parameters, which we used to estimate intercepts and repeated-measurements slopes for each participant, as well as intercepts for items, when applicable. Third, we had explicit control over the probability distribution of the likelihood. This allowed us to use more robust techniques for capturing a better fit to the outcomes variables of interest including Bernoulli (trial-level accuracy, hits, and false-alarms; i.e., logistic regression), Shifted Lognormal (reaction time), Truncated Normal (CFMT: 0-72 bound), Skew Normal (d' and C), and Multivariate Beta (subject-level MVPA decoding rates for encoding and recognition phase). Overall, these three factors generally lead to more conservative and robust inference relative to the Frequentist approach (4). Importantly, some of these exact model specifications require Bayesian sampling-based approaches rather than optimization-based techniques given there is scarce software support or implementation applying some of these specific Frequentist optimization problems.

For each behavioral model, posterior distributions on the stimulus class parameters were inspected. Statistical inference for no difference between faces and flowers was a two-step process. First, we tested if the 95% credible interval (the Bayesian alternative to Frequentist confidence intervals) did not overlap with 0, which would suggest a potential difference between the two stimulus classes with that particular outcome variable. If there was no overlap with 0, we fit a model without the stimulus class term and used the Widely Applicable Information Criterion to determine which model fit the data better (5). We report the difference in fit between these models by examining the log pointwise-predictive density to determine if there was a substantial

difference in that variable across the two stimulus classes. Ultimately, the model with the lower WAIC was considered better for the balance between the tradeoff of fit and parsimony. In all Bayesian behavioral models, we controlled for potential age and sex differences by fitting age as an additive term and sex as a multiplicative term with stimulus class. This multiplicative term allows for overall differences in performance between men and women, as well as potential sex differences in performance between the two stimulus classes. This is important, because the recognition task for faces only included male faces, and the selection of flowers could result in plausible differences in task performance across sex, as could be expected for other stimulus classes (e.g., cars).

Imaging parameters and acquisition.

MRI scanning was performed at the University of Virginia Fontaine Research Park on a Siemens 3 Tesla MAGNETOM Prisma Fit high-speed imaging device equipped with a 32-channel head-coil. First, high-resolution T1-weighted anatomical images were acquired using Siemens' magnetization-prepared rapid-acquired gradient echo (MPRAGE) pulse sequence with the following specifications: echo time (TE) = 2.98 ms; repetition time (TR) = 2300 ms; flip angle (FA) = 9°; image matrix = 240 mm × 256 mm; slice thickness = 1 mm; 208 slices. Then, whole-brain functional images were acquired using a T2*-weighted echo planar imaging (EPI) sequence sensitive to BOLD contrast with the following specifications: TE = 30 ms; TR = 800 ms; FA = 52°; image matrix = 90 mm x 90 mm; slice thickness = 2.4 mm; slice gap = 2.4 mm; 660 slices. Stimuli were presented using an LCD AVOTEC projector onto a screen located behind the participant's head and viewed through an integrated head-coil mirror.

Imaging preprocessing with fMRIPrep

Results included in this chapter come from preprocessing performed using *fMRIPrep* 21.0.0rc1 (6) which is based on *Nipype* 1.6.1 (RRID:SCR_002502) (7). Many internal operations of *fMRIPrep* use *Nilearn* 0.8.1 (8), mostly within the functional processing workflow. For each participant, the T1-weighted (T1w) image was corrected for intensity non-uniformity (INU) with N4BiasFieldCorrection (9), distributed with ANTs 2.3.3 (RRID:SCR_004757) (10), and used as T1w-reference throughout the workflow. The T1w-reference was then skull-stripped with a *Nipype* implementation of the antsBrainExtraction.sh workflow (from ANTs), using OASIS30ANTs as target template. Brain tissue segmentation of cerebrospinal fluid (CSF), white-matter (WM) and gray-matter (GM) was performed on the brain-extracted T1w using fast (FSL 5.0.11, RRID:SCR_002823) (11). Volume-based spatial normalization to one standard space (MNI152NLin2009cAsym) was performed through nonlinear registration with antsRegistration (ANTs 2.3.3), using brain-extracted versions of both T1w reference and the T1w template. The following template was selected for spatial normalization: *ICBM 152 Nonlinear Asymmetrical template version 2009c* [RRID:SCR_008796; TemplateFlow ID: MNI152Nlin2009cAsym] (12).

For each of the BOLD runs per subject, the following preprocessing was performed. First, a reference volume and its skull-stripped version were generated using a

custom methodology of *fMRIPrep*. BOLD runs were slice-time corrected to 0.351s (0.5 of slice acquisition range 0s-0.703s) using 3dTshift from AFNI (RRID:SCR_005927) (13). Head-motion parameters with respect to the BOLD reference (transformation matrices, and six corresponding rotation and translation parameters) were estimated before any spatiotemporal filtering using mcflirt (FSL 5.0.11) (14). The BOLD reference was then co-registered to the T1w reference using flirt (FSL 5.0.11) (15) with the boundary-based registration (16) cost-function. Co-registration was configured with nine degrees of freedom to account for distortions remaining in the BOLD reference. The BOLD time-series (including slice-timing correction when applied) were resampled onto their original, native space by applying the transforms to correct for head-motion. These resampled BOLD time-series will be referred to as *preprocessed BOLD in original space*, or just *preprocessed BOLD*. The BOLD time-series were resampled into standard space, generating a *preprocessed BOLD run in MNI152Nlin2009cAsym space*. Several confounding time-series were calculated based on the *preprocessed BOLD*: framewise displacement (FD), DVARS and three region-wise global signals. FD was computed using two formulations following Power (absolute sum of relative motions (17)) and Jenkinson (relative root mean square displacement between affines (14)). FD and DVARS are calculated for each functional run, both using their implementations in *Nipype* (17). The three global signals are extracted within the CSF, the WM, and the whole-brain masks. Additionally, a set of physiological regressors were extracted to allow for component-based noise correction (*CompCor*) (18). Principal components are estimated after high-pass filtering the *preprocessed BOLD* time-series (using a discrete cosine filter with 128s cut-off) for the two *CompCor* variants: temporal (tCompCor) and anatomical (aCompCor). tCompCor components are then calculated from the top 2% variable voxels within the brain mask. For aCompCor, three probabilistic masks (CSF, WM and combined CSF+WM) are generated in anatomical space. The implementation differs (18) in that instead of eroding the masks by 2 pixels on BOLD space, the aCompCor masks are subtracted a mask of pixels that likely contain a volume fraction of GM. This mask is obtained by thresholding the corresponding partial volume map at 0.05, and it ensures components are not extracted from voxels containing a minimal fraction of GM. Finally, these masks are resampled into BOLD space and binarized by thresholding at 0.99 (as in the original implementation). Components are also calculated separately within the WM and CSF masks. For each CompCor decomposition, the *k* components with the largest singular values are retained, such that the retained components' time series are sufficient to explain 50 percent of variance across the nuisance mask (CSF, WM, combined, or temporal). The remaining components are dropped from consideration. The head-motion estimates calculated in the correction step were also placed within the corresponding confounds file. The confound time series derived from head motion estimates and global signals were expanded with the inclusion of temporal derivatives and quadratic terms for each (19). Frames that exceeded a threshold of 0.5 mm FD or 1.5 standardized DVARS were annotated as motion outliers. All resamplings can be performed with *a single interpolation step* by composing all the pertinent transformations (i.e., head-motion transform matrices, susceptibility distortion correction when available, and co-registrations to anatomical and output spaces). Gridded (volumetric) resamplings were performed using antsApplyTransforms (ANTs), configured with Lanczos interpolation to minimize the smoothing effects of other kernels

(20). For GLM-based and connectivity-based analysis, functional images were high-pass filtered at .008 Hz using 3 drift components with polynomial bases and cleaned with the following fMRIPrep confound derivatives to account for global BOLD signal outside of gray matter (csf, white_matter), primary data-driven estimated noise components (tcompcor, a_comp_cor_00, a_comp_cor_01) and motion-related parameters (trans_x, trans_x_power2, trans_y, trans_y_power2, trans_z, trans_z_power2, rot_x, rot_x_power2, rot_y, rot_y_power2, rot_z, rot_z_power2).

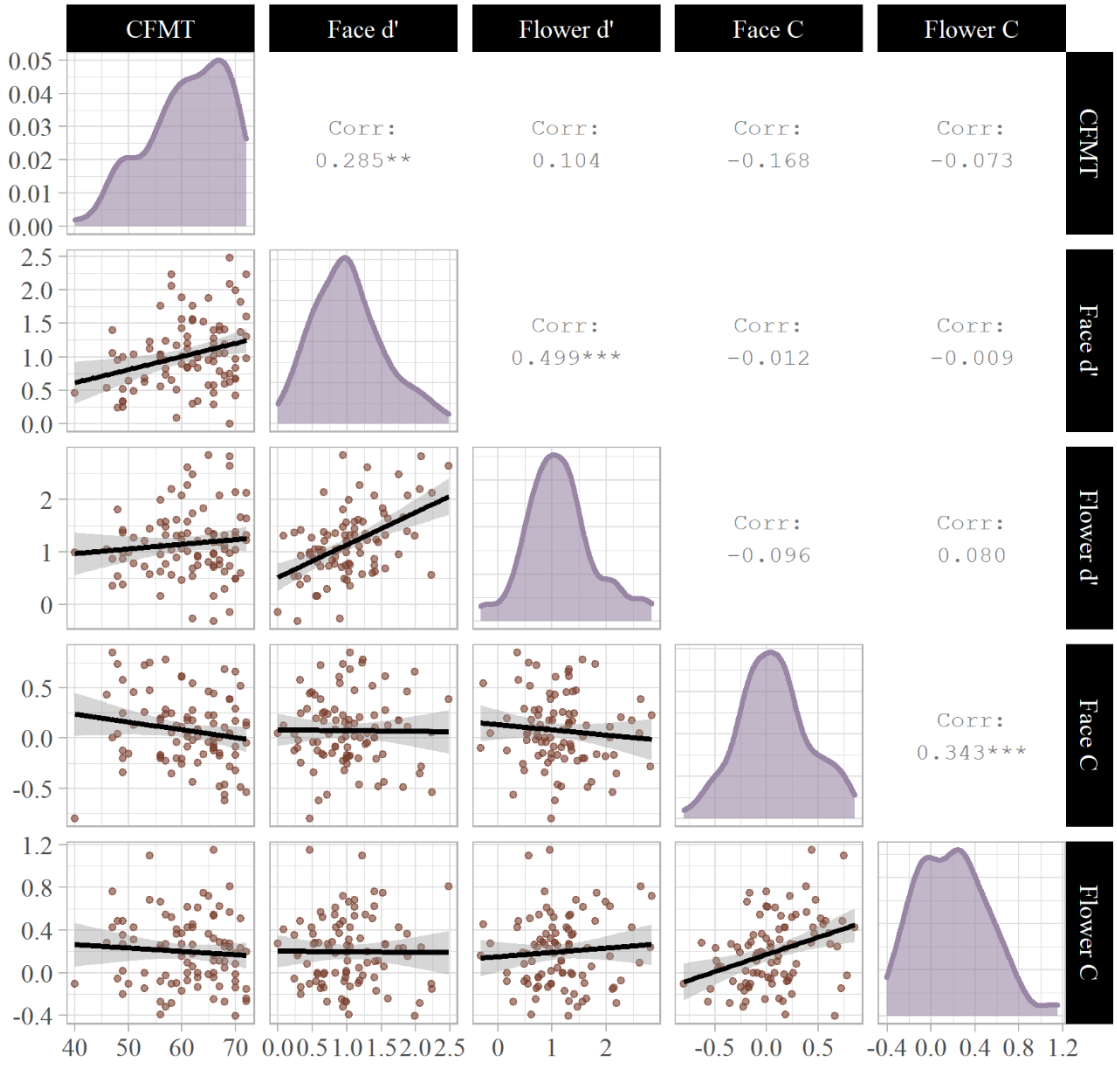

Fig. S1. Distributions and correlations between CFMT and in-scanner signal detection metrics. Across the two stimulus classes, d' and C are both positively correlated. Only Face d' is positively correlated with CFMT. The model from Table S2 suggests that this relationship is unique variance not attributable to other signal detection metrics or demographics.

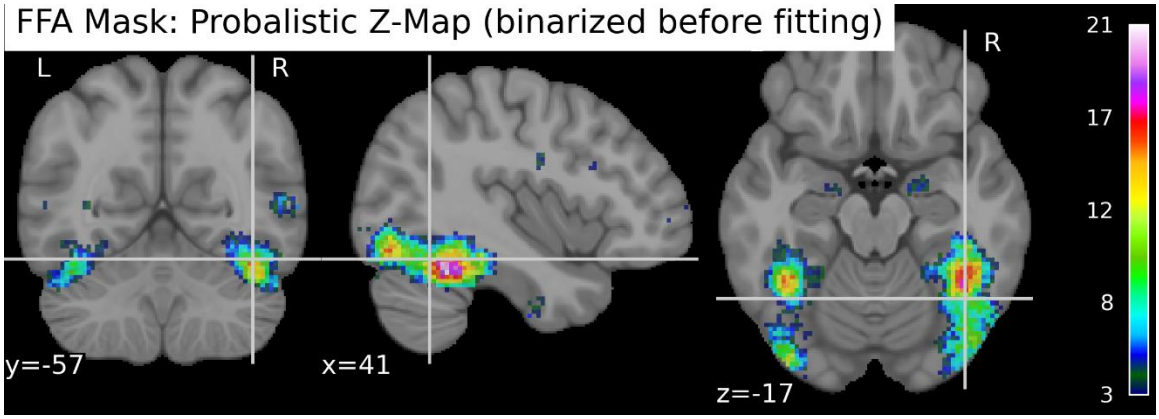

Fig. S2. Visualization of ROI mask derived from Neurosynth (keyword: “ffa”). Contrary with the suggestion of the keyword name, this mask contains voxels that are preferential for both faces and non-face stimuli (see Fig. S3).

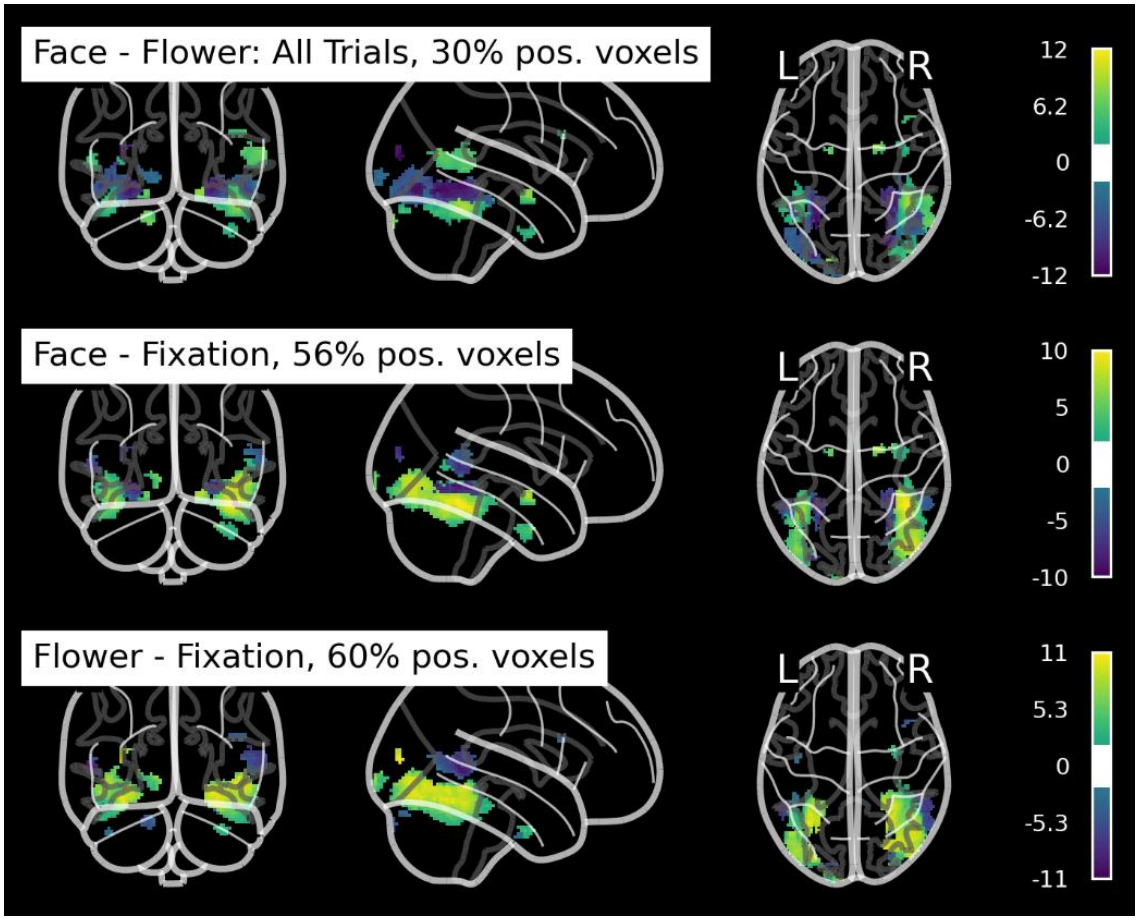

Fig. S3. Evidence that the "ffa" ROI mask includes many voxels that are not face-specific. This ROI mask casts a wide net across higher-order visual cortex and relevant sub-cortical structures that are important both for face and "object" processing. The number of significant voxels for faces and for flowers is relatively balanced within this voxel mask.

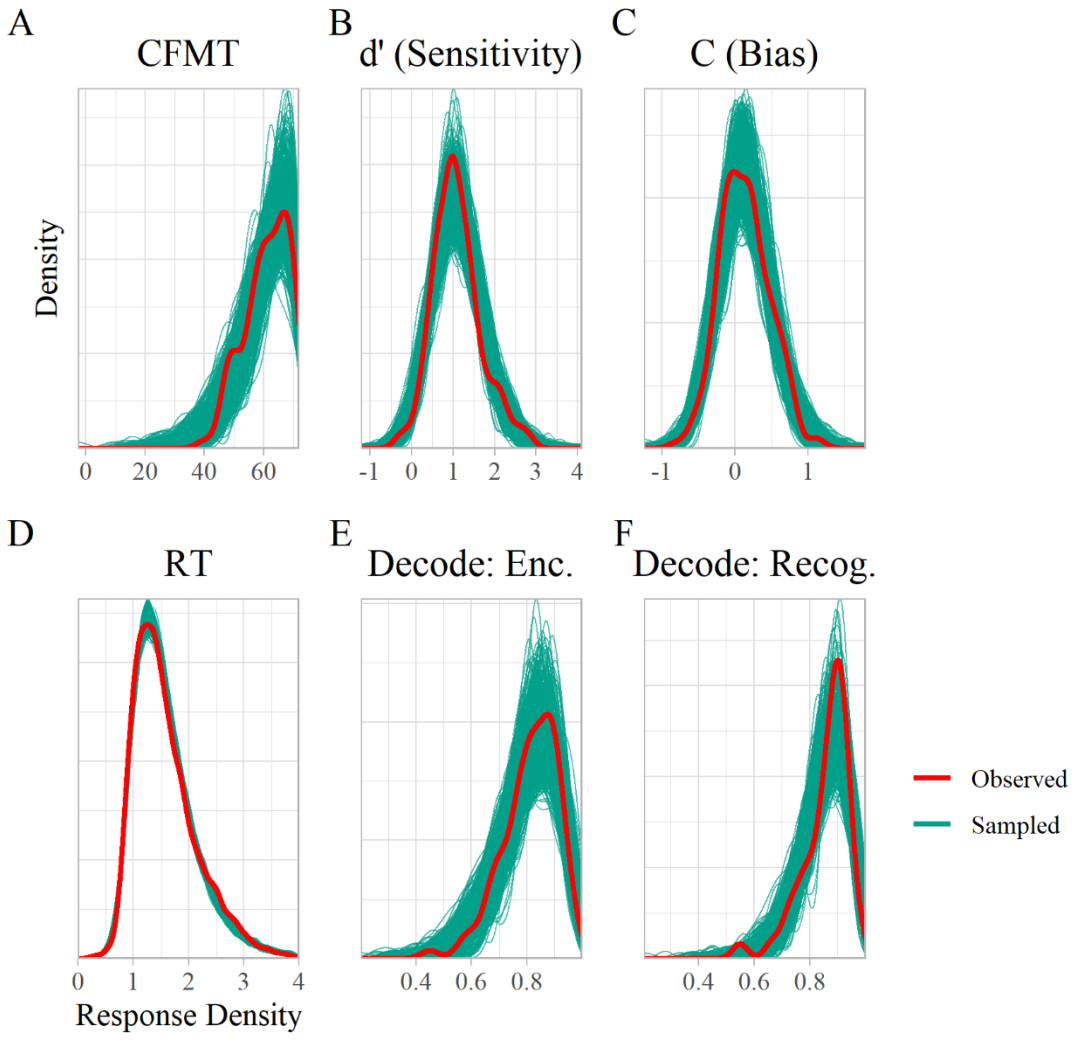

Fig. S4. Posterior predictive distribution checks of all continuous outcome variables indicate sufficient model specification for Bayesian inference. Appropriate likelihood functions were used to fit CFMT (truncated Gaussian w/ upper bound of 72), d'/ C (skew normal), RT (shifted lognormal), and decoding accuracy for both task phases (multivariate beta). The posterior stimulus class parameters for the discrete outcomes (task accuracy, hits, false alarms) are shown in Figure 1 in the main manuscript.

Table S1. Hierarchical Bayesian logistic regression fits suggest that recognition rates are similar across the two classes, with a slightly higher level of false alarms for faces (WAIC difference of 3.4 in favor null model), indicating that there is no substantial difference in false alarms across faces and flowers.

	Hits		**False Alarms**	
Predictors	*Log-Odds*	*CI (95%)*	*Log-Odds*	*CI (95%)*
Intercept	0.57	-0.38 – 1.54	-0.41	-1.42 – 0.58
Stimulus Class (Face)	0.05	-0.09 – 0.19	**0.18**	**0.02 – 0.35**
Sex (Female)	0.14	-0.01 – 0.28	-0.03	-0.18 – 0.12
Age	0.00	-0.04 – 0.05	-0.04	-0.08 – 0.01
Random Effects				
σ^2	3.29		3.29	
τ_{00}	0.33 Stimulus ID		0.53 Stimulus ID	
	0.35 Participant		0.38 Participant	
τ_{11}	0.08 Stimulus class slope		0.13 Stimulus class slope	
ρ_{01}				
ρ_{01}				
ICC	0.19		0.24	
N	92 Participants			
	120 Unique stimuli			
Observations	5427		5399	
Marginal R^2 / Conditional R^2	0.007 / 0.128		0.147 / 0.147	

Table S2. Face d' is the only signal detection metric calculated from in-scanner performance that positively associates with CFMT, suggesting that the face trials engage a cognitive process dissociable from general recognition capacities.

	CFMT | truncated(upper bound=72)	
Predictors	*Estimates*	*CI (95%)*
Intercept	68.69	63.16 – 84.27
Face d'	**5.47**	**1.14 – 11.82**
Flower d'	-1.12	-5.90 – 3.54
Face C	-2.81	-7.81 – 1.33
Flower C	0.24	-4.32 – 4.91
Age	-0.65	-5.15 – 3.71
Sex (Female)	1.79	-2.32 – 6.47
R^2 Bayes	0.162	

Table S3. Significant univariate activation for face > flower contrast includes regions canonically involved in the core face-processing network in the lateral areas of the fusiform gyrus and lateral occipital cortex, superior temporal sulcus, and amygdala.

X	*Y*	*Z*	*Mean (Z)*	*Volume (mm)*	*Anatomical Label*
44	-46	-24	4.36	8624	R Fusiform Gyrus
-40	-46	-20	3.73	3256	L Fusiform Gyrus
60	-62	14	5.47	2616	R Middle Temporal Gyrus, Superior Temporal Sulcus
-54	-46	2	4.65	584	L Middle Temporal Gyrus, Superior Temporal Sulcus
36	-2	-40	2.98	480	R Inferior Temporal Gyrus
20	-4	-14	6.17	464	R Amygdala, (Para)-hippocampal Cortex
-34	-56	6	3.05	192	L Cerebral White Matter
-20	-92	-30	7.24	168	L Cerebellum
44	18	22	5.18	168	R Inferior Frontal Gyrus
-18	-8	-16	6.46	112	L Amygdala, (Para)-hippocampal Cortex
-38	-92	-14	2.51	96	L Lateral Occipital Cortex

Table S4. Significant univariate activation for flower > face contrast includes regions canonically involved in object recognition in the medial areas of the fusiform gyrus and lateral occipital cortex.

X	*Y*	*Z*	*Mean (Z)*	*Volume (mm)*	*Anatomical Label*
24	-78	-12	-6.52	6936	R Fusiform Gyrus
-28	-64	-12	-7.18	3560	L Fusiform Gyrus
-30	-80	-8	-4.92	3456	L Lateral Occipital Cortex
-10	-104	-2	-3.92	360	L Occipital Pole
-34	-88	10	-11.4	136	L Middle Occipital Gyrus
-34	-70	-18	-3.77	128	L Fusiform Gyrus
48	-82	2	-2.96	96	R Lateral Occipital Cortex

SI References

1. P. C. Bürkner, brms: An R package for Bayesian multilevel models using Stan. *J. Stat. Softw.* **80** (2017).

2. M. D. Hoffman, A. Gelman, The no-U-turn sampler: Adaptively setting path lengths in Hamiltonian Monte Carlo. *J. Mach. Learn. Res.* **15** (2014).

3. D. J. Schad, M. Betancourt, S. Vasishth, Toward a principled Bayesian workflow in cognitive science. *Psychol. Methods* **26** (2021).

4. S. Theodoridis, *Machine Learning: A Bayesian and Optimization Perspective* (2015) https:/doi.org/10.1016/C2013-0-19102-7.

5. S. Watanabe, A Widely Applicable Bayesian Information Criterion. *J Mach Learn Res* **14**, 867–897 (2013).

6. O. Esteban, *et al.*, fMRIPrep: a robust preprocessing pipeline for functional MRI. *Nat. Methods* **16**, 111–116 (2019).

7. K. Gorgolewski, *et al.*, Nipype: A Flexible, Lightweight and Extensible Neuroimaging Data Processing Framework in Python. *Front. Neuroinformatics* **5** (2011).

8. A. Abraham, *et al.*, Machine learning for neuroimaging with scikit-learn. *Front. Neuroinformatics* **8** (2014).

9. N. J. Tustison, *et al.*, N4ITK: Improved N3 Bias Correction. *IEEE Trans. Med. Imaging* **29**, 1310–1320 (2010).

10. B. B. Avants, C. L. Epstein, M. Grossman, J. C. Gee, Symmetric diffeomorphic image registration with cross-correlation: Evaluating automated labeling of elderly and neurodegenerative brain. *Spec. Issue Third Int. Workshop Biomed. Image Regist. – WBIR 2006* **12**, 26–41 (2008).

11. Y. Zhang, M. Brady, S. Smith, Segmentation of brain MR images through a hidden Markov random field model and the expectation-maximization algorithm. *IEEE Trans. Med. Imaging* **20**, 45–57 (2001).

12. V. Fonov, A. Evans, R. McKinstry, C. Almli, D. Collins, Unbiased nonlinear average age-appropriate brain templates from birth to adulthood. *Organ. Hum. Brain Mapp. 2009 Annu. Meet.* **47**, S102 (2009).

13. R. W. Cox, J. S. Hyde, Software tools for analysis and visualization of fMRI data. *NMR Biomed.* **10**, 171–178 (1997).

14. M. Jenkinson, P. Bannister, M. Brady, S. Smith, Improved Optimization for the Robust and Accurate Linear Registration and Motion Correction of Brain Images. *NeuroImage* **17**, 825–841 (2002).

15. M. Jenkinson, S. Smith, A global optimisation method for robust affine registration of brain images. *Med. Image Anal.* **5**, 143–156 (2001).

16. D. N. Greve, B. Fischl, Accurate and robust brain image alignment using boundary-based registration. *NeuroImage* **48**, 63–72 (2009).

17. J. D. Power, *et al.*, Methods to detect, characterize, and remove motion artifact in resting state fMRI. *NeuroImage* **84**, 320–341 (2014).

18. Y. Behzadi, K. Restom, J. Liau, T. T. Liu, A component based noise correction method (CompCor) for BOLD and perfusion based fMRI. *NeuroImage* **37**, 90–101 (2007).

19. T. D. Satterthwaite, *et al.*, An improved framework for confound regression and filtering for control of motion artifact in the preprocessing of resting-state functional connectivity data. *NeuroImage* **64**, 240–256 (2013).

20. C. Lanczos, Evaluation of Noisy Data. *J. Soc. Ind. Appl. Math. Ser. B Numer. Anal.* **1**, 76–85 (1964).

Chapter 2: Accelerated epigenetic aging associates with whole-brain functional connectivity and impaired cognitive performance in older adults

Full author list: Andrew J. Graves, Joshua S. Danoff, Minah Kim, Samantha R. Brindley, Amalia M. Skyberg, Stephanie N. Giamberardino, Morgan E. Lynch, Brenda C. Straka, Travis S. Lillard, Simon G. Gregory, Jessica J. Connelly, James P. Morris

Submitted for peer review at Science Advances as of July 7th, 2023.

Introduction

The body and mind undergo significant changes as we age through the lifespan (*1*, *2*). These developmental trajectories are critical for healthy development, reducing risk of mortality, and overall well-being (*3*–*5*). While chronological age is a strong predictor for health-related risk factors, it is an incomplete metric that fails to fully characterize the unique aging process of individuals with different genetic makeup, neurodevelopment, and environmental experiences (*6*, *7*). One of the most striking changes humans undergo as we age is general decline across a wide variety of cognitive faculties, including memory, reasoning, spatial visualization, and processing speed (*8*). The current research is focused on taking an interdisciplinary approach for understanding cognitive aging through an epigenetic and neuroimaging framework.

Recent advances in epigenomic array technologies have made it possible to generate DNA methylation-based biomarkers of biological aging (*9*). These biomarkers, called epigenetic clocks, use DNA methylation values from CpG sites across the genome to estimate the biological age of a person or tissue. One major advantage of epigenetic clocks is that they can be measured from all sources of DNA, including peripheral tissues, and can be applied throughout the lifespan (*10*). The first epigenetic clock, Horvath's multi-tissue age estimator, yields epigenetic age estimates highly correlated with chronological age (*10*). Biological aging can be differentiated from chronological age by taking the residuals leftover from the linear relationship between epigenetic age and chronological age, which captures the information embedded in the biomarker unexplained by chronological age. A higher epigenetic age compared to an individual's chronological age would indicate they are aging faster than expected. This epigenetic age acceleration is associated with risk of mortality and various age-related diseases including cancer, cardiovascular diseases, and dementia (*11*). Additionally, it is possible to assess these biomarkers of aging prior to the onset of disease (*12*, *13*). After the publication of Horvath's original multi-tissue age estimator, many other epigenetic clocks have been developed that capture different aspects of aging and are sensitive to external environmental factors (*7*). The current research is utilizing DNAmGrimAge, an epigenetic clock that was developed to reflect physiological changes associated with aging, including known plasma protein biomarkers of aging (*14*). DNAmGrimAge age acceleration (denoted as AgeAccelGrim) stands out among epigenetic clocks in its capacity to predict mortality risk and clinically-relevant measures of aging (*14*, *15*).

Arguments have been made that general epigenetic processes are crucial for healthy cognitive aging (*16*). While most research has focused on medical and physical outcomes related to epigenetic age, several studies have investigated the link between epigenetic aging processes and cognition (*17–20*). One study found that age-adjusted Horvath's clock values negatively correlated with a single *g*-factor derived from cognitive items using principal components analysis in the Lothian Birth cohort (*21*). A similar finding was reported in another sample, and found that digit symbol substitution, symbol search 4-choice reaction time, and matrix reasoning survived inference criterion after mass-univariate hypothesis testing from a collection of cognitive items (*22*). A longitudinal twin-study found that twins with higher epigenetic age acceleration relative to their twin sibling experienced more cognitive decline, which directly points to a role of epigenetic modification in cognitive aging (*23*). However, a different twin-study using the original Horvath and Hannum methods did not find evidence for a link between epigenetic age acceleration and cognition (*24*).

A qualitative meta-analysis of the current literature, which includes a heterogenous collection of epigenetic clock and cognitive measurements, suggests that the link between epigenetic age acceleration and cognition is potentially promising but currently unclear and inconsistent (*25*). The pattern of results in the literature is heavily dependent upon the epigenetic clock chosen as well as the investigated cognitive domain, with modern epigenetic clocks typically outperforming first-generation epigenetic clocks for detecting associations (*26*). And while studies exist that have looked at structural brain changes such as BrainAge estimators, there is a dearth of research examining functional brain changes with functional magnetic resonance imaging (fMRI) for age accelerated individuals (*27*). This is important because differences in functional brain organization is a putative mechanism for explaining the potential link between epigenetic age and cognition (*28*).

With respect to individual differences in human brain activity, the aging process has been examined with resting-state functional connectivity (rsFC) in fMRI. Resting-state functional networks measure the temporal co-activation of low frequency blood-oxygen-level-dependent (BOLD) signals when individuals are "at rest" and have shown to be stable across timepoints (*29*, *30*). Studies on healthy adults have consistently documented aging-related decreases in long-range connectivity within the Default Mode Network (DMN), comprised of the medial prefrontal cortex, the posterior cingulate cortices, hippocampus and the inferior parietal lobules (*31–35*). These declines in connectivity were preserved after controlling for structural gray matter volume (*33*, *36*). In addition, aging has been associated with decreased connectivity in rsFC networks associated with attention, salience and/or motor regions (*36–38*) and increased connectivity in networks related to sensorimotor and subcortical structures (*38*).

Variability in rsFC has also been found to map onto individual differences in cognitive abilities (*39*, *40*). In aging individuals, increased connectivity in the DMN have been related to better scores on a memory task (*41*), a cognitive control task (*42*), a motor speed task (*43*), and an executive functioning and processing speed task (*33*). However increased connectivity has not always been shown to be linked with better cognitive

performance in this age group: Decreased interhemispheric coupling of language processing areas were found to be positively correlated with grammar learning (*44*) and decreased connectivity between the thalamus and basal ganglia were positively related with verbal episodic memory (*45*). Newer studies have cited interhemispheric connectivity and connectivity within the cingulo-opercular network as important neural correlates of cognitive skills in aging adults (*46, 47*). In summary, rsFC has utility in helping us understand age-related changes and variability in cognitive aging.

One particularly influential analysis approach for understanding individual differences in resting-state brain networks is the connectome-based predictive model (CPM) (*48*). CPM leverages robust idiosyncrasies of functional connectivity across individuals to make phenotypic predictions. CPM is particularly suited for individual differences research, as the networks are highly predictive of an individual's identity irrespective of nuisance artifacts such as head motion or anatomical differences (*49*). Successful analysis frameworks using CPM include predicting an individual's ID, age, attention, and general intelligence, among other phenotypes (*48, 50, 51*). Because epigenetic age acceleration and chronological age capture unique components of the aging process, it is currently unclear due to the dearth of research whether or not epigenetic age acceleration is related to individual differences in functional brain connectivity. To our knowledge, no research group has published work on using rsFC to examine changes in AgeAccelGrim.

The approach for the current research is unique because we are investigating an entire cognitive battery and decomposing those items into interpretable latent factors using a network model, and then using neuroimaging as a tool to understand how these relationships may be represented in the brain. This is in contrast to the previous studies investigating the relationship between epigenetic age and cognition, which have either 1) performed principal components analysis to estimate a single *g*-factor based on only one principal component, 2) only analyzed statistical relationships at the item-level which may be limited by the idiosyncratic properties of the task relevant to that item, and 3) importantly, did not use fMRI to build connectome-based predictive models to characterize these relationships in the brain. In other words, it is unclear which cognitive domains are consistently impacted by epigenetic age acceleration, and it is unknown if functional brain organization is an important mechanism for explaining these associations. We are also including measures of crystallized intelligence (e.g., vocabulary assessments), in order to disambiguate if the relationship between epigenetic age processes and cognition is driven solely by fluid intelligence constructs (i.e., processing speed, spatial reasoning, etc.) or not (*52*). This is an important distinction, given that crystallized intelligence typically does not decline with age and may not be as sensitive to the aging brain to the same degree as fluid intelligence, which will inform the scope of the effect of epigenetic processes on healthy cognition and brain function (*53*).

The first goal of the current research is to test whether epigenetic aging processes (as indexed by AgeAccelGrim) predict individual differences between people across multiple cognitive ability domains. Specifically, we hypothesize that individuals who are more age accelerated with respect to their epigenome will perform worse on a wide

variety of cognitive assessments that measure various facets of both fluid and crystallized intelligence. To answer this question, we used a subset of the Virginia Cognitive Aging Project (VCAP) cohort who provided samples for epigenetic analysis and underwent fMRI. VCAP is one of the world's largest longitudinal studies of cognitive change in normal aging, and has recently been enriched by data collection protocols incorporating epigenomic and neuroimaging data (*54*). This subset of VCAP participants includes individuals with scores showing signs of cognitive decline and individuals with scores showing signs of cognitive improvement (estimated by their previous visits). To index cognitive performance across a wide variety of domains, we used the VCAP cognitive battery, which includes 15 scales that map onto the latent domains of processing speed, memory, spatial visualization, reasoning, and vocabulary (three scales for each domain). This will help clarify whether or not second-generation epigenetic clocks, such as AgeAccelGrim, do in fact negatively impact cognition.

The second goal of the current research is to test whether AgeAccelGrim can be predicted from an individual's rsFC fMRI profile using ridge regression connectome-based predictive models (rCPM). We are specifically interested in whether or not individual differences in cognition account for the potential relationship between rsFC and AgeAccelGrim. If functional networks were identified as being predictive, we used graph-theoretic tools to estimate which brain regions are important for contributing to overall model performance. We hypothesize that functional connectivity of brain structures that can predict AgeAccelGrim are important functional hubs for higher-order cognitive abilities such as those measured by the VCAP cognitive battery. We aimed to determine whether the functional connectivity profiles are reflective of general cognitive abilities (i.e., *g*-factor), or a more specific process such as processing speed or memory. Answering these questions will enrich our understanding of if and how epigenetic age acceleration impacts functional brain network connectivity in the context of cognitive differences across individuals. Furthermore, finding evidence in functional brain networks may help explain why there is a link between epigenetic aging and cognitive aging processes.

Results

Four latent cognitive domains were estimated from the VCAP cognitive battery

Before further modeling, we reduced the dimensionality of the VCAP cognitive battery into latent components. The results from Bootstrap Exploratory Graph Analysis (bootEGA) suggest four distinct communities, which roughly map to the cognitive domains of processing speed, memory, reasoning/ spatial visualization, and vocabulary (see Fig. 1). These latent variable communities were stably estimated, such that items consistently loaded into the same factor across repeated iterations (for stability metrics, please see Fig. S1). The dimensionality assessment of four communities from bootEGA corroborates with the Scree plot in Fig. 1 using eigenvalue-eigenvector decomposition. The number of eigenvalues greater than 1 is a rough heuristic estimate of the number of distinct communities contained in a collection of variables (in this case, 4). The likely reason for the reasoning and spatial visualization factors to be collapsed into the same

community is the inclusion of the matrix reasoning item, which loads most strongly onto this latent variable and requires spatial abilities to solve appropriately. It is also common to find that reasoning and spatial visualization abilities are highly positively correlated with each other (*55*). It is important to note that the four derived latent factors are not orthogonal, and items from different communities can have non-zero weights onto other communities. This makes sense to allow from a cognitive perspective, as we do not expect any of these domains to be fully independent of each other.

Marginal correlations between AgeAccelGrim and all measured cognitive items are negative

In order to directly compare results from the item-level cognitive data to the latent-level cognitive data, we computed a simple Pearson's correlation matrix between all cognitive items, latent variables, AgeAccelGrim, and chronological age (see Fig. 2). Participant level summary statistics for cognitive performance and demographics are included in Table 1. For this analysis, we are not making any conclusions based on significance testing, but rather describing the pattern of marginal associations between all of these variables before fitting statistical models. For this specific analysis, data are aggregated over session by taking the mean cognitive score across sessions. There are several important pieces of information to glean from this analysis. First, by design, there is no linear relationship between AgeAccelGrim and chronological age; these two random variables are orthogonal with each other. Second, the sign of the marginal correlation between AgeAccelGrim and all cognitive items are negative. As expected, the same is true for chronological age. Third, the correlation between all cognitive items are positive, exhibiting the classical pattern of a positive manifold in cognitive testing (*56*). Fourth, the latent variables estimated from bootEGA (denoted as Proc. Speed, Memory, Spatial/ Reasoning, and Vocabulary) capture the unique contributions of the items that belong in their respective communities, by exhibiting larger positive correlations within-community relative to between-community. Finally, because the latent variables themselves exhibit a degree of positive correlation, this motivates the use of a multivariate statistical model to account for the linear relationships between the response variables.

AgeAccelGrim negatively associates with cognitive performance conditioning on chronological age and relevant covariates

Results from the multivariate hierarchical Bayesian model indicate that AgeAccelGrim does in fact negatively correlate with cognitive performance across all four empirically derived latent domains (see Fig. 3 and Table 2). This finding suggests that faster epigenetic age acceleration is associated with between-person differences in worse cognitive performance across tasks that measure both fluid and crystallized intelligence. Using the analogous Bayesian procedure for computing adjusted probability values directly from the posterior distributions, processing speed (p = .007), memory (p = .004), reasoning/ spatial visualization (p = .009), and vocabulary (p = .009) all survive our inference threshold of $\alpha = 0.05$ using the False Discovery Rate (FDR) procedure for multiple comparisons (see Fig. S2 for posterior fits) (*57*). This further corroborates with

the evidence from Fig. 2 that demonstrates the marginal correlation between AgeAccelGrim and every single cognitive survey administered has a negative sign. Results from the model provide further evidence for a direct relationship between AgeAccelGrim and cognitive performance by conditioning on chronological age, sex, time factors, and blood cell count indices. By design, AgeAccelGrim and chronological age are fully orthogonal to each other, which suggests that AgeAccelGrim explains a unique portion of the variance in the response variable not captured by chronological age, because both covariates are included in the model estimation. As expected, chronological age was also negatively related to all four cognitive domains. The standardized AgeAccelGrim β coefficient maximum a-posterior (MAP) estimates for all four cognitive variables fall between -0.25 and -0.35. This suggests that a one standard deviation increase in AgeAccelGrim results in approximately one-fourth / one-third of a standard deviation decrease across all measured cognitive faculties.

Both AgeAccelGrim and Age can be predicted from functional connectomes, and these results are accounted for via individual differences in cognition

Using rCPM, we are able to significantly predict AgeAccelGrim (median Spearman's r = .313, non-parametric p = .021) and chronological age (median Spearman's r = .364, non-parametric p = .012) from resting-state functional connectivity. Fig. 4 shows the distributions of model performance, and suggests that controlling for cognition mitigates the ability to predict AgeAccelGrim and age, suggesting that functional connectivity in the brain is a potential mediating mechanism that explains the relationship between AgeAccelGrim and cognition. In particular, it seems to be the case that memory (median Spearman's r = .391, non-parametric p = .005) and spatial visualization/ reasoning (median Spearman's r = .316, non-parametric p = .012) are able to be predicted from functional connectomes and share the most information with epigenetic age and chronological age-functional connectivity associations. In contrast, processing speed (median Spearman's r = .194, non-parametric p = .101) and vocabulary abilities (median Spearman's r = .138, non-parametric p = .183) were not able to be predicted from resting-state functional connectomes. Fig. S3 shows example representations computed when fitting rCPM models, which are highly correlated with simple bivariate correlations between pairwise connectivity and AgeAccelGrim, and suggest interpretability of the resulting coefficients.

The most important brain regions within the connectome for predicting AgeAccelGrim and Age support memory processes

Using eigenvector centrality to estimate which brain regions are important within the rCPM model, we found that the top five brain regions used to predict AgeAccelGrim and memory are similar, and that these structures largely support memory processes. Table 3 shows the most important brain regions in terms of functional connectivity that support a healthy aging process indexed by less epigenetic age acceleration and better memory performance. These brain regions include medial temporal lobe structures such as the hippocampus, parahippocampal cortex, anterior temporal lobe, orbitofrontal cortex, and retrosplenial cortex. Table 4 shows the most important brain regions that indicate a

more at-risk aging process indexed by more epigenetic age acceleration and worse memory performance. Interestingly, this model returned some similar nearby patches of subcortex including hippocampal regions within the medial temporal lobe, as well as the caudate nucleus and amygdala. Because of the similarity of results across both the positive and negative weight models, particularly for the medial temporal lobes, it appears that more functional connectivity in some medial temporal lobe structures is indicative of healthy aging while in others less functional connectivity. Fig. 5 and Fig. 6 show that networks for more epigenetic age acceleration and worse memory (and vice versa) have similar structure, as indexed by opposing color patterns particularly in the limbic system, but also in cerebellum, brainstem, and subcortical connections to proximal lobes. Fig. S4 shows that this structure is specific to AgeAccelGrim, by demonstrating that chronological age does not show the same opposing color pattern in the Hinton diagrams with respect to the memory networks. Table S1 includes the most important regions for predicting older age and younger age, which also include hippocampus, parahippocampus, and orbitofrontal cortex, as well as the caudate. Importantly, the important brain regions detected with AgeAccelGrim and age are different nodes in the network, thus adding unique information and complementary information when considered together.

Discussion

This research provides evidence that epigenetic age acceleration relates to between-person differences in cognitive abilities of both fluid and crystallized intelligence, and that functional connectivity profiles that predict AgeAccelGrim are similar to functional connectivity profiles that predict memory abilities. Specifically, individuals with more epigenetic age acceleration tended to perform worse on tasks that spanned a wide variety of cognitive faculties, and brain regions crucial for successful memory formation were most important for predicting AgeAccelGrim in the aging brain. These differences cannot be explained by chronological age alone, in that AgeAccelGrim and chronological age are orthogonal variables, and both were included/ controlled for in each statistical model. This suggests that epigenetic age explains a unique portion of variance of cognitive ability that chronological age does not capture, and this relationship may be explained by connectivity of memory brain structures primarily within the limbic system. Furthermore, at the behavioral level the effect of epigenetic age on cognition seems to negatively impact multiple domains and is not limited to fluid intelligence metrics. Interestingly the estimated slope values for AgeAccelGrim and chronological age were relatively close in standardized value across the domains, which may suggest that both factors are similarly important for predicting cognitive performance.

In terms of the brain, however, this relationship does seem to be specific to memory and/or spatial visualization and reasoning processes in this cohort. This was reflected in the brain systems identified as important using rCPM, which largely implicated sub-cortical structures in the medial temporal lobe and limbic system. Connectivity within these nearby structures has been previously shown to change through aging and relates to cognitive outcomes (*58–60*). Furthermore, the direction of connectivity (positive vs. negative) depends on the exact structures measured in these

systems, such as the head, tail, or body of the hippocampus (*61*). Model systems work corroborates with human studies, such that differential connectivity in CA1 and CA3 regions of the hippocampus in rats undergoing resting-state fMRI is associated with age-related memory deficits (*62*). Taken together, these brain structures are known to be important for aging and cognitive change, and here we demonstrate that epigenetic age acceleration captures a unique portion of this functional brain organization as it pertains to these differences.

There are several limitations to the current research. Ideally, epigenetic age indices are tracked longitudinally in temporal synchrony with cognitive measurements and fMRI to assess within-person dynamics of these three factors through time. Access to this data could facilitate answering the question if epigenetic age acceleration precedes or follows cognitive decline within an individual as they age. While this would not be a fully causal explanation, it would provide insight into understanding which of these factors is first impacted by the aging process. We hypothesize that epigenetic age acceleration does in fact precede deficits in cognitive performance and differential functional connectivity, but more studies would need to be designed to provide evidence for an answer to that question. Another limitation of this study is the participant sample, which consists of relatively healthy older adults. Estimating the average association between epigenetic age acceleration, cognition, and functional brain connectivity would require sampling from across the lifespan as well as across the entire spectrum of general health. It is difficult to say if the relationship between epigenetic age acceleration, cognition, and functional brain connectivity would be heightened or diminished if a sample fully representative of the population were assessed.

The VCAP cohort is in a unique position to contribute to our understanding of when and how pathological aging diverges from normal cognitive aging. This could manifest as Mild Cognitive Impairment (MCI) or more severe cases such as Alzheimer's disease and Alzheimer's disease related dementias (AD/ADRD). A future goal is to be able to estimate the likelihood of healthy and pathological development using epigenetic age, so that we can build better systems for predictive diagnostics and early intervention for specific persons. This could be accomplished through a rich and interdisciplinary individual differences approach to studying cognitive aging, by tracking epigenomic, phenotypic, and neuroimaging data together through time longitudinally. While further research is necessary for direct applications of these findings, epigenetic age acceleration together with neuroimaging in the future could be used as an important factor to consider for assessing risk of cognitive decline for individuals. The current research provides evidence that this could be a promising future approach for prospectively predicting cognitive decline risk, as the collection of epigenetic age and brain data becomes less expensive, and the quantification of this specific risk is analyzed with a sample representative of the general population. In summary, this research provides further evidence for the important role of epigenetic aging processes on the development and maintenance of healthy cognitive capacities, and suggests that functional connectivity within relevant brain structures for these capacities is differentially modulated through epigenetic age.

Materials and Methods

Experimental Design

The VCAP cognitive battery was measured longitudinally, across short and long time-scales using a variable retest interval and measurement burst design. For each occasion, participants' cognitive abilities were surveyed three times in two-hour sessions, with each session being separated by two weeks. For the current research, we are only examining the occasion (three sessions per participant, $N = 103$) that is closest in time to the provided epigenetic sample. Only 98 out of the 103 participants underwent fMRI, thus the neuroimaging analysis and results are based on the 98 participants who completed our fMRI protocol, while the behavioral results include all 103 participants.

Cognitive Measurements

Each cognitive scale name has an associated abbreviation in parentheses for its name which is used in all figures and tables in order to conserve space. Descriptions of these tasks were abbreviated from descriptions previously published (*8*). Sum scores of each cognitive task were computed as the basis for the bootEGA model.

Processing Speed

The three instruments used to assess processing speed were Digit Symbol Substitution (DigSym), Pattern Comparison (PatCom), and Letter Comparison (LetCom). DigSym involves referencing a code table to write symbols arbitrarily paired with digits as quickly as possible (*63*). PatCom involves determining if two line patterns are the same or different as quickly as possible (*64*). LetCom involves determining if two letter strings are the same or different as quickly as possible (*65*).

Memory

The three instruments used to assess memory were Word Recall (Recall), Logical Memory (LogMem), and Paired Associates (PAssoc). Recall requires listening to a list of 12 unrelated words and then immediately recalling as many as possible (*66*). LogMem requires listening to a story and then immediately recalling as many details of that story as possible (*66*). PAssoc requires listening to six pairs of unrelated words, and then recalling the second member of the pair after being cued by the first member (*67*).

Spatial Visualization

The three instruments used to assess spatial visualization were Spatial Relations (SpaRel), Paper Folding (PapFld), and Form Boards (FrmBrd). SpaRel involves identifying which three-dimensional figures corresponds to which two-dimensional figure if it were assembled (*68*). PapFld involves selecting the pattern of holes that would result if a piece of paper were to be folded and a hole were punched in the specified location

(*69*). FrmBrd involves selecting pieces that could be constructed to fill a designated form (*69*).

Reasoning

The three instruments used to assess reasoning were Matrix Reasoning (MatRea), Shipley Abstraction (Ship), and Letter Sets (LetSet). MatRea requires choosing a solution from alternatives to complete the missing cell in a matrix of geometric patterns (*70*). Ship requires determining the best option for completing a pattern from a series of elements (*71*). LetSet requires identifying the outlier among sets of letters that does not follow the same pattern/ rule as the others (*69*).

Vocabulary

The three instruments used to assess vocabulary were WAIS Vocabulary (Vocab), Synonym Vocabulary (SynVoc), and Antonym Vocabulary (AntVoc). Vocab asks participants to provide a definition for each word where scores are either incorrect, incomplete, partially correct, or correct (*63*). SynVoc asks participants to identify which of five words is the synonym to the target word (*72*). AntVoc asks participants to identify which of five words is the antonym to the target word (*72*).

Epigenetic Age

Eight and a half milliliters of whole blood were drawn into a PAXgene Blood DNA Tube (PreAnalytiX, Hombrechtikon, Switzerland). Samples were stored at 20°C for short-term storage (up to 3 months) then transferred to -80°C for long-term storage. DNA was extracted using the PAXgene Blood DNA kit (PreAnalytiX, Hombrechtikon, Switzerland) according to manufacturer instructions. DNA concentration was determined by Quant-iT™ PicoGreen® dsDNA reagent (Thermofisher Scientific, Waltham, MA, USA) per manufacturers instruction. Florescence was detected using a Tecan Infinite M200 Pro microplate reader (Tecan, Switzerland). 500 ng of DNA was bisulfite treated using a Zymo EZ DNA Methylation kit (Zymo Research, Irvine, CA) using PCR conditions for Illumina's Infinium Methylation assay (95°C for 30 seconds, 50°C for 60 minutes×16 cycles). DNA methylation was assayed using the Illumina Infinium MethylationEPIC BeadChips. Briefly, a total of 4μL of bisulfite converted DNA was hybridized to Illumina BeadChips using the manufacturer's protocols. Samples were denatured and amplified overnight for 20 to 24 hours. Fragmentation, precipitation, and resuspension of the samples followed overnight incubation, before hybridization to EPIC BeadChips for 16 to 24 hours. BeadChips were then washed to remove any unhybridized DNA and labeled with nucleotides to extend the primers to the DNA sample. Following the Infinium HD Methylation protocol, the BeadChips were imaged using the Illumina iScan system (Illumina).

Raw .idat files were read and preprocessed using the *minfi* package in R (*73*, *74*). The data set was preprocessed using noob for background subtraction and dye-bias normalization. All methylation values with detection $P > 0.01$ were set to missing

(median sample: 765 probes, range: 319 to 4453), and probes with >1% missing values (n = 6,663) were removed from further analysis. All samples were checked and confirmed to ensure that predicted sex matched reported sex. Additionally, samples were checked for excessive missing data (>5%) and unusual cell mixture estimates, which was estimated using the Houseman method as implemented in *minfi* (*75*, *76*). All samples passed these quality controls. Principal components analysis, as implemented in the *shinyMethyl* package in R, was used to examine batch effects (*77*). The first seven principal components were examined using plots and potential batch effects were tested using linear models. Principal components 3 and 6, which accounted for 2.38% and 1.65% of total variance respectively, were associated with position on the array (PC3: $F_{(7, 100)}$ = 6.668, p = 1.77e-6, adjusted R^2 = 0.271; PC6: $F_{(7, 100)}$ = 2.328, p = 0.030, adjusted R^2 = 0.080). Principal components 1, 4, and 5, which accounted for 3.63%, 1.89%, and 1.77% of the total variance were associated with bisulfite conversion plate (PC1: $F_{(1, 106)}$ = 9.918, p = 0.002, adjusted R^2 = 0.077; PC4: $F_{(1, 100)}$ = 34.04, p = 5.932e-8, adjusted R^2 = 0.236; PC5: $F_{(1, 100)}$ = 31.07, p = 1.91e-7, adjusted R^2 = 0.219). Principal components 4 and 5 were associated with array (PC4: $F_{(13, 94)}$ = 4.332, p = 1.14e-5, adjusted R^2 = 0.288; PC5: $F_{(13, 94)}$ = 4.229, p = 1.06e-5, adjusted R^2 = 0.282). Bisulfite conversion plate and array number were associated with each other, as samples on the same array originated from the same bisulfite conversion plate. Because samples were randomized across plates and arrays, and proportions of variance explained by associated principal components were low, no batch correction method was used. The *ewastools* package in R was used to assess Illumina quality control metrics and call genotypes and donor IDs to ensure the identity of repeated samples from the same individual (*78*). All samples passed Illumina quality controls.

To determine assay variability, we included one set of five technical replicates and an additional three sets of two technical replicates. After quality control filters and normalization procedures were applied, the 5,000 CpGs with the most variable M values were used as input for calculating Pearson's correlation coefficients among all pairwise combinations of samples. Pearson's correlation of unrelated samples (different individuals) were below 0.8, while correlations of technical replicates ranged from 0.988-0.994, indicating high agreement between technical replicates.

Unnormalized betas were filtered to include CpGs specified by Horvath as necessary for calculation of various clocks. The betas were uploaded to Horvath's online DNA methylation age calculator (htpps://dnamage.genetics.ucla.edu), which provides measures of Horvath's multi-tissue age estimator, DNA methylation GrimAge, and cell type abundance (*10*, *79*). A sample annotation file was included. The options to normalize data and apply advanced analysis were selected. Technical replicates were used to determine measurement error of DNAmAge, the output of Horvath's multi-tissue age estimator. The absolute difference of DNAmAge between technical replicate pairs was taken, as was the highest absolute difference in the set of five technical replicates. The median of the absolute difference was 2.02 years (range: 0.44-5.73 years), comparable to previous reports of measurement error being approximately 2.41 years (*80*).

Functional Magnetic Resonance Imaging

Imaging Parameters and Acquisition

MRI scanning was performed at the University of Virginia Fontaine Research Park on a Siemens 3 Tesla MAGNETOM Prisma Fit high-speed imaging device equipped with a 32-channel head-coil. First, high-resolution T1-weighted anatomical images were acquired using Siemens' magnetization-prepared rapid-acquired gradient echo (MPRAGE) pulse sequence with the following specifications: echo time (TE) = 2.98 ms; repetition time (TR) = 2300 ms; flip angle (FA) = 9°; image matrix = 240 mm × 256 mm; slice thickness = 1 mm; 208 slices. Then, whole-brain functional images were acquired using a T2*-weighted echo planar imaging (EPI) sequence sensitive to BOLD contrast with the following specifications: TE = 30 ms; TR = 800 ms; FA = 52°; image matrix = 90 mm x 90 mm; slice thickness = 2.4 mm; slice gap = 2.4 mm; 660 slices. We collected two 610 volume resting-state functional runs, totaling 976 seconds of resting-state functional imaging data for each participant. A black crosshair on a gray background was presented using an LCD AVOTEC projector onto a screen located behind the participant's head and viewed through an integrated head-coil mirror.

Pre-processing with *fMRIPrep*

Results included in this chapter come from preprocessing performed using *fMRIPrep* 21.0.2 (RRID:SCR_016216) (*81*), which is based on *Nipype* 1.6.1 (RRID:SCR_002502) (*82*). Many internal operations of *fMRIPrep* use *Nilearn* 0.8.1 (*83*), mostly within the functional processing workflow. For more details of the pipeline, see the section corresponding to workflows in *fMRIPrep*'s documentation. For each participant, the T1-weighted (T1w) image was corrected for intensity non-uniformity (INU) with N4BiasFieldCorrection (*84*), distributed with ANTs 2.3.3 (RRID:SCR_004757) (*85*), and used as T1w-reference throughout the workflow. The T1w-reference was then skull-stripped with a *Nipype* implementation of the antsBrainExtraction.sh workflow (from ANTs), using OASIS30ANTs as target template. Brain tissue segmentation of cerebrospinal fluid (CSF), white-matter (WM) and gray-matter (GM) was performed on the brain-extracted T1w using fast (FSL 6.0.5.1:57b01774, RRID:SCR_002823) (*86*). Volume-based spatial normalization to one standard space (MNI152NLin2009cAsym) was performed through nonlinear registration with antsRegistration (ANTs 2.3.3), using brain-extracted versions of both T1w reference and the T1w template. The following template was selected for spatial normalization: *ICBM 152 Nonlinear Asymmetrical template version 2009c* (RRID:SCR_008796; TemplateFlow ID: MNI152NLin2009cAsym) (*87*). A deformation field to correct for susceptibility distortions was estimated based on *fMRIPrep*'s *fieldmap-less* approach. The deformation field is that resulting from co-registering the EPI reference to the same-subject T1w-reference with its intensity inverted (*88*, *89*). Registration is performed with antsRegistration (ANTs 2.3.3), and the process regularized by constraining deformation to be nonzero only along the phase-encoding direction, and modulated with an average fieldmap template (*90*).

For each of the two BOLD resting-state runs per subject, the following preprocessing was performed. First, a reference volume and its skull-stripped version were generated using a custom methodology of *fMRIPrep*. Head-motion parameters with respect to the BOLD reference (transformation matrices, and six corresponding rotation and translation parameters) were estimated before any spatiotemporal filtering using mcflirt (FSL 6.0.5.1:57b01774) (*91*). The estimated *fieldmap* was then aligned with rigid-registration to the target EPI (echo-planar imaging) reference run. The field coefficients were mapped on to the reference EPI using the transform. BOLD runs were slice-time corrected to 0.351s (0.5 of slice acquisition range 0s-0.703s) using 3dTshift from AFNI (RRID:SCR_005927) (*92*). The BOLD reference was then co-registered to the T1w reference using mri_coreg (FreeSurfer) followed by flirt (FSL 6.0.5.1:57b01774) (*93*) with the boundary-based registration cost-function (*94*). Co-registration was configured with six degrees of freedom.

Several confounding time-series were calculated based on the *preprocessed BOLD*: framewise displacement (FD), DVARS and three region-wise global signals. FD was computed using two formulations following Power (absolute sum of relative motions (*95*)) and Jenkinson (relative root mean square displacement between affines (*91*)). FD and DVARS were calculated for each functional run, both using their implementations in *Nipype* (*95*). The three global signals were extracted within the CSF, the WM, and the whole-brain masks. Additionally, a set of physiological regressors were extracted to allow for component-based noise correction (*CompCor*) (*96*). Principal components were estimated after high-pass filtering the *preprocessed BOLD* time-series (using a discrete cosine filter with 128s cut-off) for the two *CompCor* variants: temporal (tCompCor) and anatomical (aCompCor). tCompCor components were then calculated from the top 2% variable voxels within the brain mask. For aCompCor, three probabilistic masks (CSF, WM and combined CSF+WM) were generated in anatomical space. The implementation differs (*96*) in that instead of eroding the masks by 2 pixels on BOLD space, the aCompCor masks are subtracted a mask of pixels that likely contain a volume fraction of GM. This mask is obtained by thresholding the corresponding partial volume map at 0.05, and it ensures components are not extracted from voxels containing a minimal fraction of GM. Finally, these masks are resampled into BOLD space and binarized by thresholding at 0.99 (as in the original implementation). Components are also calculated separately within the WM and CSF masks. For each CompCor decomposition, the *k* components with the largest singular values are retained, such that the retained components' time series are sufficient to explain 50 percent of variance across the nuisance mask (CSF, WM, combined, or temporal). The remaining components are dropped from consideration. The head-motion estimates calculated in the correction step were also placed within the corresponding confounds file. The confound time series derived from head motion estimates and global signals were expanded with the inclusion of temporal derivatives and quadratic terms for each (*97*). Frames that exceeded a threshold of 0.5 mm FD or 1.5 standardized DVARS were annotated as motion outliers.

The BOLD time-series were resampled into standard space, generating a *preprocessed BOLD run in MNI152NLin2009cAsym space*. All resamplings can be performed with *a single interpolation step* by composing all the pertinent transformations

(i.e., head-motion transform matrices, susceptibility distortion correction when available, and co-registrations to anatomical and output spaces). Gridded (volumetric) resamplings were performed using antsApplyTransforms (ANTs), configured with Lanczos interpolation to minimize the smoothing effects of other kernels (*98*).

Parcellation and Image Preparation

At the parcellation step, functional images were high-pass filtered at .008 Hz and cleaned with the following fMRIPrep confound derivatives to account for global BOLD signal outside of gray matter (csf, white_matter), primary data-driven estimated noise components (tcompcor, a_comp_cor_00, a_comp_cor_01) and motion-related parameters (trans_x, trans_x_power2, trans_y, trans_y_power2, trans_z, trans_z_power2, rot_x, rot_x_power2, rot_y, rot_y_power2, rot_z, rot_z_power2). For both resting-state functional scans, parcellation was performed by taking the framewise average of the voxel-wise signals in each of the 268 nodes from the Shen atlas (*99*). The Shen atlas is a functionally defined parcellation that covers the whole brain, including cortex, subcortex, and cerebellum. The two resting-state scans were concatenated along the time dimension before calculating connectivity, as this can improve reliability of estimates (*100*). We calculated Fisher Z transformed Pearson correlation coefficients between the activity time courses of all possible pairs of nodes to construct 268 x 268 symmetric functional connectivity matrices. Only the lower triangle of each functional connectivity matrix was extracted and vectorized, discarding the constant diagonal, resulting in 35778 unique connections/ edges, which served as input features (i.e., columns in the design matrix) to rCPM.

Statistical Analysis

Bootstrap Exploratory Graph Analysis

In order to reduce the dimensionality of the cognitive measurements into a latent space, we applied bootEGA using the *EGAnet* package in R (*101*). bootEGA is a community detection and network analysis method to evaluate the dimensional structure estimated using Exploratory Graph Analysis (EGA) (*102, 103*). The general approach of bootEGA is to generate bootstrap samples and apply EGA to each replicate sample, forming a sampling distribution of EGA results. EGA models a collection of variables through estimation of a sparse regularized partial correlation matrix using the graphical LASSO (GLASSO) procedure (*104*).

The parametric bootstrap procedure begins by estimating a network using EGA and then generating new replicate data from a multivariate normal distribution (with the same number of cases as the original data). EGA is then applied to the replicate data, continuing iteratively until the desired number of samples is achieved (1000 iterations used). The result is a sampling distribution of EGA networks. From this sampling distribution, a median (or typical) network structure was estimated by computing the median value of each edge across the replicate networks, resulting in a single network. Such a network represents the “typical” network structure of the sampling distribution.

The Louvain community detection algorithm was then applied, resulting in dimensions that would be expected for a typical network from the EGA sampling distribution (identical community membership estimated by the Walktrap algorithm for comparison) (*105*). One metric for structural consistency is *item stability* or the robustness of each item's placement within each empirically derived dimension. Item stability is estimated by computing the proportion of times each item is placed in each dimension. This metric provides information about which items are leading to structural consistency (replicating often in their empirically derived dimension) or inconsistency (replicating often in other dimensions).

We computed standardized network community scores for each community from the model-implied graph from EGA. The standardized network community scores are linear combinations of the original measurements within the cognitive battery. These network scores are compressed representations of the original data and are analogous to component vectors from principal components analysis or factor scores from factor analysis (*106*). Each cognitive dimension derived from EGA (four, in this case) has its own network score vector. This means each participant has four network scores for each session, and each network score is computed as a linear combination of the weighted items that load onto each community.

Hierarchical Bayesian Model Approach

In order to model cognitive performance as a function of AgeAccelGrim, chronological age, sex, and blood cell count covariates (abbreviated as NK, Mono, Gran, PlasmaBlast, CD8pCD28nCD45Ran, CD8.naive, CD4.naive), we fit a multivariate hierarchical Bayesian generalized linear model with a Student-T likelihood. Because blood cell counts are known to influence DNAmGrimAge, we account for these age-related changes in immune cell populations to ensure the epigenetic age acceleration parameters are not merely indicative of blood cell counts (*107*). We used the Student-T likelihood as an alternative to the traditional Gaussian likelihood, because the Student-T alternative is more robust to outliers and converges to the Gaussian solution when Gaussian assumptions are in fact met (*108*). Interpreting the coefficients of Student-T regression (also known as robust regression in a Bayesian framework) is similar to traditional regression with a Gaussian likelihood. Each latent cognitive domain response variable was jointly estimated in a multivariate model to account for correlation across each domain.

We used the *brms* software package in R and the state-of-the-art Hamiltonian Monte-Carlo No-U-Turn sampler (NUTS) for Bayesian computation and inference (*109, 110*). Default priors on the intercepts were generated by Student-T($\nu = 3$, $\mu = 0.2$, $\sigma = 2.5$), and the σ scale parameters were generated by Student-T($\nu = 3$, $\mu = 0$, $\sigma = 2.5$). Priors for the ν degrees of freedom parameter were generated by $\gamma(\alpha = 2, \beta = 0.1)$, with special treatment of the vocabulary prior $\gamma(\alpha = 12, \beta = 0.1)$, due to its consistent underestimation of ν which would lead to unstable posteriors without being addressed. Priors for the correlation matrices between fixed and random effects were generated by LKJ-Cholesky($\eta = 1$). We ran 7 independent Markov chains each with 20,000 total

iterations, including 10,000 warm-up iterations. We fixed the target average proposal acceptance probability to 99% to improve the quality of sampling and thus the resulting posterior distributions. Convergence of the posteriors were confirmed with all $\hat{R} \approx 1.0$, which assesses agreement across the Markov chains. Posterior predictive checks were used to assess model adequacy (*111*).

Posterior distributions on the parameters can be inspected and inference can be employed using credible intervals (the Bayesian alternative to Frequentist confidence intervals). Additionally, we can simply look at the ratio of posterior density on respective sides of 0. Counting the number of observations in the sampled posterior distribution for a given parameter on the side of 0 that has the minority, and then multiplying that count by 2, results in a Bayesian analogue to a two-tailed Frequentist *p*-value. The *hypothesis* function in *brms* returns these posterior probabilities for inference (*112*). This procedure is not directly sensitive to the prior relative to alternative procedures such as bayes factors, making it a more attractive option when the priors are used simply for regularization and are not informed by domain knowledge (*113*).

There are several motivating factors for using Bayesian techniques for the current research. First, we can apply regularization priors to the regression coefficients as a way to employ shrinkage and mitigate potential for over-fitting, generated by $\beta \sim N(\mu = 0, \sigma = 10)$. Second, we can easily model hierarchy through probability distributions which allows for accurate estimation of subject-specific parameters, which we used to estimate intercepts and slopes through session to account for potential practice-effect noise. Third, we have explicit control over the probability distribution of the likelihood. This allows us to use more robust techniques such as Student-T regression. Overall, these three factors generally lead to more conservative and robust inference relative to the Frequentist approach (*114*). Last, we can fit this hierarchical model in a multivariate context, which typically requires Bayesian sampling-based approaches rather than optimization-based techniques given there is scarce software support or implementation applying this specific Frequentist optimization problem.

Ridge Regression Connectome-based Predictive Modeling

It has been shown that treating connectivity vectors as columns for predicting behavior using ridge regression tends to perform better than other popular connectome-based modeling approaches (*115*). Ridge regression is a linear supervised learning technique that regularizes model coefficients toward 0 with the canonical L2 norm. The regularization degree is governed by a single parameter, λ, where large values perform more shrinkage and small values perform less shrinkage. We performed rCPM using a repeated ($N = 100$) outer K-fold ($K = 10$) cross-validation procedure where individuals were split into 10 folds, models were trained using 9 of the folds, and then evaluated on the held-out fold. Within each cross-validation split, we tuned λ with an inner 2-fold cross-validation loop to conservatively estimate optimal regularization strength and overall prediction fit. The phenotypic outcomes were residualized with respect to confound/ nuisance variables specific for each analysis.

Prediction performance for the rCPM models were evaluated using the Spearman correlation, since successful rank prediction across participants was considered most important. To assess the statistical significance of prediction performance, we generated null distributions of expected performance metrics due to chance by permuting behavioral scores with respect to individuals and ran the rCPM pipeline for 1000 iterations. Then, we calculated a non-parametric *p*-value, which tallies the number of times the performance metric for each of the 1000 iterations of the null distribution exceeds the median performance metric of the 100 true iterations. The coefficient matrices were treated as networks to estimate importance of specific brain regions by calculating eigenvector centrality on the ridge regression coefficient matrix averaged across cross-validation iterations and separated by positive and negative sign. The top 2% of coefficients for both the positive and negative sign were used for the network visualizations.

References

1. J. Campisi, P. Kapahi, G. J. Lithgow, S. Melov, J. C. Newman, E. Verdin, From discoveries in ageing research to therapeutics for healthy ageing. *Nature*. **571**, 183–192 (2019).

2. C. López-Otín, M. A. Blasco, L. Partridge, M. Serrano, G. Kroemer, The hallmarks of aging. *Cell*. **153**, 1194–1217 (2013).

3. J. A. Sumner, N. L. Colich, M. Uddin, D. Armstrong, K. A. McLaughlin, Early Experiences of Threat, but Not Deprivation, Are Associated With Accelerated Biological Aging in Children and Adolescents. *Biological Psychiatry*. **85** (2019), doi:10.1016/j.biopsych.2018.09.008.

4. A. T. Lu, A. Quach, J. G. Wilson, A. P. Reiner, A. Aviv, K. Raj, L. Hou, A. A. Baccarelli, Y. Li, J. D. Stewart, E. A. Whitsel, T. L. Assimes, L. Ferrucci, S. Horvath, DNA methylation GrimAge strongly predicts lifespan and healthspan. *Aging*. **11** (2019), doi:10.18632/aging.101684.

5. G. E. Miller, E. Chen, K. J. Parker, Psychological Stress in Childhood and Susceptibility to the Chronic Diseases of Aging: Moving Toward a Model of Behavioral and Biological Mechanisms. *Psychological Bulletin*. **137** (2011), doi:10.1037/a0024768.

6. L. Ferrucci, M. Gonzalez-Freire, E. Fabbri, E. Simonsick, T. Tanaka, Z. Moore, S. Salimi, F. Sierra, R. de Cabo, Measuring biological aging in humans: A quest. *Aging cell*. **19**, e13080 (2020).

7. H. Palma-Gudiel, L. Fañanás, S. Horvath, A. S. Zannas, "Psychosocial stress and epigenetic aging" in *International Review of Neurobiology* (2020), vol. 150.

8. T. A. Salthouse, When does age-related cognitive decline begin? *Neurobiology of aging*. **30**, 507–514 (2009).

9. S. Horvath, K. Raj, DNA methylation-based biomarkers and the epigenetic clock theory of ageing. *Nature Reviews Genetics*. **19**, 371–384 (2018).

10. S. Horvath, DNA methylation age of human tissues and cell types. *Genome Biology*. **14** (2013), doi:10.1186/gb-2013-14-10-r115.

11. P. D. Fransquet, J. Wrigglesworth, R. L. Woods, M. E. Ernst, J. Ryan, The epigenetic clock as a predictor of disease and mortality risk: a systematic review and meta-analysis. *Clinical epigenetics*. **11**, 1–17 (2019).

12. R. E. Marioni, S. Shah, A. F. McRae, B. H. Chen, E. Colicino, S. E. Harris, J. Gibson, A. K. Henders, P. Redmond, S. R. Cox, A. Pattie, J. Corley, L. Murphy, N. G. Martin, G. W. Montgomery, A. P. Feinberg, M. D. Fallin, M. L. Multhaup, A. E. Jaffe, R. Joehanes, J. Schwartz, A. C. Just, K. L. Lunetta, J. M. Murabito, J. M.

Starr, S. Horvath, A. A. Baccarelli, D. Levy, P. M. Visscher, N. R. Wray, I. J. Deary, DNA methylation age of blood predicts all-cause mortality in later life. *Genome Biology*. **16** (2015), doi:10.1186/s13059-015-0584-6.

13. L. Perna, Y. Zhang, U. Mons, B. Holleczek, K. U. Saum, H. Brenner, Epigenetic age acceleration predicts cancer, cardiovascular, and all-cause mortality in a German case cohort. *Clinical Epigenetics*. **8** (2016), doi:10.1186/s13148-016-0228-z.

14. A. T. Lu, A. Quach, J. G. Wilson, A. P. Reiner, A. Aviv, K. Raj, L. Hou, A. A. Baccarelli, Y. Li, J. D. Stewart, E. A. Whitsel, T. L. Assimes, L. Ferrucci, S. Horvath, DNA methylation GrimAge strongly predicts lifespan and healthspan. *Aging*. **11** (2019), doi:10.18632/aging.101684.

15. C. McCrory, G. Fiorito, B. Hernandez, S. Polidoro, A. M. O'Halloran, A. Hever, C. Ni Cheallaigh, A. T. Lu, S. Horvath, P. Vineis, R. A. Kenny, GrimAge Outperforms Other Epigenetic Clocks in the Prediction of Age-Related Clinical Phenotypes and All-Cause Mortality. *Journals of Gerontology - Series A Biological Sciences and Medical Sciences*. **76** (2021), doi:10.1093/gerona/glaa286.

16. S. Akbarian, M. S. Beeri, V. Haroutunian, Epigenetic determinants of healthy and diseased brain aging and cognition. *JAMA neurology*. **70**, 711–718 (2013).

17. S. Shiau, S. M. Arpadi, Y. Shen, A. Cantos, C. V. Ramon, J. Shah, G. Jang, J. J. Manly, A. M. Brickman, A. A. Baccarelli, Epigenetic aging biomarkers associated with cognitive impairment in older African American adults with human immunodeficiency virus (HIV). *Clinical Infectious Diseases*. **73**, 1982–1991 (2021).

18. S. Degerman, M. Josefsson, A. N. Adolfsson, S. Wennstedt, M. Landfors, Z. Haider, S. Pudas, M. Hultdin, L. Nyberg, R. Adolfsson, Maintained memory in aging is associated with young epigenetic age. *Neurobiology of aging*. **55**, 167–171 (2017).

19. J. Bressler, R. E. Marioni, R. M. Walker, R. Xia, R. F. Gottesman, B. G. Windham, M. L. Grove, W. Guan, J. S. Pankow, K. L. Evans, Epigenetic age acceleration and cognitive function in African American adults in midlife: the atherosclerosis risk in communities study. *The Journals of Gerontology: Series A*. **75**, 473–480 (2020).

20. M. A. Beydoun, D. Shaked, S. M. Tajuddin, J. Weiss, M. K. Evans, A. B. Zonderman, Accelerated epigenetic age and cognitive decline among urban-dwelling adults. *Neurology*. **94**, e613–e625 (2020).

21. R. E. Marioni, S. Shah, A. F. McRae, S. J. Ritchie, G. Muniz-Terrera, S. E. Harris, J. Gibson, P. Redmond, S. R. Cox, A. Pattie, J. Corley, A. Taylor, L. Murphy, J. M. Starr, S. Horvath, P. M. Visscher, N. R. Wray, I. J. Deary, The epigenetic clock is correlated with physical and cognitive fitness in the Lothian Birth Cohort 1936. *International Journal of Epidemiology*. **44** (2015), doi:10.1093/ije/dyu277.

22. R. F. Hillary, A. J. Stevenson, S. R. Cox, D. L. McCartney, S. E. Harris, A. Seeboth, J. Higham, D. Sproul, A. M. Taylor, P. Redmond, J. Corley, A. Pattie, M. del C. V. Hernández, S. Muñoz-Maniega, M. E. Bastin, J. M. Wardlaw, S. Horvath, C. W. Ritchie, T. L. Spires-Jones, A. M. McIntosh, K. L. Evans, I. J. Deary, R. E. Marioni, An epigenetic predictor of death captures multi-modal measures of brain health. *Molecular Psychiatry*. **26** (2021), doi:10.1038/s41380-019-0616-9.

23. V. Vaccarino, M. Huang, Z. Wang, Q. Hui, A. J. Shah, J. Goldberg, N. Smith, B. Kaseer, N. Murrah, O. M. Levantsevych, Epigenetic age acceleration and cognitive decline: a twin study. *The Journals of Gerontology: Series A*. **76**, 1854–1863 (2021).

24. A. Starnawska, Q. Tan, A. Lenart, M. McGue, O. Mors, A. Børglum, K. Christensen, M. Nyegaard, L. Christiansen, Blood DNA methylation age is not associated with cognitive functioning in middle-aged monozygotic twins. *Neurobiology of aging*. **50**, 60–63 (2017).

25. A. Zhou, Z. Wu, A. Z. Zaw Phyo, D. Torres, S. Vishwanath, J. Ryan, Epigenetic aging as a biomarker of dementia and related outcomes: a systematic review. *Epigenomics*. **14**, 1125–1138 (2022).

26. J. Maddock, J. Castillo-Fernandez, A. Wong, R. Cooper, M. Richards, K. K. Ong, G. B. Ploubidis, A. Goodman, D. Kuh, J. T. Bell, R. Hardy, DNA methylation age and physical and cognitive aging. *Journals of Gerontology - Series A Biological Sciences and Medical Sciences*. **75**, 504–511 (2020).

27. Y. Zheng, M. Habes, M. Gonzales, R. Pomponio, I. Nasrallah, S. Khan, D. E. Vaughan, C. Davatzikos, S. Seshadri, L. Launer, Mid-life epigenetic age, neuroimaging brain age, and cognitive function: coronary artery risk development in young adults (CARDIA) study. *Aging (Albany NY)*. **14**, 1691 (2022).

28. A. I. Wiesman, M. T. Rezich, J. O'Neill, B. Morsey, T. Wang, T. Ideker, S. Swindells, H. S. Fox, T. W. Wilson, Epigenetic Markers of Aging Predict the Neural Oscillations Serving Selective Attention. *Cerebral Cortex*. **30**, 1234–1243 (2020).

29. Z. Shehzad, A. M. C. Kelly, P. T. Reiss, D. G. Gee, K. Gotimer, L. Q. Uddin, S. H. Lee, D. S. Margulies, A. K. Roy, B. B. Biswal, E. Petkova, F. X. Castellanos, M. P. Milham, The Resting Brain: Unconstrained yet Reliable. *Cerebral Cortex*. **19**, 2209–2229 (2009).

30. A. S. Choe, C. K. Jones, S. E. Joel, J. Muschelli, V. Belegu, B. S. Caffo, M. A. Lindquist, P. C. M. van Zijl, J. J. Pekar, Reproducibility and Temporal Structure in Weekly Resting-State fMRI over a Period of 3.5 Years. *PLOS ONE*. **10**, e0140134 (2015).

31. J. R. Andrews-Hanna, A. Z. Snyder, J. L. Vincent, C. Lustig, D. Head, M. E. Raichle, R. L. Buckner, Disruption of large-scale brain systems in advanced aging. *Neuron*. **56**, 924–935 (2007).

32. R. L. Bluhm, P. C. Williamson, E. A. Osuch, P. A. Frewen, T. K. Stevens, K. Boksman, R. W. Neufeld, J. Théberge, R. A. Lanius, Alterations in default network connectivity in posttraumatic stress disorder related to early-life trauma. *Journal of Psychiatry and Neuroscience*. **34**, 187–194 (2009).

33. J. S. Damoiseaux, C. Beckmann, E. S. Arigita, F. Barkhof, P. Scheltens, C. Stam, S. Smith, S. Rombouts, Reduced resting-state brain activity in the "default network" in normal aging. *Cerebral cortex*. **18**, 1856–1864 (2008).

34. L. K. Ferreira, G. F. Busatto, Resting-state functional connectivity in normal brain aging. *Neuroscience & Biobehavioral Reviews*. **37**, 384–400 (2013).

35. W. Koch, S. Teipel, S. Mueller, K. Buerger, A. L. Bokde, H. Hampel, U. Coates, M. Reiser, T. Meindl, Effects of aging on default mode network activity in resting state fMRI: does the method of analysis matter? *Neuroimage*. **51**, 280–287 (2010).

36. K. Onoda, M. Ishihara, S. Yamaguchi, Decreased Functional Connectivity by Aging Is Associated with Cognitive Decline. *Journal of Cognitive Neuroscience*. **24**, 2186–2198 (2012).

37. E. A. Allen, E. B. Erhardt, E. Damaraju, W. Gruner, J. M. Segall, R. F. Silva, M. Havlicek, S. Rachakonda, J. Fries, R. Kalyanam, A baseline for the multivariate comparison of resting-state networks. *Frontiers in systems neuroscience*. **5**, 2 (2011).

38. D. Tomasi, N. D. Volkow, Aging and functional brain networks. *Molecular Psychiatry*. **17**, 549–558 (2012).

39. J. B. Keller, T. Hedden, T. W. Thompson, S. A. Anteraper, J. D. E. Gabrieli, S. Whitfield-Gabrieli, Resting-state anticorrelations between medial and lateral prefrontal cortex: Association with working memory, aging, and individual differences. *Cortex*. **64**, 271–280 (2015).

40. A. E. Reineberg, D. E. Gustavson, C. Benca, M. T. Banich, N. P. Friedman, The Relationship Between Resting State Network Connectivity and Individual Differences in Executive Functions. *Frontiers in Psychology*. **9** (2018) (available at https://www.frontiersin.org/articles/10.3389/fpsyg.2018.01600).

41. L. Wang, P. LaViolette, K. O'Keefe, D. Putcha, A. Bakkour, K. R. Van Dijk, M. Pihlajamäki, B. C. Dickerson, R. A. Sperling, Intrinsic connectivity between the hippocampus and posteromedial cortex predicts memory performance in cognitively intact older individuals. *Neuroimage*. **51**, 910–917 (2010).

42. J. M. Duchek, D. A. Balota, J. B. Thomas, A. Z. Snyder, P. Rich, T. L. Benzinger, A. M. Fagan, D. M. Holtzman, J. C. Morris, B. M. Ances, Relationship between Stroop performance and resting state functional connectivity in cognitively normal older adults. *Neuropsychology*. **27**, 516 (2013).

43. S. Hirsiger, V. Koppelmans, S. Mérillat, F. Liem, B. Erdeniz, R. D. Seidler, L. Jäncke, Structural and functional connectivity in healthy aging: Associations for cognition and motor behavior. *Human Brain Mapping*. **37**, 855–867 (2016).

44. D. Antonenko, M. Meinzer, R. Lindenberg, A. V. Witte, A. Flöel, Grammar learning in older adults is linked to white matter microstructure and functional connectivity. *Neuroimage*. **62**, 1667–1674 (2012).

45. M. Ystad, T. Eichele, A. J. Lundervold, A. Lundervold, Subcortical functional connectivity and verbal episodic memory in healthy elderly—A resting state fMRI study. *NeuroImage*. **52**, 379–388 (2010).

46. H. K. Hausman, A. O'Shea, J. N. Kraft, E. M. Boutzoukas, N. D. Evangelista, E. J. Van Etten, P. K. Bharadwaj, S. G. Smith, E. Porges, G. A. Hishaw, The role of resting-state network functional connectivity in cognitive aging. *Frontiers in aging neuroscience*. **12**, 177 (2020).

47. J. Zhao, P. Manza, C. Wiers, H. Song, P. Zhuang, J. Gu, Y. Shi, G.-J. Wang, D. He, Age-related decreases in interhemispheric resting-state functional connectivity and their relationship with executive function. *Frontiers in aging neuroscience*. **12**, 20 (2020).

48. E. S. Finn, X. Shen, D. Scheinost, M. D. Rosenberg, J. Huang, M. M. Chun, X. Papademetris, R. T. Constable, Functional connectome fingerprinting: Identifying individuals using patterns of brain connectivity. *Nature Neuroscience*. **18**, 1664–1671 (2015).

49. C. Horien, X. Shen, D. Scheinost, R. T. Constable, The individual functional connectome is unique and stable over months to years. *NeuroImage*. **189**, 676–687 (2019).

50. N. U. F. Dosenbach, B. Nardos, A. L. Cohen, D. A. Fair, J. D. Power, J. A. Church, S. M. Nelson, G. S. Wig, A. C. Vogel, C. N. Lessov-Schlaggar, K. A. Barnes, J. W. Dubis, E. Feczko, R. S. Coalson, J. R. Pruett, D. M. Barch, S. E. Petersen, B. L. Schlaggar, *Science*, in press, doi:10.1126/science.1194144.

51. K. Yoo, M. D. Rosenberg, W. T. Hsu, S. Zhang, C. S. R. Li, D. Scheinost, R. T. Constable, M. M. Chun, Connectome-based predictive modeling of attention: Comparing different functional connectivity features and prediction methods across datasets. *NeuroImage*. **167**, 11–22 (2018).

52. R. B. Cattell, Theory of fluid and crystallized intelligence: A critical experiment. *Journal of Educational Psychology*. **54** (1963), doi:10.1037/h0046743.

53. J. L. Horn, R. B. Cattell, Age differences in fluid and crystallized intelligence. *Acta Psychologica*. **26** (1967), doi:10.1016/0001-6918(67)90011-x.

54. K. Siedlecki, Findings From the Virginia Cognitive Aging Project: Individual Differences, Well-Being, and Cognition. *Innovation in Aging*. **4**, 591–592 (2020).

55. S. Datta, D. Roy, Abstract reasoning and Spatial Visualization in Formal Operational Stage. *International Journal of Scientific and Research Publications*. **5** (2015).

56. A. R. Jensen, g: Artifact or reality? *Journal of Vocational Behavior*. **29** (1986), doi:10.1016/0001-8791(86)90011-4.

57. Y. Benjamini, Y. Hochberg, Controlling the False Discovery Rate: A Practical and Powerful Approach to Multiple Testing. *Journal of the Royal Statistical Society: Series B (Methodological)*. **57** (1995), doi:10.1111/j.2517-6161.1995.tb02031.x.

58. A. Salami, S. Pudas, L. Nyberg, Elevated hippocampal resting-state connectivity underlies deficient neurocognitive function in aging. *Proceedings of the National Academy of Sciences*. **111**, 17654–17659 (2014).

59. R. Setton, L. Mwilambwe-Tshilobo, S. Sheldon, G. R. Turner, R. N. Spreng, Hippocampus and temporal pole functional connectivity is associated with age and individual differences in autobiographical memory. *Proceedings of the National Academy of Sciences*. **119**, e2203039119 (2022).

60. J. S. Damoiseaux, R. P. Viviano, P. Yuan, N. Raz, Differential effect of age on posterior and anterior hippocampal functional connectivity. *NeuroImage*. **133**, 468–476 (2016).

61. L. L. Beason-Held, A. T. Shafer, J. O. Goh, B. A. Landman, C. Davatzikos, B. Viscomi, J. Ash, M. Kitner-Triolo, L. Ferrucci, S. M. Resnick, Hippocampal activation and connectivity in the aging brain. *Brain imaging and behavior*. **15**, 711–726 (2021).

62. X. Liang, L.-M. Hsu, H. Lu, J. A. Ash, P. R. Rapp, Y. Yang, Functional connectivity of hippocampal CA3 predicts neurocognitive aging via CA1–frontal circuit. *Cerebral Cortex*. **30**, 4297–4305 (2020).

63. D. Wechsler, *Wechsler Adult Intelligence Scale: Third Edition* (The Psychological Corporation, San Antonio, TX, 1997).

64. T. A. Salthouse, R. L. Babcock, Decomposing Adult Age Differences in Working Memory. *Developmental Psychology*. **27** (1991), doi:10.1037/0012-1649.27.5.763.

65. T. A. Salthouse, R. L. Babcock, Decomposing Adult Age Differences in Working Memory. *Developmental Psychology*. **27** (1991), doi:10.1037/0012-1649.27.5.763.

66. D. Wechsler, *Wechsler Memory Scale – Third Edition* (The Psychological Corporation, San Antonio, TX, 1997).

67. T. A. Salthouse, N. Fristoe, S. H. Rhee, How localized are age-related effects on neuropsychological measures? *Neuropsychology*. **10** (1996), doi:10.1037/0894-4105.10.2.272.

68. G. K. Bennett, H. G. Seashore, A. G. Wesman, *Differential Aptitude Test* (The Psychological Corporation, San Antonio, TX, 1997).

69. R. B. Ekstrom, J. W. French, H. H. Harman, *Manual for kit of factor-referenced cognitive tests* (Educational Testing Service, Princeton, NJ, 1976).

70. J. Raven, *Advanced Progressive Matrices, Set II* (H.K. Lewis, London, 1962).

71. R. A. Zachary, *Shipley Institute of Living Scale - Revised* (Western Psychological Services, Los Angeles, CA, 1986).

72. T. A. Salthouse, Speed and knowledge as determinants of adult age differences in verbal tasks. *Journals of Gerontology*. **48** (1993), doi:10.1093/geronj/48.1.P29.

73. M. J. Aryee, A. E. Jaffe, H. Corrada-Bravo, C. Ladd-Acosta, A. P. Feinberg, K. D. Hansen, R. A. Irizarry, Minfi: A flexible and comprehensive Bioconductor package for the analysis of Infinium DNA methylation microarrays. *Bioinformatics*. **30** (2014), doi:10.1093/bioinformatics/btu049.

74. J. P. Fortin, T. J. Triche, K. D. Hansen, Preprocessing, normalization and integration of the Illumina HumanMethylationEPIC array with minfi. *Bioinformatics*. **33** (2017), doi:10.1093/bioinformatics/btw691.

75. E. A. Houseman, W. P. Accomando, D. C. Koestler, B. C. Christensen, C. J. Marsit, H. H. Nelson, J. K. Wiencke, K. T. Kelsey, DNA methylation arrays as surrogate measures of cell mixture distribution. *BMC Bioinformatics*. **13** (2012), doi:10.1186/1471-2105-13-86.

76. A. E. Jaffe, R. A. Irizarry, Accounting for cellular heterogeneity is critical in epigenome-wide association studies. *Genome Biology*. **15** (2014), doi:10.1186/gb-2014-15-2-r31.

77. J. P. Fortin, E. Fertig, K. Hansen, shinyMethyl: Interactive quality control of Illumina 450k DNA methylation arrays in R. *F1000Research*. **3** (2014), doi:10.12688/f1000research.4680.2.

78. J. A. Heiss, A. C. Just, Identifying mislabeled and contaminated DNA methylation microarray data: An extended quality control toolset with examples from GEO. *Clinical Epigenetics*. **10** (2018), doi:10.1186/s13148-018-0504-1.

79. A. T. Lu, A. Quach, J. G. Wilson, A. P. Reiner, A. Aviv, K. Raj, L. Hou, A. A. Baccarelli, Y. Li, J. D. Stewart, E. A. Whitsel, T. L. Assimes, L. Ferrucci, S. Horvath, DNA methylation GrimAge strongly predicts lifespan and healthspan. *Aging*. **11** (2019), doi:10.18632/aging.101684.

80. L. M. McEwen, M. J. Jones, D. T. S. Lin, R. D. Edgar, L. T. Husquin, J. L. MacIsaac, K. E. Ramadori, A. M. Morin, C. F. Rider, C. Carlsten, L. Quintana-Murci, S. Horvath, M. S. Kobor, Systematic evaluation of DNA methylation age estimation with common preprocessing methods and the Infinium MethylationEPIC BeadChip array. *Clinical Epigenetics*. **10** (2018), doi:10.1186/s13148-018-0556-2.

81. O. Esteban, C. J. Markiewicz, R. W. Blair, C. A. Moodie, A. I. Isik, A. Erramuzpe, J. D. Kent, M. Goncalves, E. DuPre, M. Snyder, H. Oya, S. S. Ghosh, J. Wright, J. Durnez, R. A. Poldrack, K. J. Gorgolewski, fMRIPrep: a robust preprocessing pipeline for functional MRI. *Nature Methods*. **16**, 111–116 (2019).

82. K. Gorgolewski, C. Burns, C. Madison, D. Clark, Y. Halchenko, M. Waskom, S. Ghosh, Nipype: A Flexible, Lightweight and Extensible Neuroimaging Data Processing Framework in Python. *Frontiers in Neuroinformatics*. **5** (2011) (available at https://www.frontiersin.org/articles/10.3389/fninf.2011.00013).

83. A. Abraham, F. Pedregosa, M. Eickenberg, P. Gervais, A. Mueller, J. Kossaifi, A. Gramfort, B. Thirion, G. Varoquaux, Machine learning for neuroimaging with scikit-learn. *Frontiers in Neuroinformatics*. **8** (2014) (available at https://www.frontiersin.org/articles/10.3389/fninf.2014.00014).

84. N. J. Tustison, B. B. Avants, P. A. Cook, Y. Zheng, A. Egan, P. A. Yushkevich, J. C. Gee, N4ITK: Improved N3 Bias Correction. *IEEE Transactions on Medical Imaging*. **29**, 1310–1320 (2010).

85. B. B. Avants, C. L. Epstein, M. Grossman, J. C. Gee, Symmetric diffeomorphic image registration with cross-correlation: Evaluating automated labeling of elderly and neurodegenerative brain. *Medical Image Analysis*. **12**, 26–41 (2008).

86. Y. Zhang, M. Brady, S. Smith, Segmentation of brain MR images through a hidden Markov random field model and the expectation-maximization algorithm. *IEEE Transactions on Medical Imaging*. **20**, 45–57 (2001).

87. V. Fonov, A. Evans, R. McKinstry, C. Almli, D. Collins, Unbiased nonlinear average age-appropriate brain templates from birth to adulthood. *NeuroImage*. **47**, S102 (2009).

88. S. Wang, D. J. Peterson, J. C. Gatenby, W. Li, T. J. Grabowski, T. M. Madhyastha, Evaluation of field map and nonlinear registration methods for correction of susceptibility artifacts in diffusion MRI. *Frontiers in neuroinformatics*. **11**, 17 (2017).

89. J. M. Huntenburg, Evaluating nonlinear coregistration of BOLD EPI and T1w images (2014).

90. J. M. Treiber, N. S. White, T. C. Steed, H. Bartsch, D. Holland, N. Farid, C. R. McDonald, B. S. Carter, A. M. Dale, C. C. Chen, Characterization and correction of geometric distortions in 814 diffusion weighted images. *PloS one*. **11**, e0152472 (2016).

91. M. Jenkinson, P. Bannister, M. Brady, S. Smith, Improved Optimization for the Robust and Accurate Linear Registration and Motion Correction of Brain Images. *NeuroImage*. **17**, 825–841 (2002).

92. R. W. Cox, J. S. Hyde, Software tools for analysis and visualization of fMRI data. *NMR in Biomedicine*. **10**, 171–178 (1997).

93. M. Jenkinson, S. Smith, A global optimisation method for robust affine registration of brain images. *Medical Image Analysis*. **5**, 143–156 (2001).

94. D. N. Greve, B. Fischl, Accurate and robust brain image alignment using boundary-based registration. *NeuroImage*. **48**, 63–72 (2009).

95. J. D. Power, A. Mitra, T. O. Laumann, A. Z. Snyder, B. L. Schlaggar, S. E. Petersen, Methods to detect, characterize, and remove motion artifact in resting state fMRI. *NeuroImage*. **84**, 320–341 (2014).

96. Y. Behzadi, K. Restom, J. Liau, T. T. Liu, A component based noise correction method (CompCor) for BOLD and perfusion based fMRI. *NeuroImage*. **37**, 90–101 (2007).

97. T. D. Satterthwaite, M. A. Elliott, R. T. Gerraty, K. Ruparel, J. Loughead, M. E. Calkins, S. B. Eickhoff, H. Hakonarson, R. C. Gur, R. E. Gur, D. H. Wolf, An improved framework for confound regression and filtering for control of motion artifact in the preprocessing of resting-state functional connectivity data. *NeuroImage*. **64**, 240–256 (2013).

98. C. Lanczos, Evaluation of Noisy Data. *Journal of the Society for Industrial and Applied Mathematics Series B Numerical Analysis*. **1**, 76–85 (1964).

99. X. Shen, F. Tokoglu, X. Papademetris, R. T. Constable, Groupwise whole-brain parcellation from resting-state fMRI data for network node identification. *NeuroImage*. **82**, 403–415 (2013).

100. J. W. Cho, A. Korchmaros, J. T. Vogelstein, M. P. Milham, T. Xu, Impact of concatenating fMRI data on reliability for functional connectomics. *NeuroImage*. **226**, 117549 (2021).

101. H. F. Golino, S. Epskamp, Exploratory graph analysis: A new approach for estimating the number of dimensions in psychological research. *PLoS ONE*. **12** (2017), doi:10.1371/journal.pone.0174035.

102. A. P. Christensen, H. Golino, Estimating the Stability of Psychological Dimensions via Bootstrap Exploratory Graph Analysis: A Monte Carlo Simulation and Tutorial. *Psych*. **3** (2021), doi:10.3390/psych3030032.

103. H. Golino, D. Shi, A. P. Christensen, L. E. Garrido, M. D. Nieto, R. Sadana, J. A. Thiyagarajan, A. Martínez-Molina, Investigating the performance of Exploratory Graph Analysis and traditional techniques to identify the number of latent factors: A simulation and tutorial. *Psychological Methods*. **25** (2019), doi:10.1037/met0000255.

104. J. Friedman, T. Hastie, R. Tibshirani, Sparse inverse covariance estimation with the graphical lasso. *Biostatistics*. **9** (2008), doi:10.1093/biostatistics/kxm045.

105. P. Pons, M. Latapy, Computing communities in large networks using random walks. *Journal of Graph Algorithms and Applications*. **10** (2006), doi:10.7155/jgaa.00124.

106. A. P. Christensen, H. Golino, On the equivalency of factor and network loadings. *Behavior Research Methods*. **53** (2021), doi:10.3758/s13428-020-01500-6.

107. C. G. Bell, R. Lowe, P. D. Adams, A. A. Baccarelli, S. Beck, J. T. Bell, B. C. Christensen, V. N. Gladyshev, B. T. Heijmans, S. Horvath, DNA methylation aging clocks: challenges and recommendations. *Genome biology*. **20**, 1–24 (2019).

108. A. Gelman, J. Hill, *Data Analysis Using Regression and Multilevel/Hierarchical Models* (2006).

109. P. C. Bürkner, brms: An R package for Bayesian multilevel models using Stan. *Journal of Statistical Software*. **80** (2017), doi:10.18637/jss.v080.i01.

110. M. D. Hoffman, A. Gelman, The no-U-turn sampler: Adaptively setting path lengths in Hamiltonian Monte Carlo. *Journal of Machine Learning Research*. **15** (2014).

111. D. J. Schad, M. Betancourt, S. Vasishth, Toward a principled Bayesian workflow in cognitive science. *Psychological Methods*. **26** (2021), doi:10.1037/met0000275.

112. P. C. Bürkner, brms: An R package for Bayesian multilevel models using Stan. *Journal of Statistical Software*. **80** (2017), doi:10.18637/jss.v080.i01.

113. J. N. Rouder, P. L. Speckman, D. Sun, R. D. Morey, G. Iverson, Bayesian t tests for accepting and rejecting the null hypothesis. *Psychonomic bulletin & review*. **16**, 225–237 (2009).

114. S. Theodoridis, *Machine Learning: A Bayesian and Optimization Perspective* (2015).

115. S. Gao, A. S. Greene, R. T. Constable, D. Scheinost, Combining multiple connectomes improves predictive modeling of phenotypic measures. *NeuroImage*. **201**, 116038 (2019).

Figures and Tables

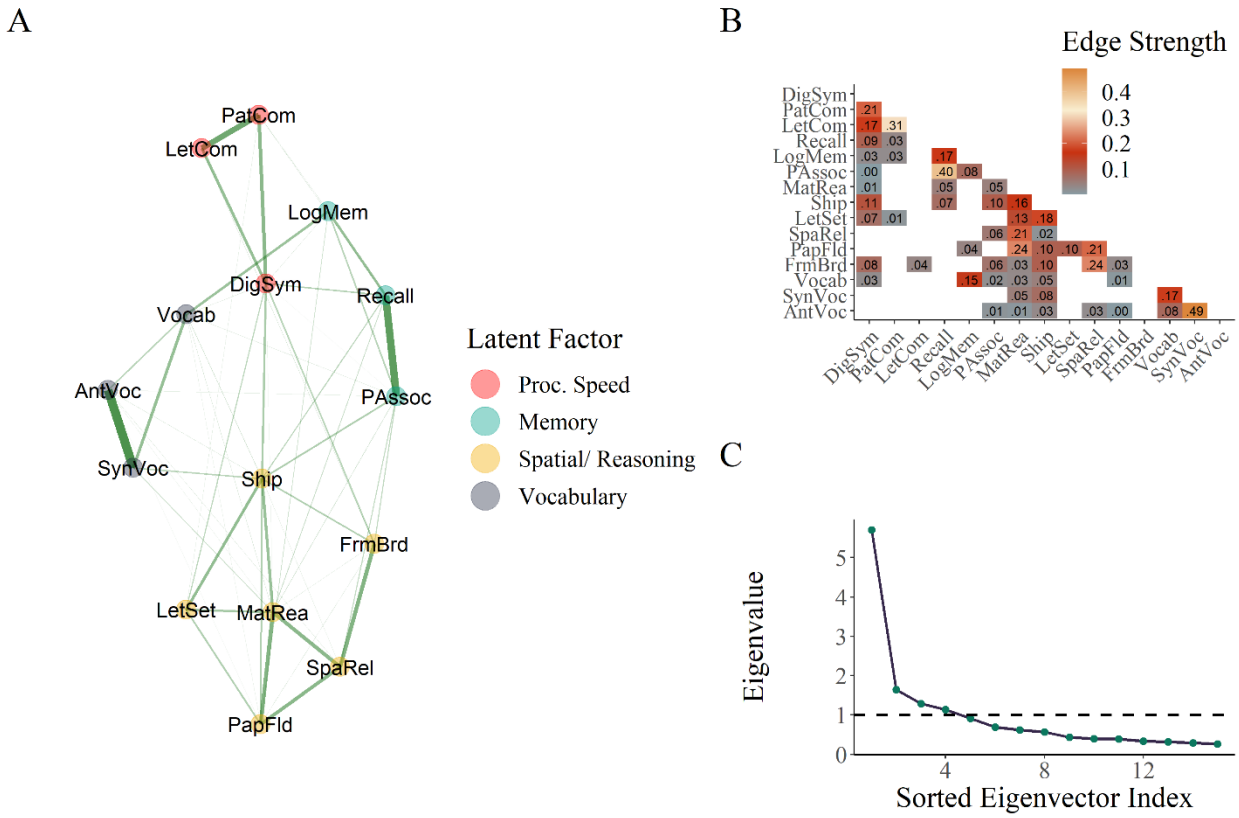

Fig. 1. Four latent domains estimated from the cognitive battery using bootEGA. Panel A shows the estimated graph of the cognitive battery, where distinct colors reflect distinct communities and the size of the edges between nodes reflects the strength of the connection. Panel B shows the regularized partial correlation matrix that is a numeric representation of the graph, where white space indicates no connection between those nodes, and the cell entries represent edge strength between each node. This is the adjacency matrix for the graph and was estimated using GLASSO. Panel C shows the eigenvalue-eigenvector decomposition of the cognitive battery, providing additional supporting evidence that there are approximately 4 latent variables among the original set of items.

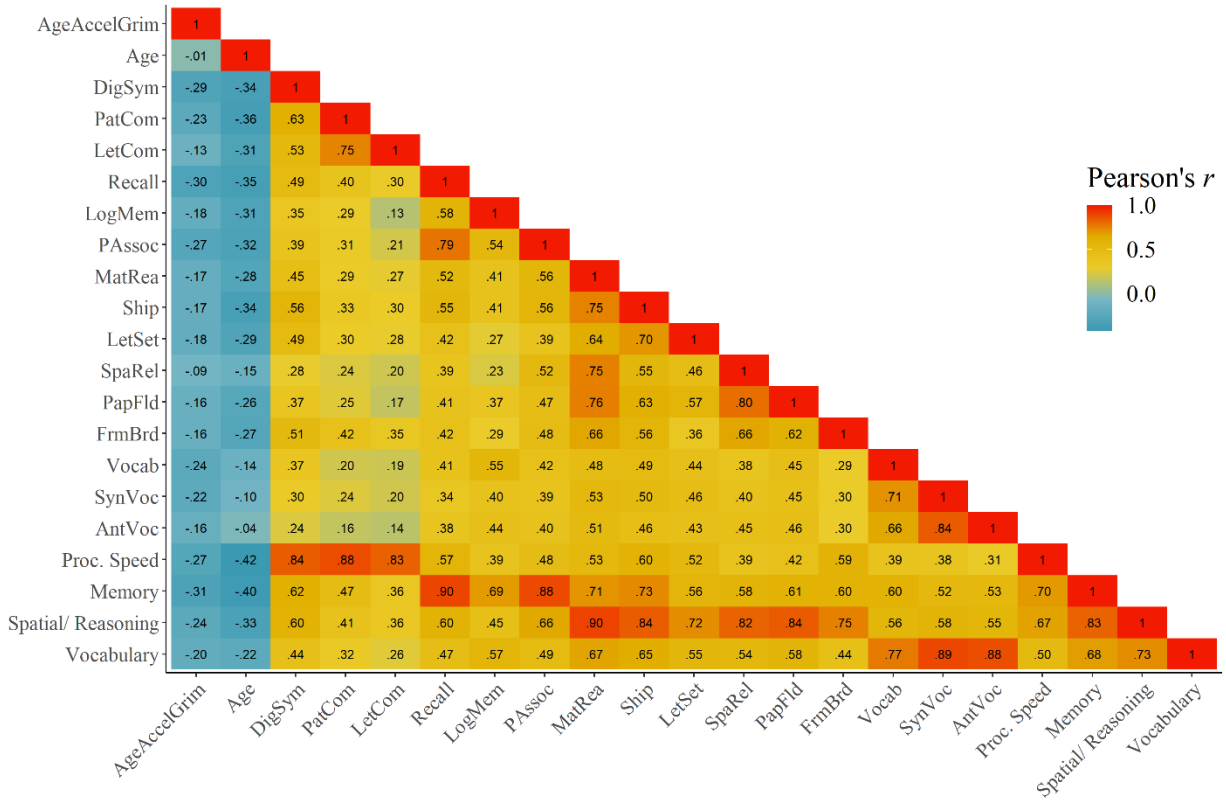

Fig. 2. AgeAccelGrim negatively correlates with all cognitive items measured.
Shown is the raw correlation matrix between AgeAccelGrim, chronological age, the original cognitive items, and the 4 latent cognitive domains. Data is aggregated over the three sessions by taking the mean for this visualization. There is no linear relationship between AgeAccelGrim and chronological age. At the marginal level, both AgeAccelGrim and chronological age negatively associate to some degree with all of the cognitive items surveyed, as well as the 4 latent domains. As expected, the cognitive items and latent cognitive domains are positively correlated with each other.

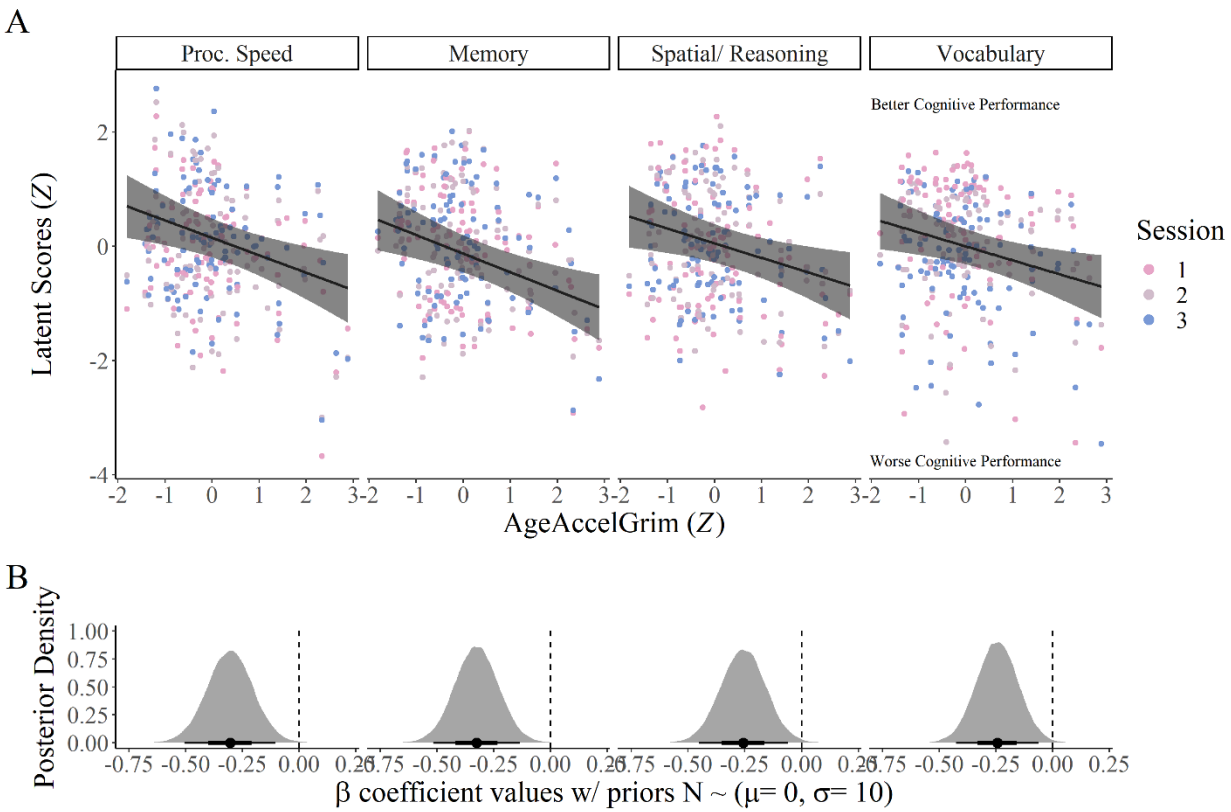

Fig. 3. AgeAccelGrim negatively associates with all 4 latent cognitive domains after adjusting for chronological age and all covariates. Panel A shows the posterior estimates for the AgeAccelGrim regression coefficients for each response variable as black lines with uncertainty bands showing the uncertainty. Overlaid are the raw data used to fit the model, which includes session-level information. Panel B shows the density plots on the bottom of the entire posterior distribution of parameter values, with 95% credible intervals indicated by the lines underneath the density. There is very little overlap with 0, suggesting that the relationship between AgeAccelGrim, conditional on chronological age and all other covariates, is reliably negative. The actual posterior probability values are included in the main text.

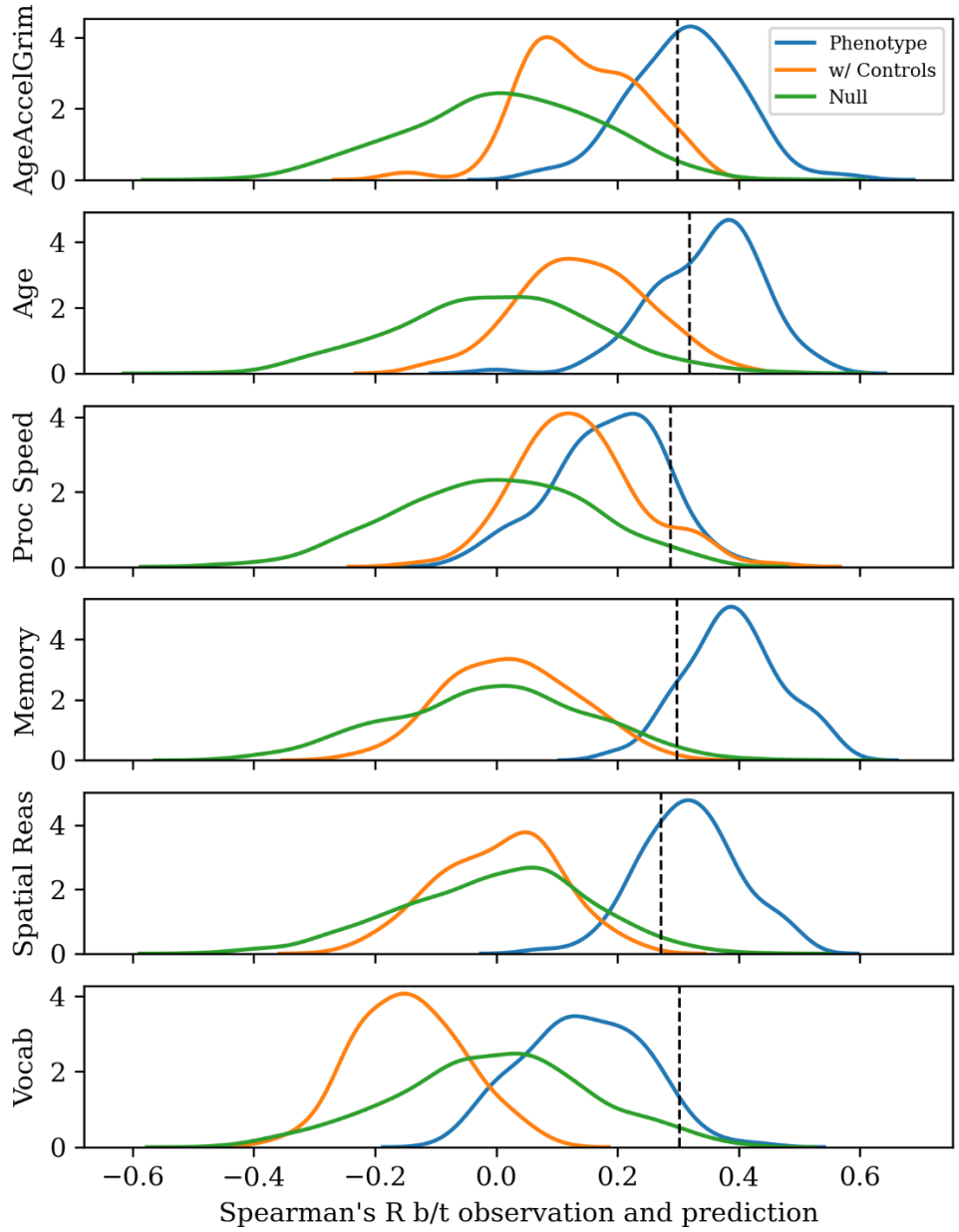

Fig. 4. rCPM significantly predicts AgeAccelGrim, Age, and Memory/ Spatial Reasoning. Using both fMRI resting state input scans, rCPM can predict epigenetic age and chronological age, as well as memory and spatial reasoning (which are highly positively correlated). The phenotype (blue) distributions for the AgeAccelGrim analysis controlled for age, sex and the time difference between blood draw/ brain scan and cognitive assessment, and conversely the age analysis controlled for AgeAccelGrim, sex, and the time difference. The control-adjusted (orange) distributions for AgeAccelGrim and Age additionally controlled for all four cognitive factors. The phenotype (blue) distributions of the cognitive factors controlled for sex and time difference. The control-adjusted (orange) distributions for all four cognitive factors additionally controlled for Age and AgeAccelGrim. These results show that the functional connectome contains information uniquely relevant for both epigenetic age and chronological age, and that information is shared with individual differences in cognition, particularly memory.

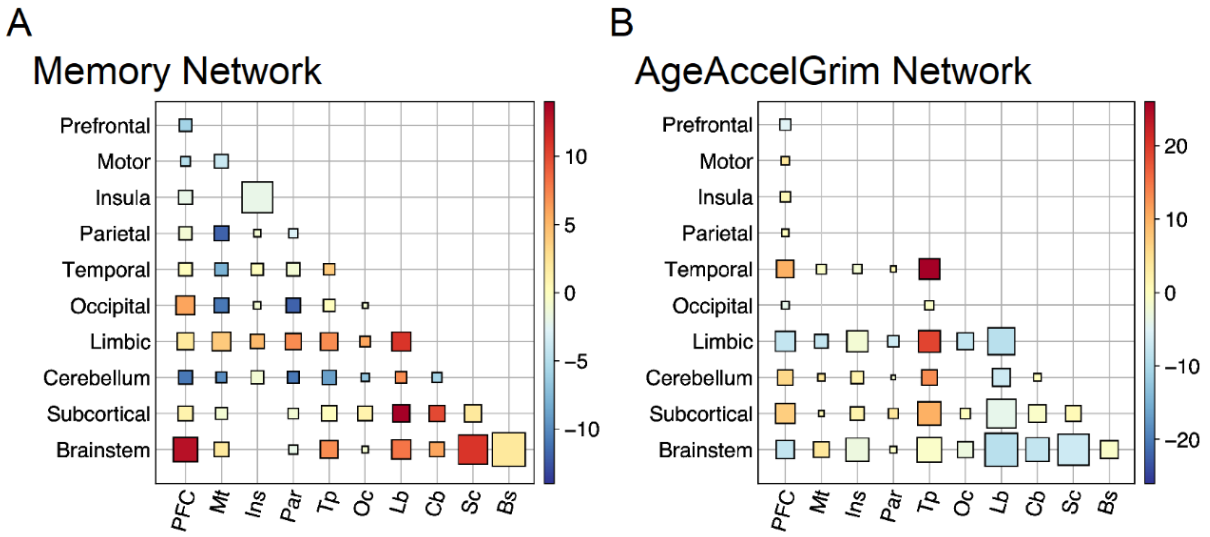

Fig. 5. Networks reflective of memory performance and AgeAccelGrim show largely opposite patterns at the lobe-level. Hinton plot visualizations show that memory and AgeAccelGrim have opposing network structure patterns, suggesting that better memory and slower epigenetic age acceleration (and vice versa) are captured through similar lobe-level connections through the functional connectome. Size corresponds to the sum of edges in the "high"- and "low" networks standardized by the number of possible edges between each pair of regions. Color corresponds to the difference between edges in the high- and low-phenotype networks, such that red corresponds to edges mostly in the better memory/ more epigenetic age accelerated network and blue corresponds to edges mostly in the worse memory/ less epigenetic age accelerated network. In particular, the limbic, cerebellar, and brainstem networks, as well as the subcortical connections to those three networks, have opposing strength. These results are in line with the hypothesis that epigenetic age acceleration and memory performance are negatively correlated at least in part due to functional brain activity differences.

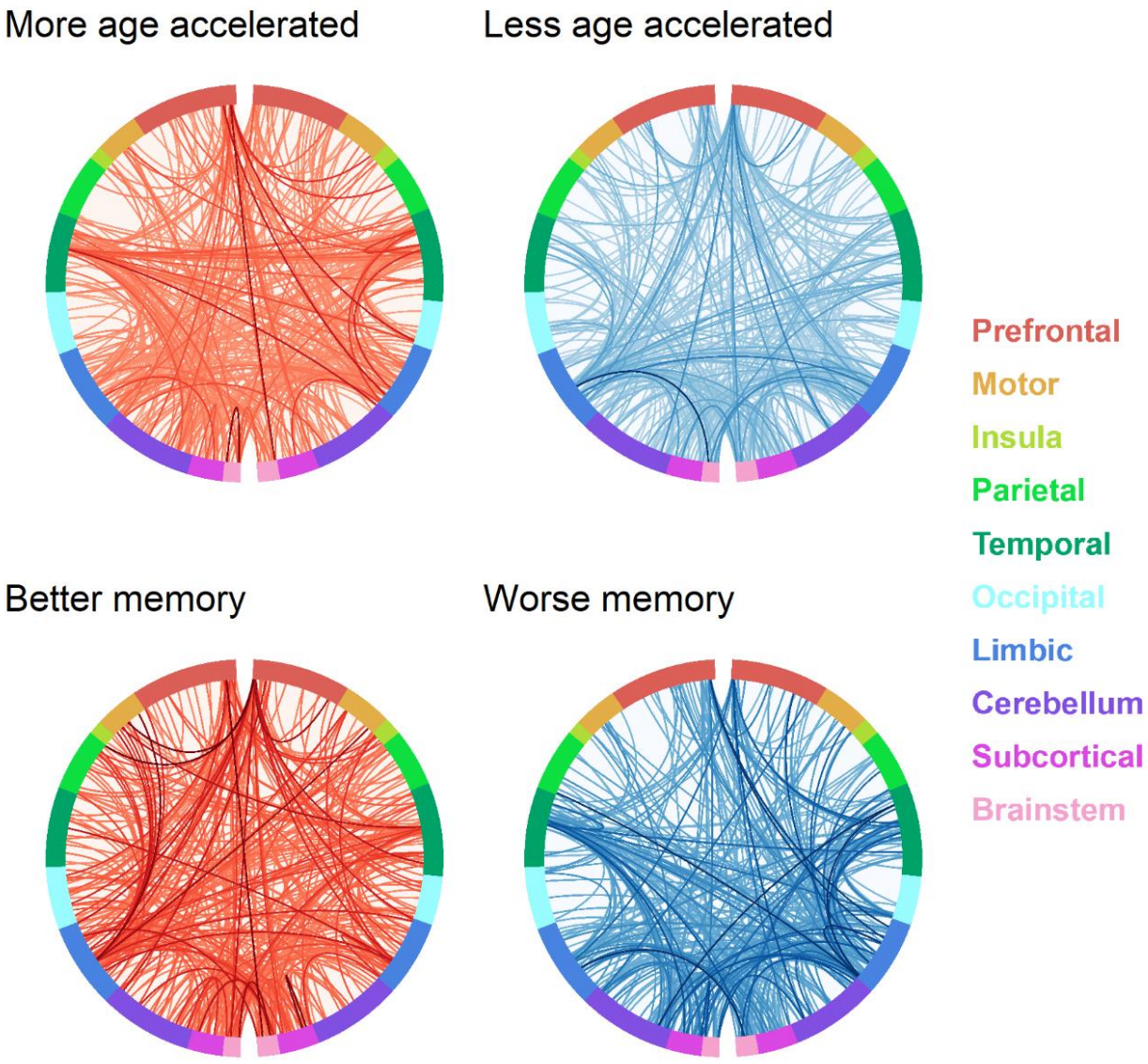

Fig. 6. Networks reflective of memory performance and AgeAccelGrim show largely opposite patterns at the edge-level. Circle plot diagrams show that memory and AgeAccelGrim have opposing network structure patterns, suggesting that better memory and slower epigenetic age acceleration (and vice versa) are captured through similar edge-level connections through the functional connectome. Edges in the positive networks are visualized in red, and edges in the negative network are visualized in blue. Darker lines correspond to edges with higher strength (absolute value).

Trait	*Minimum*	*Mean*	*Maximum*	*SD*
Age-related variables				
Age	59	68.98	81	5.68
AgeAccelGrim	-6.46	-0.16	9.88	3.49
DNAmGrimAge	54.77	64.95	79.84	5.52
Time Difference (Days)	21	331.54	1288	124.13
Cognitive measurements				
DigSym	35	72.24	107.67	12.61
PatCom	6.5	14.78	25.5	3.2
LetCom	4.5	9.71	17.17	2.05
Recall	17.33	34.32	46.67	6.2
LogMem	21.67	48.33	64	8.32
PAssoc	0.33	2.79	5.83	1.51
MatRea	2	7.26	13.33	2.81
Ship	4	12.86	18.67	2.91
LetSet	3.33	11.36	14	1.87
SpaRel	3.33	9.49	16.67	3.43
PapFld	2	6.16	11	2.44
FrmBrd	1	6.43	13	2.8
Vocab	17.67	53.59	62.67	6.87
SynVoc	3.33	7.82	9.67	1.47
AntVoc	2.67	7.35	10	1.65

Table 1. VCAP Participant Summary Statistics. Cognitive measurements were averaged across the three sessions here for computing participant-level summary statistics.

β coefficient	*Proc. Speed*	*Memory*	*Spatial/ Reasoning*	*Vocabulary*
Parameters of Interest				
Intercept	0.15 [-0.19, 0.49]	-0.13 [-0.46, 0.20]	0.05 [-0.28, 0.39]	0.00 [-0.31, 0.31]
AgeAccelGrim	**-0.31 [-0.51, -0.11]**	**-0.33 [-0.52, -0.13]**	**-0.26 [-0.45, -0.06]**	**-0.24 [-0.43, -0.06]**
Age	**-0.39 [-0.58, -0.21]**	**-0.45 [-0.62, -0.27]**	**-0.33 [-0.51, -0.15]**	**-0.20 [-0.37, -0.04]**
Covariates				
Time Difference	0.03 [-0.14, 0.20]	0.10 [-0.06, 0.27]	0.14 [-0.03, 0.30]	0.01 [-0.14, 0.17]
Session	**0.06 [0.02, 0.10]**	0.01 [-0.03, 0.04]	0.02 [-0.02, 0.07]	**-0.18 [-0.23, -0.12]**
Sex (Female)	-0.21 [-0.63, 0.21]	0.18 [-0.22, 0.58]	-0.06 [-0.47, 0.35]	0.09 [-0.28, 0.47]
NK	0.05 [-0.22, 0.32]	0.18 [-0.08, 0.43]	0.17 [-0.09, 0.43]	0.07 [-0.17, 0.30]
Mono	-0.11 [-0.30, 0.07]	-0.10 [-0.28, 0.08]	-0.11 [-0.29, 0.07]	-0.06 [-0.22, 0.11]
Gran	-0.05 [-0.41, 0.30]	0.03 [-0.31, 0.36]	0.04 [-0.31, 0.38]	0.14 [-0.18, 0.45]
PlasmaBlast	0.19 [-0.07, 0.44]	0.11 [-0.13, 0.35]	0.06 [-0.19, 0.30]	0.01 [-0.21, 0.24]
CD8pCD28nCD45RAn	-0.02 [-0.24, 0.21]	0.02 [-0.19, 0.23]	0.09 [-0.12, 0.31]	0.06 [-0.13, 0.27]
CD8.naive	0.11 [-0.14, 0.35]	0.03 [-0.21, 0.26]	0.02 [-0.22, 0.25]	0.09 [-0.14, 0.31]
CD4.naive	-0.12 [-0.38, 0.14]	-0.10 [-0.35, 0.15]	-0.04 [-0.29, 0.22]	-0.17 [-0.40, 0.06]

Table 2. Bayesian Multivariate Population Parameter Estimates and Associated Uncertainty. Bold cell entries indicate 95% credible intervals that do not overlap with 0.

Node #	*X*	*Y*	*Z*	*Region*	*Lobe*	*Centrality*	*Top Neurosynth Terms*
Better Memory							
94	**35.6**	**-14.7**	**-18.4**	**Hippocampus**	**Limbic**	**0.17**	**hippocampus, hippocampal, memory**
136	**-5.8**	**18.2**	**-21.6**	**Orbitofrontal**	**Prefrontal**	**0.16**	**subgenual, major depression, depression**
195	-37.8	-13.2	-29.3	Inferior Temporal Gyrus	Motor	0.14	anterior temporal, temporal, medial temporal
18	26.6	19.6	-21.3	Pars Orbitalis	Prefrontal	0.13	cortex ofc, ofc, orbitofrontal
3	5.1	34.9	-17.4	Orbitofrontal	Prefrontal	0.12	orbitofrontal, orbitofrontal cortex, medial orbitofrontal
125	14	8.3	-9.5	Putamen	Prefrontal	0.12	reward, ventral striatum, striatum
Less Age Accelerated							
94	**35.6**	**-14.7**	**-18.4**	**Hippocampus**	**Limbic**	**0.20**	**hippocampus, hippocampal, memory**
136	**-5.8**	**18.2**	**-21.6**	**Orbitofrontal**	**Prefrontal**	**0.15**	**subgenual, major depression, depression**
268	-6.1	-18.9	-36.8	Brainstem	Brainstem	0.14	N/A
227	-7.5	-42.1	13.3	Agranular Retrolimbic	Limbic	0.13	retrosplenial cortex, retrosplenial, posterior cingulate
229	-21.5	-36.9	5.7	Hippocampus	Limbic	0.13	hippocampus, hippocampal, learning task
96	29.3	-19.6	-26.3	Parahippocampal	Limbic	0.12	medial temporal, hippocampus, parahippocampal

Table 3. Most important functional connectivity regions for better memory and slower epigenetic age acceleration. The top two nodes are shared across these phenotypes and the remaining structures are largely implicated in learning and memory processes.

Node #	*X*	*Y*	*Z*	*Region*	*Lobe*	*Centrality*	*Top Neurosynth Terms*
Worse Memory							
59	**43.4**	**-26.5**	**-24.6**	**InfTempGyrus**	**Temporal**	**0.19**	**photographs, temporal lobe, medial temporal**
234	**-30.5**	**-23.9**	**-26.6**	**Parahipp**	**Limbic**	**0.19**	**lobe mtl, hippocampal, mtl**
122	13.7	-4.2	20.9	Caudate	Subcortical	0.14	caudate, caudate nucleus, nucleus
58	40.3	-11.3	-35.8	InfTempGyrus	Motor	0.13	face recognition, medial temporal, temporal lobe
217	-23.6	-41.3	19.9	NA	Limbic	0.13	N/A
230	-32.1	-40.2	-4	Hippocampus	Limbic	0.13	hippocampal, medial temporal, hippocampus
More Age Accelerated							
59	**43.4**	**-26.5**	**-24.6**	**InfTempGyrus**	**Temporal**	**0.21**	**photographs, temporal lobe, medial temporal**
2	9.6	17.8	-19.5	OrbFrontal	Prefrontal	0.15	interpersonal, frontotemporal, cognitive emotional
120	21.2	-36.4	22.6	NA	Subcortical	0.15	N/A
92	31.2	3.7	-21.6	Amygdala	Limbic	0.14	amygdala, amygdala insula, fear
234	**-30.5**	**-23.9**	**-26.6**	**Parahipp**	**Limbic**	**0.14**	**lobe mtl, hippocampal, mtl**
127	12.3	-27.7	13.5	Thalamus	Subcortical	0.13	caudate nucleus, thalamic, insula inferior

Table 4. Most important functional connectivity regions for worse memory and faster epigenetic age acceleration. The top node (as well as 2nd memory node and 4th AgeAccelGrim node) are shared across these phenotypes and the remaining cortical structures are largely implicated in learning and memory processes.

Supporting Information for Chapter 2: Accelerated epigenetic aging associates with whole-brain functional connectivity and impaired cognitive performance in older adults

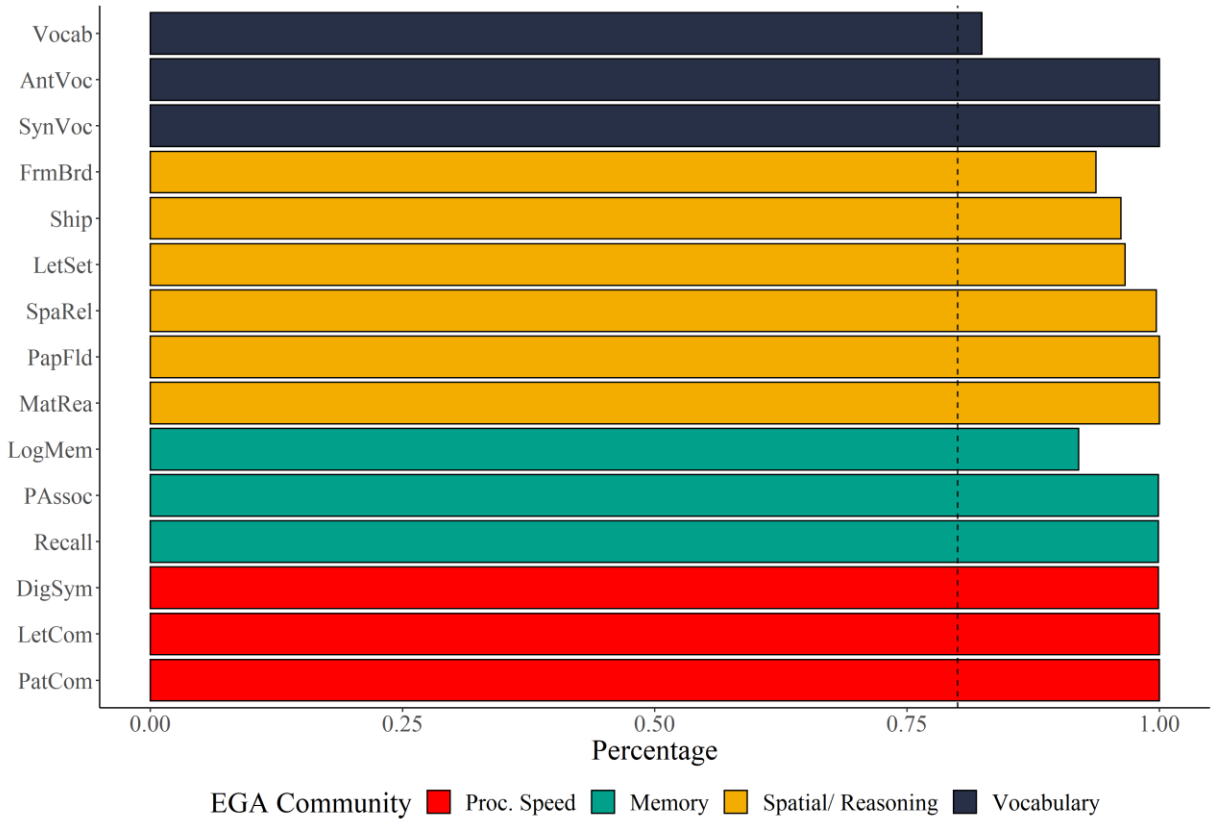

Fig. S1. All cognitive items were stably estimated into discrete communities from bootEGA. Stability was assessed via generation of 1000 multivariate normal replicates of the original data. Higher item percentages are roughly analogous to higher loadings in traditional factor analysis. The replications provide insight into the uncertainty of the community structure. Heuristically, items that demonstrate greater than 80% replication percentage are considered relatively stable, and each item exceeds that threshold. This suggests that this identical structure would likely replicate upon collection of a new sample.

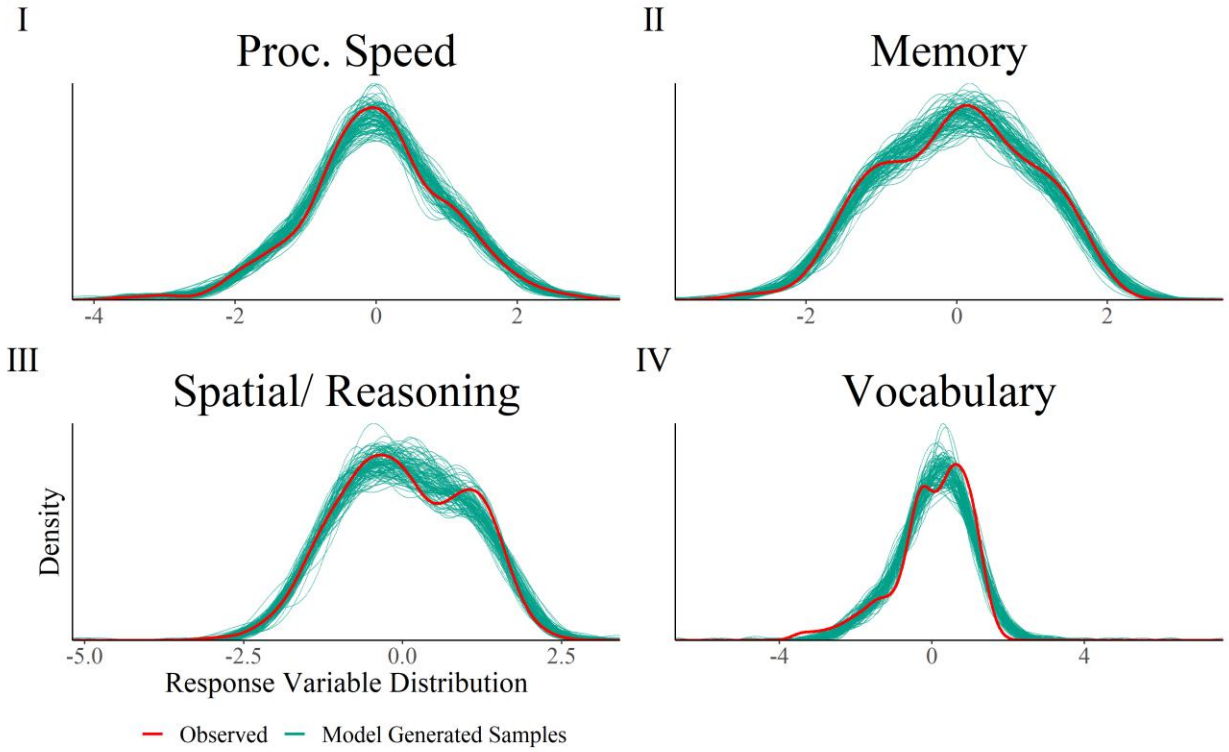

Fig. S2. Posterior predictive distribution check shows good overlap with model simulations and observed data. This provides visual diagnostic information that the Bayesian model is adequately specified, and that the mathematical assumptions appear sufficient for representing the data generation process. Each of these posterior distribution panels represent Student-T likelihoods jointly estimated from the four response variables in the multivariate hierarchical model. The Vocabulary response variable exhibits wider tails because the posterior estimation of the degrees of freedom was lower than the other three response variables, which motivated the use of a stronger prior specifically on the degrees of freedom parameter, υ, for Vocabulary. This improved model stability without sacrificing the capacity to do inference for this response variable.

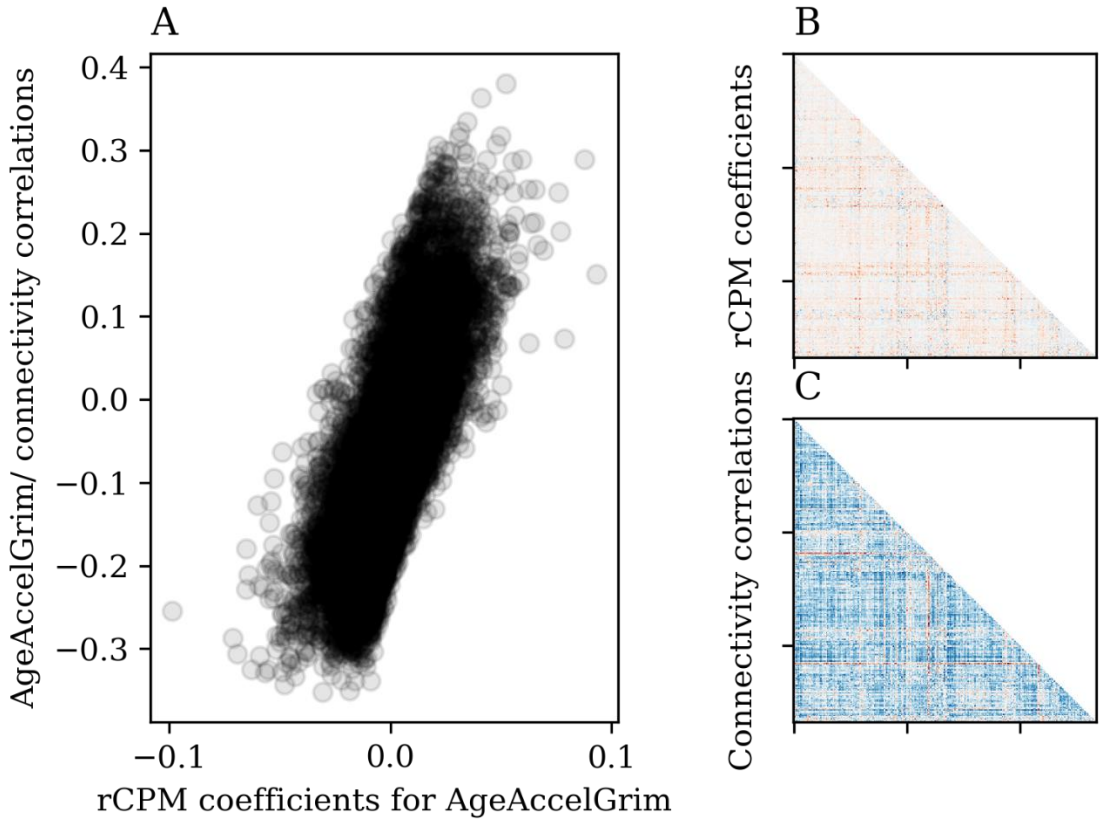

Fig. S3. rCPM captures and filters functional connectivity-phenotype relationships. Using AgeAccelGrim as a demonstrative example, the correlation between rCPM coefficients and simple bivariate correlations with phenotype is strong and positive. This is indicated both by the scatterplot in Panel A and the similarity between important nodes in the two matrix heatmaps in Panels B and C. Each row/column in the heatmap matrices corresponds to a unique brain region, and each cell entry represents the correlation between pairwise connectivity of those two regions and phenotype (i.e., AgeAccelGrim). This suggests that analyzing the degree network statistic of the rCPM coefficient matrix will recover which brain regions are uniquely important for predicting AgeAccelGrim, and can be interpreted in a similar fashion to summing the bivariate correlation values of a specific brain region to determine importance.

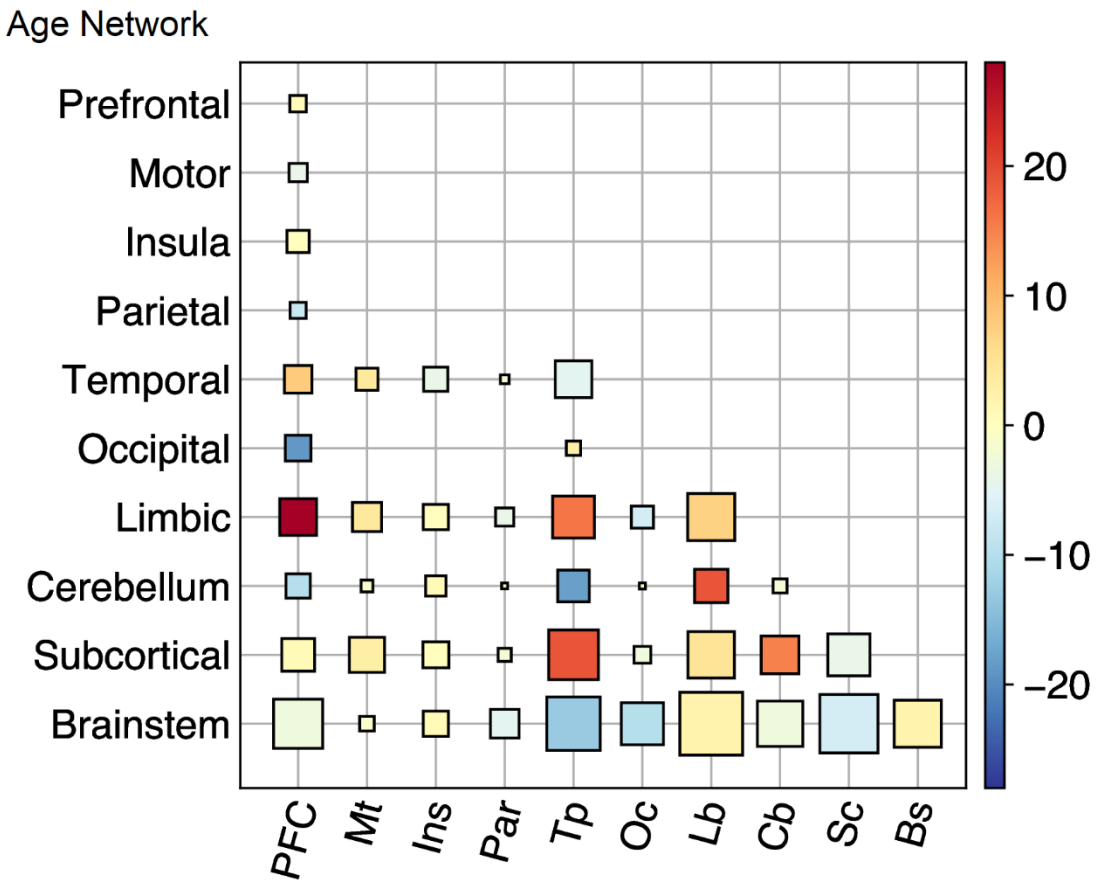

Fig. S4. Networks reflective of age do not show opposite patterns in limbic system to memory networks. Hinton plot visualizations show that memory (see Figure 5 in main manuscript) and age, in contrast to AgeAccelGrim, do not have opposing network structure patterns in the limbic system. Size corresponds to the sum of edges in the "high"- and "low" networks standardized by the number of possible edges between each pair of regions. Color corresponds to the difference between edges in the high- and low-phenotype networks, such that red corresponds to edges mostly in the older age network and blue corresponds to edges mostly in the younger age network.

Table S1. Most important functional connectivity regions for predicting older age and younger age.

Node #	*X*	*Y*	*Z*	*Region*	*Lobe*	*Centrality*	*Top Neurosynth Terms*
Older Age							
121	12.7	12.9	11.5	Caudate	Subcortical	0.14	social, imagine, construction
185	-38	6.1	-37.9	Temporal Pole	Temporal	0.14	semantic memory, social interactions, default network
194	-49.3	-4.7	-37.4	Inferior Temporal Gyrus	Temporal	0.14	caudate, caudate nucleus, nucleus
87	28.4	-53.8	7.1	Ventral Posterior Cingulate	Limbic	0.13	N/A
94	35.6	-14.7	-18.4	Hippocampus	Limbic	0.13	hippocampus, hippocampal, memory
202	-30	-5.8	-40.9	Parahippocampal	Temporal	0.13	progressive, aphasia, dementia
Younger Age							
132	6.3	-24.9	-17.5	Brainstem	Brainstem	0.17	ventral tegmental, tegmental, midbrain
195	-37.8	-13.2	-29.3	Inferior Temporal Gyrus	Temporal	0.15	hippocampus, medial temporal, hippocampal
232	-35.7	-24.8	-14.9	Hippocampus	Limbic	0.15	anterior temporal, temporal, medial temporal
135	-18.2	19	-21	Orbitofrontal	Prefrontal	0.14	paralimbic, orbitofrontal, cortex amygdala
136	-5.8	18.2	-21.6	Orbitofrontal	Prefrontal	0.14	subgenual, major depression, depression
120	21.2	-36.4	22.6	NA	Subcortical	0.13	N/A

Chapter 3: Extensions and application of the robust shared response model to electroencephalography data for enhancing brain-computer interface systems

Full author list: Andrew J. Graves, Cory Clayton, Joon Yuhl Soh, Gabe Yohe, Per B. Sederberg

Published in IEEE Systems and Information Engineering Design Symposium (SIEDS).

**Because this paper was written in LaTeX and involves a substantial number of mathematical equations, the final published .pdf was incorporated into this dissertation rather than converting to the same Word format applied to Chapters 1 and 2.*

Extensions and Application of the Robust Shared Response Model to Electroencephalography Data for Enhancing Brain-Computer Interface Systems

Andrew J. Graves
School of Data Science
University of Virginia
Charlottesville, VA
ajg3eh@virginia.edu

Cory Clayton
School of Data Science
University of Virginia
Charlottesville, VA
acc2ds@virginia.edu

Joon Yuhl Soh
School of Data Science
University of Virginia
Charlottesville, VA
js8hh@virginia.edu

Gabe Yohe
School of Data Science
University of Virginia
Charlottesville, VA
gjy7kb@virginia.edu

Per B. Sederberg
Department of Psychology
University of Virginia
Charlottesville, VA
pbs5u@virginia.edu

***Abstract*—Brain Computer Interfaces (BCI) decode electroencephalography (EEG) data collected from the human brain to predict subsequent behavior. While this technology has promising applications, successfully implementing a model is challenging. The typical BCI control application requires many hours of training data from each individual to make predictions of intended activity specific to that individual. Moreover, there are individual differences in the organization of brain activity and low signal-to-noise ratios in noninvasive measurement techniques such as EEG. There is a fundamental bias-variance trade-off between developing a single model for all human brains vs. an individual model for each specific human brain. The Robust Shared Response Model (RSRM) attempts to resolve this trade-off by leveraging both the homogeneity and heterogeneity of brain signals across people. RSRM extracts components that are common and shared across individual brains, while simultaneously learning unique representations between individual brains. By learning a latent shared space in conjunction with subject-specific representations, RSRM tends to result in better predictive performance on functional magnetic resonance imaging (fMRI) data relative to other common dimension reduction techniques. To our knowledge, we are the first research team attempting to expand the domain of RSRM by applying this technique to controlled experimental EEG data in a BCI setting. Using the openly available Motor Movement/ Imagery dataset, the decoding accuracy of RSRM exceeded models whose input was reduced by Principal Component Analysis (PCA), Independent Component Analysis (ICA), and subject-specific PCA. The results of our experiments suggest that RSRM can recover distributed latent brain signals and improve decoding accuracy of BCI tasks when dimension reduction is implemented as a feature engineering step. Future directions of this work include augmenting state-of-the art BCI with efficient reduced representations extracted by RSRM. This could enhance the utility of BCI technology in the real world. Furthermore, RSRM could have wide-ranging applications across other machine-learning applications that require classification of naturalistic data using reduced representations.**

***Index Terms*—Brain-computer interface, Electroencephalography, Machine learning**

I. Introduction

Brain Computer Interfaces (BCI) have garnered a lot of attention in the worlds of technology, data science, medicine, and neuroscience [14, 15]. Many recent strides in BCI technology have led to astonishing new possibilities in brain research and development [10]. A critical function of any BCI system is the ability to decode data collected from the human brain to predict subsequent behavior, which can be used for prosthetics and epilepsy research [5, 1]. Successfully deploying a model that predicts human behavior from data generated by the brain is difficult to do well, given it requires both computational speed and high accuracy. The typical BCI application requires many hours of training data from each individual to make accurate predictions specific to that individual. Moreover, there are individual differences in the organization of brain activity and low signal-to-noise ratios in noninvasive measurement techniques such as EEG.

Even though individuals have different spatial topographies with respect to brain activation, a common analytical assumption in neuroscience research is that all spatial features are anatomically aligned. This assumption imposes a structure such that all brain activation across individuals operates in a similar location in space [4]. This assumption extends beyond anatomical alignment into temporal dynamics and synthetically engineered features. However, averaging topographies across subjects has not shown much promise in accuracy for training individual models [13]. To account for this limitation, a different approach is to align features based on "function" rather than space [8]. We would like to have a method that can map different functional topographies from individuals into a common shared latent space. The shared response modeling framework was designed to accomplish this task of achieving proper functional alignment across individuals [3].

A. Prior work on shared response modeling

The Robust Shared Response Model (RSRM) is a latent variable model that projects a collection of time series into a compressed feature space [13]. In order to learn representations common between brains under a specific task protocol, RSRM extracts components that are shared across individuals. RSRM and its close variants [Shared Response Model (SRM)] were initially developed for applications with functional magnetic resonance imaging (fMRI) data under tasks that involve temporally synchronized naturalistic stimuli [3, 11]. SRM

demonstrated superior performance on applications to fMRI data over other common dimension-reduction methods such as Principal Component Analysis (PCA) and Independent Component Analysis (ICA). RSRM was able to successfully extract both common features between subjects and unique features within subjects despite different functional topographies in the raw data space [13]. The key difference between RSRM and SRM is that SRM only maps to a shared feature space, and does not directly model individual differences. Experimental results for RSRM in comparison to the SRM showed that the RSRM performed slightly better than the SRM as well as trained faster in time segment matching and classification [13].

Notably, there does not seem to be any prior work applying the shared response modeling framework to domains outside of fMRI. This paper presents new experiments that suggest RSRM is a useful dimension reduction technique in the context of decoding brain signals using EEG. We have reason to hypothesize that directly modeling individual differences using RSRM instead of SRM could lead to better performance in EEG environments. The aim of this paper is to investigate the utility of RSRM for EEG interfaced movement control applications. We will begin with a brief mathematical description of RSRM. Then we will describe simulations to demonstrate recovery of latent time-series signals using RSRM. Finally, we will discuss our empirical application of RSRM to model EEG data.

II. Methods

A. RSRM notation and formulation

Let N be the number of subjects, v the number of features, k the number of latent components, and t the number of events. The following expression is the primary equation for the RSRM [13] (see Figure 1 for the model design as applied to EEG).

$$\mathbf{X}^{(i)} = \mathbf{W}^{(i)}\mathbf{R} + \mathbf{S}^{(i)} + \mathbf{E}^{(i)},\ i = 1 \dots N \tag{1}$$

where (i) is the indexer for each individual subject and

- $\mathbf{X}^{(i)} \in \mathbb{R}^{v_i \times t}$ is the data matrix.
- $\mathbf{W}^{(i)} \in \mathbb{R}^{v_i \times k}$ is the matrix mapping from the observed subject space to the shared latent space.
- $\mathbf{R} \in \mathbb{R}^{k \times t}$ is the shared-response matrix.
- $\mathbf{S}^{(i)} \in \mathbb{R}^{v_i \times t}$ is the non-shared matrix unique to each individual subject.
- $\mathbf{E}^{(i)} \in \mathbb{R}^{v_i \times t}$ is an additive noise matrix specific for each subject.

Equation (1) is then estimated by solving the following optimization problem:

$$\min_{\mathbf{S}^{(i)}, \mathbf{W}^{(i)}, \mathbf{R}} \sum_{i=1}^{N} \frac{1}{2} ||\mathbf{X}^{(i)} - \mathbf{W}^{(i)}\mathbf{R} - \mathbf{S}^{(i)}||_F^2 + \lambda_i ||\mathbf{S}^{(i)}||_1 \tag{2}$$

s.t.

$$\mathbf{W}^{(i)^T}\mathbf{W}^{(i)} = \mathbf{I},\ \forall\ i = 1 \dots N.$$

Equation (2) is a non-convex optimization problem, but we can estimate subsets of the model using convex optimization techniques and then combine the results at the end. Using Block Coordinate Descent, we can partition the variables into blocks and optimize each block while fixing the other blocks constant. In RSRM, each individual mapping from the latent space $\mathbf{W}^{(i)}$, each individual non-shared/unique matrix $\mathbf{S}^{(i)}$, and the shared response model $\mathbf{R}$ is a block. Because optimizing each of these blocks while keeping the other blocks constant is a convex problem, we can approximate the global optimum with a greedy solution. This is an iterative optimization procedure by which we apply the three following routines defining the block coordinate descent.

First, we solve for $\mathbf{W}^{(i)}$ by using the Procrustes method [6]

$$\mathbf{W}^{(i)} = \mathbf{U}^{(i)}\mathbf{V}^{(i)^T} \tag{3}$$

where $\mathbf{U}^{(i)}\mathbf{V}^{(i)^T}$ is achieved through singular value decomposition (SVD)

$$\mathbf{U}^{(i)}\mathbf{\Sigma}^{(i)}\mathbf{V}^{(i)} = (\mathbf{X}^{(i)} - \mathbf{S}^{(i)})\mathbf{R}^T. \tag{4}$$

Second, we solve for $\mathbf{S}^{(i)}$ using a soft shrinkage penalty

$$\mathbf{S}^{(i)} = \text{Shrink}(\mathbf{X}^{(i)} - \mathbf{W}^{(i)}\mathbf{R}, \lambda) \tag{5}$$

where the amount of shrinkage is determined by λ. More specifically, soft shrinkage is applied to $\mathbf{D}^{(i)} \in \mathbb{R}^{v_i \times t}$

$$s = S_{\lambda_i}(d) = \begin{cases} (|d| - \lambda_i)\text{sign}(d), & \text{if } |d| > \lambda_i \\ 0 & \text{otherwise,} \end{cases} \tag{6}$$

where the individual residual $\mathbf{D}^{(i)}$ is

$$\mathbf{D}^{(i)} = \mathbf{X}^{(i)} - \mathbf{W}^{(i)}\mathbf{R}. \tag{7}$$

In other words, soft shrinkage of $\mathbf{D}^{(i)}$ is equal to $\mathbf{S}^{(i)}$. Last, we solve for $\mathbf{R}$ with

$$\mathbf{R} = \frac{1}{N}\sum_{i=1}^{N} \mathbf{W}^{(i)^T}(\mathbf{X}^{(i)} - \mathbf{S}^{(i)}). \tag{8}$$

We can specify the shrinkage parameter λ to balance how much is shared ($\mathbf{R}$) by all subjects and how much is unique to each subject ($\mathbf{S}^{(i)}$). As $\lambda \to \infty$, the model is equivalent to the deterministic solution where $\mathbf{S}^{(i)} \to 0$. As $\lambda \to 0$, there will

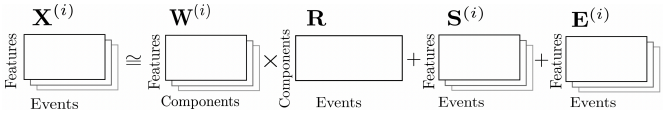

Fig. 1. Visual depiction of the matrices that represent the RSRM. For this EEG application, features are an array of time-frequency values over each channel. Components (k) are the latent vectors extracted by RSRM. The translation of this model from fMRI to EEG data was not trivial, given their respective temporal and spatial resolution limitations. Note that dropping the additive noise matrix $\mathbf{E}^{(i)}$ makes this an approximate solution.

be no shared response between individuals and all portions are unique to each individual ($\mathbf{S}^{(i)} \rightarrow \mathbf{X}^{(i)}$). Additionally, we can specify the number of components we want our model to compute. This is analogous to selecting the number of components in PCA.

B. Experiment 1: Simulation methods

In order to get an intuitive sense that RSRM works for EEG-like time series, we simulated data with known parameters and attempted to recover them through visualization of the latent shared space. For this simulation, we translated the extant Python RSRM code [9] into the R programming language, both for other R programmers to use and to check the robustness of implementations using different numerical libraries. Sine-waves with specific frequencies f are a simple surrogate for simulating EEG time-series signals. Given RSRM is greedy and there are no guarantees that it will return the globally optimal solution, we predicted output that visually matches our prior expectation, rather than searching for a specific point estimate for f. This is because multiple signals will likely be embedded into the same latent space and will not be perfectly separated. Alternatively, one could compute a Fast Fourier transformation of the latent vector to estimate its power at specific frequencies.

The simulation incorporated signals from 32 electrodes and 100 different individuals. We randomly sampled two different deterministic sine-wave signals [10 Hz, 25 Hz] across electrodes. Different individuals had randomly sampled locations of the signals across the scalp to test if RSRM could effectively recover signals that were not spatially aligned. We perturbed these sine-wave signals by adding Gaussian noise generated by $N \sim (\mu = 0, \sigma = 4)$. Let A be amplitude, θ phase angle offset, and $\mathbf{t} \in \mathbb{R}^N$ represent time. Sine-waves were generated with the following expression

$$A \sin(2\pi f \mathbf{t} + \theta) \tag{9}$$

fixing $A = 1$, $\theta = 0$, and $N = 1000$. We attempted to recover all instances of f in the latent shared response space. We fit exactly two components to test if the two recovered latent vectors resembled the two true signal distributions. We experimentally manipulated λ values [0, 100000] to test its role in modeling shared latent spaces.

C. Experiment 2: Empirical application methods

1) Dataset description: In order to test the application of RSRM on our EEG data, we used the openly available EEG Motor Movement/Imagery Dataset [12]. We chose this dataset as a benchmark because it includes data from a large number of individuals (relative to other openly available EEG datasets), and the specific tasks are directly related to solving motor movement problems using BCI. This dataset contains 12 two-minute task-related runs (i.e., recordings) for each individual. Each person performed four different tasks under three separate runs. The four tasks are:

1) Open and close left vs. right fist
2) Imagine opening and closing left vs. right fist
3) Open and close both fists vs. both feet
4) Imagine opening and closing both fists vs. both feet

Each task includes two motor movements of interest with at least 21 trials for each motor movement (see Figure 2). Thus, each task allows us to make 42 predictions for each individual subject, which results in 4410 classification labels for each task.

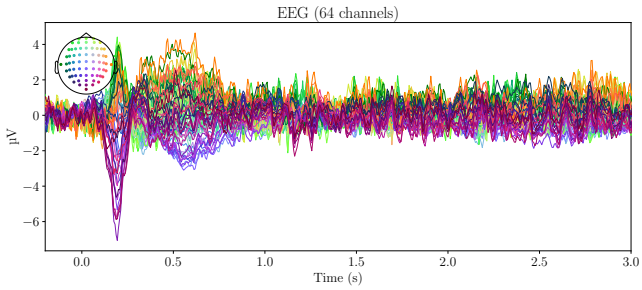

Fig. 2. Example evoked difference waveform of one of the motor movement tasks: imagining closing fists vs. imagining closing feet. The majority of the visually distinguishable signals in the time domain occur in the 200-1000 ms range and are spatially distributed across the brain.

2) EEG Pre-processing Workflow: The Raw EEG Motor Movement/Imagery Dataset was pre-processed using the MNE and pyprep Python software libraries [7, 2]. First, we loaded the data and added channel location coordinates. Next, we applied a band-pass filter [infinite impulse response (IIR) Butterworth model; high-pass cutoff: 1 Hz, low-pass cutoff: 50 Hz] to smooth the brain signals. Bad channels were automatically identified by low signal-to-noise ratios, near zero-variance recordings, and large deviations from nearby spatial regions. Then an average reference was applied to the data, which subtracts the average signal across the brain to improve signal-to-noise ratios across electrodes. Then we spatially interpolated all identified bad channels to preserve the dimensionality of the dataset across individuals. We segmented the data into 3 second trials with a 200 ms baseline relative to stimulus onset, which cued the individual to perform the task of interest. We then realigned the task events such that each individual had the same sequence of trial type for each task. This was necessary because fitting RSRM requires a temporal synchronization with respect to classification labels, while EEG experiments typically randomize the onset of specific events. For the final feature engineering step, we decomposed the signals into a time-frequency representation using Morlet wavelets. From this decomposition, we generated 12 families of frequencies logarithmically spaced between 3 Hz and 45 Hz. We averaged these time-frequency representations across 400 ms time-windows strictly to keep the data input at a manageable size for our unsupervised learning experiments. We reshaped the data such that the time-frequency representations for each channel were encoded as rows of the data matrix, and the specific events were encoded as the columns of the matrix.

3) Experimental Design: In order to test the capacity of RSRM to effectively represent relevant brain signals in a reduced space, we systematically varied the dimensionality of the reduced space and compared decoding performance with other traditional dimension-reduction techniques. We used the BrainIAK software library in Python for fitting RSRM [9]. The unsupervised learning techniques employed were RSRM, PCA, ICA, and within-subject PCA. For RSRM, each individual had its own matrix $\mathbf{X}^{(i)} \in \mathbb{R}^{6144\times 42}$, later transposed and concatenated after applying RSRM fit and transformation methods. For within-subject PCA, each individual matrix was the transpose of the initial RSRM matrices and were trained independently for each subject. For PCA and ICA, each of these individual matrices were concatenated into one single matrix $\mathbf{X} \in \mathbb{R}^{4410\times 6144}$. For each model, we reduced the original feature representation into a specified number of components k. Then we trained a support vector machine classifier with a radial basis function kernel to decode one class from the other for each task. We chose not to tune the hyper-parameters C and γ because our primary research question concerned the relative accuracy of each dimension-reduction technique, rather than optimizing performance for each model configuration. We estimated model performance by using leave-one-run-out cross-validation. For each task, there were three runs which resulted in three folds. Thus, we trained each model on 28 events from each subject and then tested them on the remaining 14 subject events until we had predictions for all 42 events for each subject. Because of this validation scheme, we were constrained by RSRM to fit at most 28 latent components ($k << v$ given that $v = 6144$). For RSRM, λ was held constant at 2.5 and the model was run with 2 iterations. We chose a low number of iterations such that the model training time would be as short as possible.

III. Results

A. Experiment 1: Simulation results

Using 10 Hz and 25 Hz sine-wave signals perturbed by a stochastic distribution $N \sim (\mu = 0, \sigma = 4)$, we generated a raw collection of time-series signals. We fit RSRM to these raw signals to test its ability to recover the deterministic signals. We were able to capture the majority of the deterministic sine-wave distribution, which represents the true signal without noise, within two components of the RSRM given a high value of λ (Figure 3). This gives us confidence that this modeling procedure may prove to be useful for application in EEG.

B. Experiment 2: Empirical application results

After validating the potential utility of RSRM for EEG-like data structures, we compared the performance of RSRM to PCA, ICA, and within-subject PCA for classification tasks within the Motor Movement/ Imagery Dataset. We observed that RSRM demonstrated superior performance for all 4 tasks, yielding significantly higher decoding accuracy (see Figure 4 and Table I). Statistical comparisons only include RSRM in relation to within-subject PCA, because PCA and ICA performed much worse than RSRM given most values of k. This pattern of results is consistent with the previous literature in fMRI [3]. This suggests that RSRM is a useful feature engineering step for EEG processing pipelines, when the dimensionality of the input space needs to be reduced.

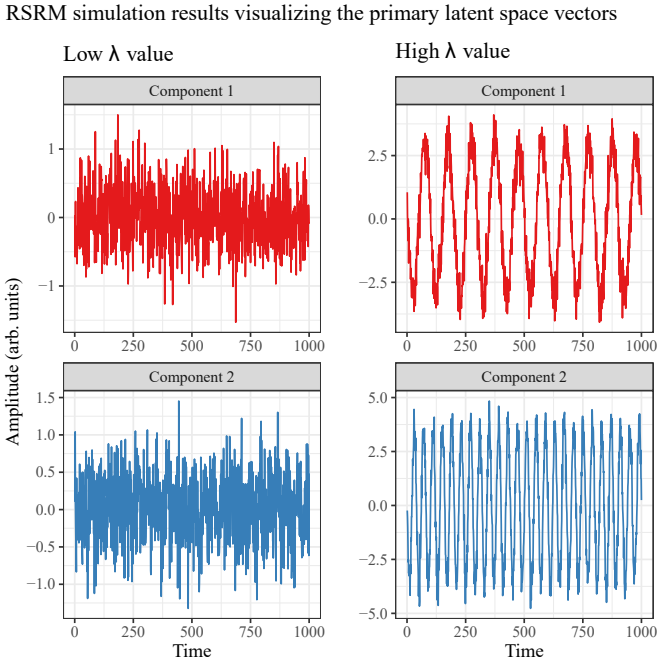

Fig. 3. First two RSRM components captured from noisy sine-wave signals. As predicted, When λ was very low, the model learned almost no shared information across individuals. Thus, the left side of the figure is only capturing an idiosyncratic and stochastic distribution across subjects. When λ is very high, the model prioritizes shared information across individuals over unique information. This is why the first two components are primarily capturing the deterministic signal in the distribution, namely 10 Hz (top-right) and 25 Hz (bottom-right). For non-simulated applications, λ is a hyperparameter that can be tuned to balance this trade-off.

IV. Discussion

A. Summary

The primary purpose of this research was to investigate whether a robust shared response model can effectively factor common and unique EEG signals between the brains of different individuals into a reduced feature space. When applied to a relatively simple machine learning classification model, the data pre-processed by RSRM was able to predict significantly above chance and was able to outperform all other dimension reduction techniques that we tested. The results suggest that RSRM captured aspects of the shared feature space above and beyond standard dimension reduction techniques typically used in neuroscience.

B. Limitations and Future Directions

The primary limitation of this experiment was the relatively low values of accuracy on each of the four tasks. We believe this is due to our leave-one-run-out cross-validation scheme, which constrained us to training the RSRM on only 28 events for each subject. Based on the patterns in Figure 4,

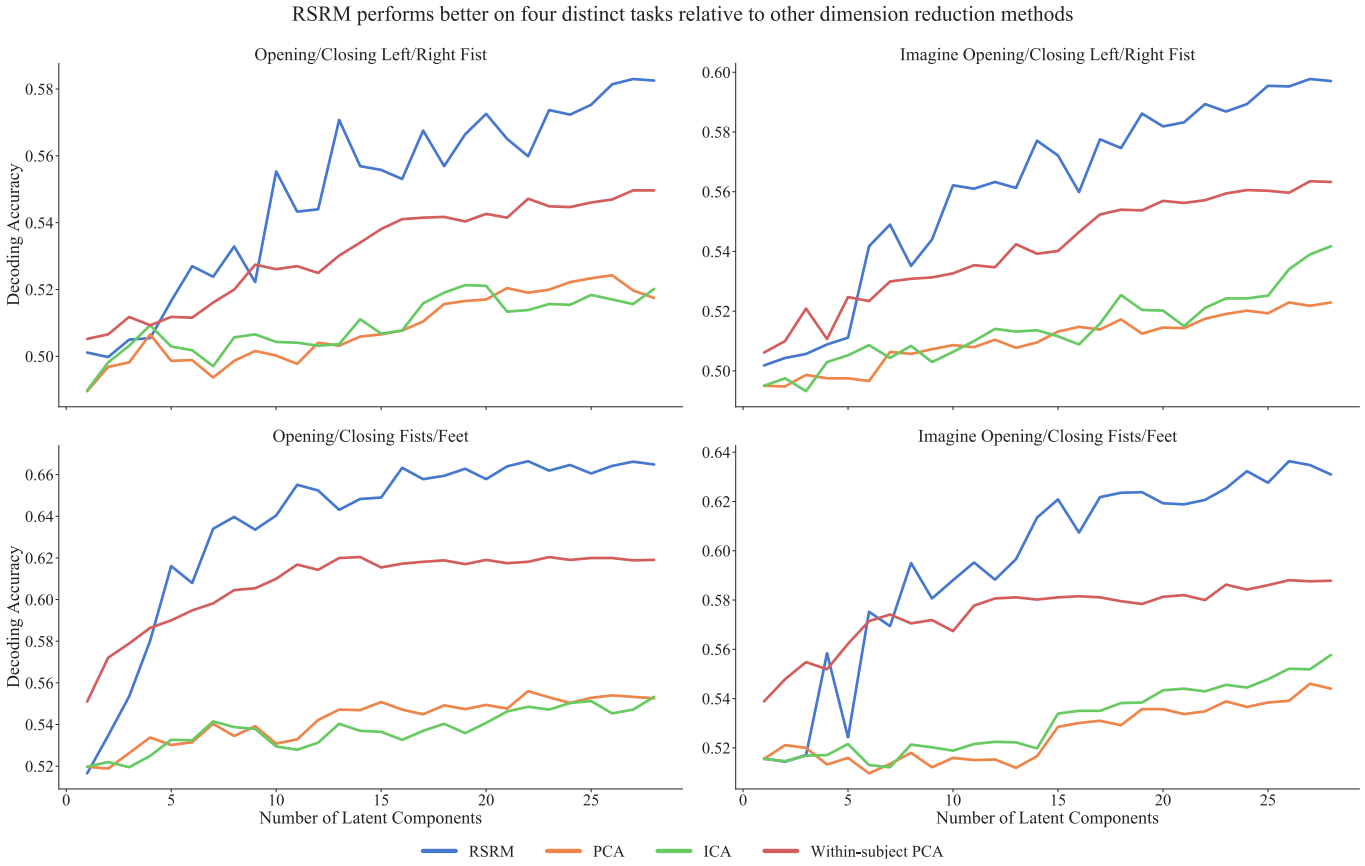

Fig. 4. Primary results from Experiment 2. RSRM outperforms on all four tasks relative to other standard dimension reduction techniques that were tested (chance decoding performance $= 0.50$). Here, we are analyzing relative accuracy between these methods, rather than trying to maximize accuracy with one single model configuration. The crucial accuracy difference is when the number of components is 28. Additionally, the RSRM latent representation improves performance at lower values of k. Importantly, it appears that increasing k would likely increase the differences in performance between RSRM and the other three techniques. Note that PCA and ICA require $k >> 28$ to reach the current performance level of RSRM from this experiment (fixing $k = 28$ for RSRM).

TABLE I
PAIRED t-TESTS COMPARING RSRM TO WITHIN-SUBJECT PCA ACROSS ALL NUMBER OF COMPONENTS

Task	t	df	p
Open and close left vs. right fist	6.73	27	$< .001$
Imagine opening and closing left vs. right fist	6.78	27	$< .001$
Open and close both fists vs. both feet	6.15	27	$< .001$
Imagine opening and closing both fists vs. both feet	4.05	27	$< .001$

the accuracy looks as though it would likely increase as additional components computed by RSRM are added. We also did not fine-tune any specific classifier for any given model configuration, as we wanted to be able to make direct comparisons across each model instance. Finally, there are likely more principled ways to feature engineer the data before fitting RSRM to EEG. For example, we averaged the Morlet wavelet decomposition time-frequency representations over 400 ms time-windows, which only provides a crude estimate and may in fact conflate multiple independent processes into one single vector.

We plan on running future experiments on different datasets with enough components for the accuracy to stabilize, in conjunction with more sophisticated feature engineering and supervised learning. In fact, RSRM could be particularly beneficial to deep learning frameworks whose training requires large amounts of data. Applying RSRM to artificial neural networks would allow combining datasets across individuals for training. Future work will expand these experiments to predicting more than two classes, as well as attempting to decode brain signals in a streaming real-time application. Despite these stated limitations, we argue that this work contributes toward the cumulative science of designing better BCI systems.

C. Conclusions

Training BCIs on EEG data is challenging due its relatively low signal-to-noise ratio. The typical BCI application requires building a new decoding model for each patient

due to the unique anatomical and functional topographies between patients' EEG signals. This research attempted to tackle these problems by applying RSRM, which is known to work well with fMRI data, and adapt it to function with scalp EEG data. We found that RSRM as a feature engineering step outperformed PCA, ICA, and within-subject PCA across four different motor movement tasks. A key attribute of RSRM is its ability to reduce dimensionality in the data, which leads to a significant reduction in model training time as well as a reduction in training data needed to build a sufficient model. This has the ability to have a meaningful impact on patients' lives who require a BCI for performing specific tasks. Furthermore, RSRM could have wide-ranging applications across other machine-learning applications that require decoding/classification of naturalistic data using reduced representations.

Acknowledgment

We would like to thank our project mentors Dr. Timothy W. Clark, Dr. Mohammad Sadnan Al Manir, and the UVA School of Data Science for their training, and feedback throughout this research project's development. We also would like to thank the UVA Department of Psychology for their intellectual support that made this research possible.

References

[1] Rafeed Alkawadri. "Brain–Computer Interface (BCI) Applications in Mapping of Epileptic Brain Networks Based on Intracranial-EEG: An Update". In: *Frontiers in Neuroscience* 13 (2019). Publisher: Frontiers. ISSN: 1662-453X. DOI: 10.3389/fnins.2019.00191. URL: https://www.frontiersin.org/articles/10.3389/fnins.2019.00191/full.

[2] Nima Bigdely-Shamlo et al. "The PREP pipeline: standardized preprocessing for large-scale EEG analysis". In: *Frontiers in Neuroinformatics* 9 (2015). Publisher: Frontiers. ISSN: 1662-5196. DOI: 10.3389/fninf.2015.00016. URL: https://www.frontiersin.org/articles/10.3389/fninf.2015.00016/full.

[3] Po-Hsuan (Cameron) Chen et al. "A Reduced-Dimension fMRI Shared Response Model". In: *Advances in Neural Information Processing Systems 28*. Ed. by C. Cortes et al. Curran Associates, Inc., 2015, pp. 460–468. URL: http://papers.nips.cc/paper/5855-a-reduced-dimension-fmri-shared-response-model.pdf.

[4] Jonathan D. Cohen et al. "Computational approaches to fMRI analysis". In: *Nature Neuroscience* 20.3 (Mar. 2017). Number: 3 Publisher: Nature Publishing Group, pp. 304–313. ISSN: 1546-1726. DOI: 10.1038/nn.4499. URL: https://www.nature.com/articles/nn.4499.

[5] Daniel Elstob and Emanuele Lindo Secco. "A Low Cost Eeg Based Bci Prosthetic Using Motor Imagery". In: *arXiv:1603.02869 [cs]* (Mar. 9, 2016). arXiv: 1603.02869. URL: http://arxiv.org/abs/1603.02869.

[6] John C. Gower and Garmt B. Dijksterhuis. *Procrustes problems*. Vol. 30. Oxford, UK: Oxford University Press, Jan. 22, 2004. 248 pp. ISBN: 978-0-19-851058-1. URL: http://www.oup.com/uk/catalogue/?ci=9780198510581.

[7] Alexandre Gramfort et al. "MEG and EEG data analysis with MNE-Python". In: *Frontiers in Neuroscience* 7 (2013). Publisher: Frontiers. ISSN: 1662-453X. DOI: 10.3389/fnins.2013.00267. URL: https://www.frontiersin.org/articles/10.3389/fnins.2013.00267/full.

[8] James V Haxby et al. "Hyperalignment: Modeling shared information encoded in idiosyncratic cortical topographies". In: *eLife* 9 (June 2, 2020). Ed. by Chris I Baker and Floris P de Lange. Publisher: eLife Sciences Publications, Ltd, e56601. ISSN: 2050-084X. DOI: 10.7554/eLife.56601. URL: https://doi.org/10.7554/eLife.56601.

[9] Manoj Kumar et al. "BrainIAK tutorials: User-friendly learning materials for advanced fMRI analysis". In: *PLOS Computational Biology* 16.1 (Jan. 15, 2020). Publisher: Public Library of Science, e1007549. ISSN: 1553-7358. DOI: 10.1371/journal.pcbi.1007549. URL: https://journals.plos.org/ploscompbiol/article?id=10.1371/journal.pcbi.1007549.

[10] Elon Musk and Neurolink. "An integrated brain-machine interface platform with thousands of channels". In: *J Med Internet Res* 21.10 (2019), p. 12. DOI: 10.2196/16194. URL: http://www.jmir.org/2019/10/e16194/.

[11] Hugo Richard et al. "Fast shared response model for fMRI data". In: (Sept. 27, 2019). arXiv: 1909.12537 [cs.CV]. URL: https://arxiv.org/abs/1909.12537.

[12] Gerwin Schalk et al. "BCI2000: a general-purpose brain-computer interface (BCI) system". In: *IEEE transactions on bio-medical engineering* 51.6 (June 2004), pp. 1034–1043. ISSN: 0018-9294. DOI: 10.1109/TBME.2004.827072.

[13] Javier S. Turek et al. "Capturing Shared and Individual Information in fMRI Data". In: *2018 IEEE International Conference on Acoustics, Speech and Signal Processing (ICASSP)*. ICASSP 2018 - 2018 IEEE International Conference on Acoustics, Speech and Signal Processing (ICASSP). Calgary, AB: IEEE, Apr. 2018, pp. 826–830. ISBN: 978-1-5386-4658-8. DOI: 10.1109/ICASSP.2018.8462175. URL: https://ieeexplore.ieee.org/document/8462175/.

[14] J. J. Vidal. "Real-time detection of brain events in EEG". In: *Proceedings of the IEEE* 65.5 (May 1977). Conference Name: Proceedings of the IEEE, pp. 633–641. ISSN: 1558-2256. DOI: 10.1109/PROC.1977.10542.

[15] J. J. Vidal. "Toward Direct Brain-Computer Communication". In: *Annual Review of Biophysics and Bioengineering* 2.1 (1973), pp. 157–180. DOI: 10.1146/annurev.bb.02.060173.001105. URL: https://doi.org/10.1146/annurev.bb.02.060173.001105.

Conclusions

All three chapters within this dissertation contain novel contributions to the literature and span a wide variety of important contemporary problems in psychology and neuroscience. The common thread linking these interdisciplinary efforts is 1) the committed focus to understanding why people's minds and brains operate differently from one another, and 2) the successful application of modern machine learning tools to function as a mechanism for uncovering new insights about the brain and behavior. More broadly, all three chapters have potential to contribute to applications in order to better understand brain mechanisms underlying specific neuropsychological conditions (Chapter 1: Prosopagnosia, Chapter 2: Alzheimer's disease related dementias., Chapter 3: Parkinson's). The remaining paragraphs recapitulate the main findings from each chapter, highlighting the significance and novelty within each respective domain of study.

In Chapter 1, we were the first to demonstrate using fMRI that decoding rates of stimulus states for faces is significantly related to face recognition ability in neurotypicals, suggesting that the spatial patterns underlying stimulus encoding and processing are more discriminative as face recognition ability increases. While this relationship is not strictly due to regions within the *core* face network, we do find that the right p STS and FFA are important mechanisms for supporting successful face recognition. Additionally, for the first time, we find that state-of-the-art CPM-based techniques fail to capture these individual differences in face recognition ability. These patterns of results point toward face recognition ability being a unique cognitive process that may be less globally distributed with respect to neural mechanisms in contrast to other complex cognitive processes such as attention or decision-making. This chapter's results suggest that individual differences in face recognition ability may be largely constrained to canonical cortical regions sensitive to faces, in line with a local rather than distributed account. This work contributes to a better understanding of how domain-specific neural systems support behavioral heterogeneity in face recognition, and suggests that specialized preferential higher-order visual cortices may be more important than whole-brain connectivity for understanding this specific behavior.

In Chapter 2, we provide confirmatory evidence that epigenetic age acceleration relates to between-person differences in cognitive abilities of both fluid and crystallized intelligence, and we were the first to demonstrate that functional connectivity profiles that predict AgeAccelGrim are similar to functional connectivity profiles that predict memory abilities. Specifically, individuals with more epigenetic age acceleration tended to perform worse on tasks that spanned a wide variety of cognitive faculties, and brain regions crucial for successful memory formation were most important for predicting AgeAccelGrim in the aging brain. These differences cannot be explained by chronological age alone, in that AgeAccelGrim and chronological age are orthogonal variables, and both were included/ controlled for in each statistical model. This suggests that epigenetic age explains a unique portion of variance of cognitive ability that chronological age does not capture, and this relationship may be explained by connectivity of memory brain structures primarily within the limbic system. These brain structures are known to be important for aging and cognitive change, and here we

demonstrate that epigenetic age acceleration captures a unique portion of this functional brain organization as it pertains to these differences.

In Chapter 3, we were the first to demonstrate that RSRM can effectively factor common and unique EEG signals between the brains of different individuals into a reduced feature space to improve the quality of brain-computer interfaces. The results suggest that RSRM captured aspects of the shared feature space above and beyond standard dimension reduction techniques typically used in neuroscience, pointing to a benefit of mathematical considerations with respect to individual differences in the topography of brain signals. We found that RSRM as a feature engineering step outperformed PCA, ICA, and within-subject PCA across four different motor movement tasks. This has the ability to have a meaningful impact on patients' lives who require a BCI for performing specific tasks. Furthermore, RSRM could have wide-ranging applications across other machine-learning applications that require decoding/classification of naturalistic data using reduced representations.